

ACOUSTIC STREAMING IN COMPRESSIBLE TURBULENT
BOUNDARY LAYERS

A Dissertation
Submitted to the Faculty
of
Purdue University
by
Iman Rahbari

In Partial Fulfillment of the
Requirements for the Degree
of
Doctor of Philosophy

December 2019
Purdue University
West Lafayette, Indiana

**THE PURDUE UNIVERSITY GRADUATE SCHOOL
STATEMENT OF DISSERTATION APPROVAL**

Dr. Guillermo Paniagua, Chair

School of Mechanical Engineering

Dr. J. Stuart Bolton

School of Mechanical Engineering

Dr. Gregory A. Blaisdell

School of Aeronautics and Astronautics

Dr. Eusebio Valero

School of Aeronautical and Space Engineering (Universidad Politécnica
de Madrid)

Dr. Beni Cukurel

Faculty of Aerospace Engineering (IIT-Technion)

Approved by:

Dr. Nicole Key

Associate Head for Graduate Studies

To my Baba and Maman

ACKNOWLEDGMENTS

First and foremost, I would like to thank Professor Guillermo Paniagua for giving me the opportunity to continue my studies at Purdue University. Professor Paniagua has always been a great support in every possible instance, and I will always remain indebted to him for all his ideas, guidance, and encouragement throughout my Ph.D.

I extend my gratitude to my Ph.D. committee members from Purdue University; Professor J. Stuart Bolton, for teaching me all I know about the acoustics, and Professor Gregory Blaisdell, for his excellent course on the turbulence modeling. I cannot express how grateful I am towards Professor Blaisdell for his support and guidance over the course of my research, from giving access to the *Rice* cluster during the most crucial period of my Ph.D. to many fruitful discussions. I appreciate the invaluable comments of Professor Eusebio Valero from UPM Madrid on the Linear Stability Analysis and flow control, and Professor Beni Cukurel from IIT-Technion for great discussions and comments during the BSF meetings.

This research has been supported in part by Grant No 2016358 from the Binational Science Foundation and Summer Research Fellowship from the School of Mechanical Engineering at Purdue University. Numerical simulations have been performed partially using the Extreme Science and Engineering Discovery Environment (XSEDE) Comet at SDSC and Bridges at PSC through allocation TG-CTS170041 and, partially on the Amazon Web Service provided through the AWS Cloud Credits for Research program. Purdue University's *Rice* cluster have been used for data management and post-processing purposes. I would like to gratefully acknowledge Professor Sanjiva Lele for granting access to an early version of the code CFDSU developed for high-fidelity numerical simulations.

I also thank Professor Carlo Scalo for his support during the early stage of my Ph.D. research and his help during the development of the Linear Stability tools. I

learned invaluable skills from Professor Scalo, for which I am truly grateful. Moreover, I would like to thank Professor Vahid Esfahanian, from the University of Tehran, for teaching me the fundamentals of the Computational Fluid Dynamics. I also appreciate the continued support from Prof. Mohammad Hassan Rahimian and Professor Mojtaba Tahani in the past several years.

Life at Purdue has been a fantastic adventure, thanks to my incredible friends; Mario and James (both take the first spot, jointly), Maggie Jo (should also be the first, too), Valeria, David, Jorge, Francisco, and the entire PETAL team with whom I have had the chance to discuss, collaborate and share. I also wish to thank Soroush and Amir Hossein for the countless hours of fantastic conversations and ALL my awesome friends in West Lafayette that have made my Ph.D. life a terrific one.

Lastly, I would like to whole-heartedly appreciate the support of my family; Baba and Maman for all their unimaginable sacrifices, and Amir, Shahla, and Shahram for their support and encouragement throughout this journey.

TABLE OF CONTENTS

	Page
LIST OF TABLES	viii
LIST OF FIGURES	ix
ABSTRACT	xvii
1. INTRODUCTION	1
1.1 Literature Review	1
1.2 Research Objectives	4
1.3 Research Methodology	4
1.4 Research Guideline	5
2. NUMERICAL METHODS	7
2.1 Fully-compressible Navier-Stokes Equations	7
2.2 Numerical Methods for Navier Stokes Simulations	8
2.2.1 Compact Finite Difference Method	9
2.2.2 Explicit Time Advancement	10
2.2.3 Implicit Time Advancement	10
2.2.4 Large Eddy Simulation Technique	11
2.3 Linearized Navier-Stokes Equations	12
2.4 Numerical Methods for Local Stability Analysis	14
2.4.1 Spectral Method	15
2.4.2 Validation of the Local Stability Solver	16
2.5 Numerical Methods for Global Stability Analysis	18
2.5.1 Spectral Methods for GSA	19
2.5.2 Compact Finite Difference for GSA	21
2.5.3 Sparse Implementation of Compact Finite Difference for GSA	22
2.5.4 Validation of the Global Stability Solver	27
2.6 Application of the Linear Stability Analysis in Turbulent Flow Simulations	30
3. ACOUSTIC EXCITATION FOR HEAT TRANSFER ENHANCEMENT IN HIGH-SPEED FLOWS	32
3.1 Problem Formulation	32
3.2 Results	34
3.2.1 Base Flow	34
3.2.2 Linearized Navier-Stokes Analysis	37
3.2.3 Fully Non-linear Navier-Stokes Simulations	40

	Page
3.2.4 On the Efficacy of the Linear Stability Analysis in Selecting the Optimal Modes	55
3.2.5 Parametric Analysis of Acoustic Excitation for Heat Transfer Enhancement	58
4. ACOUSTIC EXCITATION FOR HEAT TRANSFER REDUCTION IN HIGH-SPEED FLOWS	66
4.1 Problem Formulation	66
4.2 Results	68
4.2.1 Temporal Evolution of Perturbations	69
4.2.2 Near-wall Instantaneous Flow Fields	71
4.2.3 Time-averaged and Phase-Locked Averaged Statistics	73
4.2.4 Temporal Evolution of the Perturbations Resulted from Different Forcing Amplitudes $A_f \propto 1/\mathcal{T}$	77
4.2.5 Time-averaged and Phase-Locked Averaged Statistics at Different Forcing Amplitudes $A_f \propto 1/\mathcal{T}$	78
5. ACOUSTIC EXCITATION OF A SPATIALLY DEVELOPING BOUNDARY LAYER	85
5.1 Validation Study	86
5.2 Base Flow Calculation	89
5.3 Linear Stability Analysis	91
5.4 Fully Non-linear Calculations	93
6. CONCLUSIONS	100
REFERENCES	103
A. EQUATIONS FOR GLOBAL STABILITY ANALYSIS	108
VITA	114

LIST OF TABLES

Table	Page
2.1 Comparison of complex wave velocity, c , of the most unstable mode for compressible Couette flow with the reference values taken from Hu and Zhong [32] for several Re_∞ , M_∞ and k . Grid convergence study shown for $N=100$, $N=200$ and $N=300$, are respectively placed on the top, middle and bottom rows for each case.	18
2.2 Comparison of number of non-zero elements, nnz() , in matrices A and B (2.21), generated using implicit versus explicit compact scheme implementation for a model problem	25
2.3 Global stability analysis of leading edge boundary layer at $Re = 800$, $M = 0.02$ and $\beta = 0.255$ on a 48×48 grid where $c_i = \omega_i/\beta$ and $c_r = \omega_r/\beta$. Subscripts GH and A1 represent the Görtler-Hämmerlin and first anti-symmetric modes. Deviating digits are underlined.	29
3.1 Simulation parameters for the acoustically excited cases. Length of the forcing region in all cases is set to $L_f = 0.0745L_x$	41
4.1 Simulation parameters for the acoustic excitation normal to the flow in spanwise direction for a supersonic channel flow at $M_b = 1.5$	68

LIST OF FIGURES

Figure	Page
2.1 Comparison of complex wave velocity spectrum for compressible Couette flow at $\mu_\infty = 2$, $\text{Re}_\infty = 2 \times 10^5$, $k = 1$ using $N=100$ grid points (\circ) with results from Hu and Zhong [33] (\blacktriangledown). Real part (—) and imaginary part ($-\cdot-$) of velocity, \hat{u} , temperature, \hat{T} , and pressure, \hat{p} , eigenfunctions of the most unstable mode at $M_\infty = 5$, $\text{Re}_\infty = 5 \times 10^5$, $\alpha = 3$ with (a): $\Re\{\hat{T}\}$, (b): $\Re\{\hat{u}\}$, (c): $\Im\{\hat{T}\}$, (d): $\Im\{\hat{u}\}$, (aa): $\Re\{\hat{p}\}$, (bb): $\Im\{\hat{p}\}$	17
2.2 Comparison of complex phase velocity spectrum for laminar compressible Couette flow at $M_\infty = 5$, $\text{Re}_\infty = 1 \times 10^5$ and $k = 2.5$ using $N=100$ grid points (\blacktriangledown) against Hu and Zhong [32]. Real part (—) and imaginary part ($-\cdot-$) of velocity, \hat{u} , temperature, \hat{T} , and pressure, \hat{p} , eigenfunctions of the most unstable mode (indicated with downward arrow) with (a): $\Re\{\hat{T}\}$, (b): $\Re\{\hat{u}\}$, (c): $\Im\{\hat{T}\}$, (d): $\Im\{\hat{u}\}$, (aa): $\Re\{\hat{p}\}$, (bb): $\Im\{\hat{p}\}$	19
2.3 Spy plots of \mathbf{A} and \mathbf{B} matrices using dense implementation of compact scheme for a grid of 10×10	20
2.4 Spy plots of compact finite difference operators, L and R , and explicit derivative matrix, D . As it is shown, L and R operators are banded (tri- and penta-diagonal) matrices while the D matrix is dense.	22
2.5 Sample structure of A_u^X and A_v^X as part of the \mathbf{A} matrix (2.22). Blocks having non-zero entries are shaded while the ones with all zero elements are left white. The corresponding segments in the array $\hat{\mathbf{q}}$ are shown in the right. L_x and R_x are compact finite difference operators (2.34) in x -direction; similarly, L_y and R_y are these operators in y -direction. The rest correspond to different terms in the linearized Navier-Stokes equations.	24
2.6 Spy plots of \mathbf{A} and \mathbf{B} matrices using the implicit(sparse) implementation of compact scheme for a grid of 10×10	24
2.7 Total number of non-zero elements (left) and total highmark (right) for implicit and explicit implementations of compact scheme	30
3.1 Schematic view of the proposed setup. The computational domain is of size $(L_x, L_y, L_z) = (4\pi\delta, 2\delta, 1.5\pi\delta)$. The shaded area of width L_f in each unit indicates the region where the effect of acoustic drivers mounted on side-walls is modeled via forcing function of form (3.1)	33

Figure	Page
3.2 Mean streamwise velocity and temperature profiles as well as fluctuating velocity components at $Re_b = 3000$ and $M_b = 1.5$. Open circles (\circ) are taken from [23]	36
3.3 Time-averaged streamwise velocity, temperature and density at $Re_b = 3000$ and two different bulk Mach numbers, $M_b = 1.5$, and 0.75	36
3.4 Eigenvalue spectrum of compressible channel flow at $Re_b = 3000$ and $M_b = 1.5$ (left) and $M_b = 0.75$ (right). Streamwise wavenumber is $k = 0.5$ corresponding to the largest mode that fits inside a domain of size $L_x = 4\pi$. R_1 and all other modes located on the right side of the hook-shape modes are fast acoustic modes, L_1 and other modes appearing on its left side are slow acoustic modes and W_i ($i = 1$ on the left and $i = 2$ is on the right) are wall modes	38
3.5 The added shear stress \widehat{uv} and added heat flux \widehat{Tv} for mode R_1 (right), W_1 (middle), and L_1 (left). Top row corresponds to the supersonic $M_b = 1.5$ and the bottom row is associated with the subsonic case $M_b = 0.75$	39
3.6 History of temperature perturbation $\delta T = T_{\text{exc}} - T_{\text{unexc}}$ at the center of the forcing region at $Re_b = 3000$ and two Mach numbers, C1: $M_b = 1.5$ (left) and C2: $M_b = 0.75$ (right)	42
3.7 History of the space-averaged SEF and TEF at $Re_b = 3000$ and two Mach numbers, C1: $M_b = 1.5$ (left) and C2: $M_b = 0.75$ (right)	44
3.8 Instantaneous temperature perturbation field for acoustic excitation of supersonic turbulent boundary layer. A top view at the bottom wall at $y^+ \approx 4$ for four instances of one period within region (a) in figure 3.6 (left). The grey box indicates the region where forcing is active.	46
3.9 Instantaneous temperature perturbation field for acoustic excitation of supersonic turbulent boundary layer. A top view at the bottom wall at $y^+ \approx 4$ for four instances of one period within region (b) in figure 3.6 (left). The grey box indicates the region where forcing is active.	47
3.10 Instantaneous Q-criterion confined between the bottom wall and $y = 0.1$ in the unexcited (left) and the excited condition of C1 (right) for a supersonic turbulent channel flow at four instances of one period (\mathcal{T}). The structures are colored by their corresponding wall-normal velocity component from blue (negative) to red (positive values).	48
3.11 time- x representation of the spanwise-averaged temperature field near the bottom wall at $y^+ \approx 4$ (left) and at the channel center (right), over one pulsation cycle in the limit-cycle region.	49

Figure	Page
3.12 Contours of streaming velocity U_{st} (left) and temperature T_{st} for an acoustically excited supersonic channel flow at $Re_b = 3000$ and $M_b = 1.5$ with $A_f = 0.5$ and $\omega_f = 2\pi/4.59$ over $t/\mathcal{T} \in [10, 90]$	50
3.13 Harmonic component of streamwise velocity (top) and temperature field (bottom) in supersonic configuration	52
3.14 Harmonic component of streamwise velocity (top) and temperature field (bottom) in subsonic configuration	53
3.15 Decomposition of total Reynolds stress terms as well as turbulent heat flux into the background and harmonic terms for supersonic configuration .	54
3.16 Decomposition of total Reynolds stress terms as well as turbulent heat flux into the background and harmonic terms for subsonic configuration . .	55
3.17 Phase-locked averaged temperature contours (at $t/\mathcal{T} = 1/4$) for supersonic (C1) and subsonic cases (C2) (a&e, respectively). Maximum and minimum values are truncated for better visualization. Spatial DFT of this field is illustrated in (b&f). Amplitude of the dominant mode ($k = 0.5$) is shown in (c&g) along with the temperature eigenfunction of the most unstable mode identified by LSA. Same procedure is repeated for the streamwise velocity in (d&h).	56
3.18 History of SEF and TEF (left) as well as temperature perturbation δT at the center of the forcing region (right) at $M_b = 1.5$ subjected to off-design excitation frequencies, case C3 in table 3.1 with $\omega_f = 2\pi/4.00$ is represented by black and case C4 with $\omega_f = 2\pi/5.00$ is shown as grey; on the left SEF (— · · —) and TEF (——) overlap throughout the process. .	57
3.19 Temporal evolution of temperature fluctuations (δT) at the center of the forcing region, $y = 1$, at four different forcing amplitudes. This quantity is spatially averaged within $x \in [1.87 - 2.37]$ and $z \in [0, 1.5\pi]$ (right). Wave heights in the start-up as well as the limit-cycle regions are reported on the plots. History of SEF (— · · —) and TEF (——) are also presented as a function of pulsation period (left). Plots (a and b) represent the case C2 with $A_f=0.25$, and (c and d) refer to the case A1 with $A_f = 0.125$. (e and f) and (g and h) are respectively associated with the cases A2 where $A_f = 0.0625$ and A3 where $A_f = 0.03125$. $\overline{\text{TEF}}$ (· · · · ·) and $\overline{\text{SEF}}$ (· · · · ·) taken over the last 25 cycles along with the offset between these two quantities are reported on the graphs.	60

Figure	Page
3.20 Second-order turbulent statistics at $Re_b = 3000$ and $M_b = 0.75$ subjected to excitation at different forcing amplitudes; unexcited case (- - -), A3 with $A_f = 0.031$ (●), A2 with $A_f = 0.062$ (■), A1 with $A_f = 0.125$ (▲) and C1 with $A_f = 0.250$ (◆). Time-averaging is taken over the first 50 pulsation periods and spatially averaged in streamwise and spanwise directions.	61
3.21 Response of an acoustically excited channel flow at $Re_b = 3000$ and $M_b = 0.75$ to sudden de-activation of forcing source. The system is initially subjected to the acoustic excitation at $A_f = 0.25$ and $\omega_f = 2\pi/6.94$. History of temperature perturbations δT (bottom) and SEF and TEF (top).62	62
3.22 History of space-averaged Enhancement Factors (left) and temperature fluctuations at the channel center within the forcing region (right) at $Re_b = 6000$ and $M_b = 0.75$. Forcing function is shown in Equation (3.1) with $A_f = 0.25$ and $\omega_f = 2\pi/6.954$. SEF (- - -), TEF (—), \overline{TEF} (.....), and \overline{SEF} (.....)	63
3.23 Instantaneous temperature field for an acoustically excited subsonic turbulent channel flow at $Re_b = 6000$ and $M_b = 0.75$. Top view at the bottom wall $y^+ \approx 4$ at four instances of one period. Top and bottom row respectively correspond to the unexcited and excited cases.	63
3.24 History of Shear and Thermal Enhancement Factors (a&c) as well as temperature perturbations δT at the channel center within the forcing region (b&c) for acoustically excited channels with length $L_x = 6\pi$ (top) and 8π (bottom). On the left, solid line refers to the TEF and dash-dotted line shows the SEF. Time-averaged value of these two quantities, taken over the last 10 cycles, are plotted with red and blue dotted-lines, respectively. Both cases show the resonance and a higher TEF compared to SEF (color online).	65
4.1 Proposed setup to analyze the acoustic excitation in the spanwise direction. Acoustic drivers are active in the entire shaded area. The effect of acoustic drivers mounted on side-walls operating 180° out of phase is modeled via forcing function of form (4.1)	66

Figure	Page
4.2 History of the space-averaged SEF (— · · —) and TEF (—) (3.4) (left) and spanwise velocity perturbations (δw) at the channel centers for cases C1 to 4; (a&b): $\omega_f = 2\pi/20$, (c&d): $\omega_f = 2\pi/40$, (e&f): $\omega_f = 2\pi/80$, (g&h): $\omega_f = 2\pi/120$ at $Re_b = 3000$, $M_b = 1.5$. In all the cases studied here, the forcing amplitude is constant $A_f = 0.05$. Time-averaged \overline{TEF} taken during the limit-cycle oscillations is shown on all plots via a dashed-line (- - -) and the changes in this quantity due to excitation is reported on the graphs. Moreover, the wave height corresponding to δw in each case is also denoted on the right column.	70
4.3 Temperature fields near the bottom wall at $y^+ \approx 4$. Simulations are performed at $Re_b = 3000$ and $M_b = 1.5$; excited case at $A_f = 0.05$ and $\mathcal{T} = 20$, corresponding to case C1 (right), unexcited case (middle), and temperature perturbation, δT (left). Each row corresponds to one instance within the first period of the limit cycle oscillations; from top to bottom $t/\mathcal{T} = 0$, $t/\mathcal{T} = 1/4$, $t/\mathcal{T} = 2/4$, and $t/\mathcal{T} = 3/4$	72
4.4 Temperature fields near the bottom wall at $y^+ \approx 4$. Simulations are performed at $Re_b = 3000$ and $M_b = 1.5$; excited case at $A_f = 0.05$ and $\mathcal{T} = 40$, corresponding to case C2 (right), unexcited case (middle), and temperature perturbation, δT (left). Each row corresponds to one instance within the first period of the limit cycle oscillations; from top to bottom $t/\mathcal{T} = 0$, $t/\mathcal{T} = 1/4$, $t/\mathcal{T} = 2/4$, and $t/\mathcal{T} = 3/4$	73
4.5 Temperature fields near the bottom wall at $y^+ \approx 4$. Simulations are performed at $Re_b = 3000$ and $M_b = 1.5$; excited case at $A_f = 0.05$ and $\mathcal{T} = 80$, corresponding to case C3 (right), unexcited case (middle), and temperature perturbation, δT (left). Each row corresponds to one instance within the first period of the limit cycle oscillations; from top to bottom $t/\mathcal{T} = 0$, $t/\mathcal{T} = 1/4$, $t/\mathcal{T} = 2/4$, and $t/\mathcal{T} = 3/4$	74
4.6 Instantaneous Q-criterion in a sub-domain confined between the bottom wall and $y = 0.05$ in the excited condition of C1 for a supersonic turbulent channel flow at four instances of one period (\mathcal{T}). The structures are colored by their corresponding wall-normal velocity component from blue (negative) to red (positive values).	75
4.7 Streaming velocity components in both streamwise (left) and spanwise (middle) directions along with the streaming temperature (right). Simulations are performed at $Re_b = 3000$ and $M_b = 1.5$ subjected to the spanwise forcing of form (4.1) at $A_f=0.05$ for C1: $\omega_f = 2\pi/20$ (●), C2: $\omega_f = 2\pi/40$ (■), C3: $\omega_f = 2\pi/80$ (▲), and C4: $\omega_f = 2\pi/120$ (◆)	75

- 4.8 Phase-locked averaged spanwise velocity \widetilde{W} at five different instances of one period (\mathcal{T}); (right) excitation at $\omega_f = 2\pi/80$, (middle) $\omega_f = 2\pi/40$, and (left) $\omega_f = 2\pi/20$. The vertical dashed line (---) represents the viscous penetration length $l_{\text{visc}} = 2\pi\sqrt{2\nu_w/\omega_f}$, (●) shows the starting phase of a period, i.e., $t/\mathcal{T} = 0/5$, (■) $t/\mathcal{T} = 1/5$, (▲) $t/\mathcal{T} = 2/5$, (◆) $t/\mathcal{T} = 3/5$, and (▶) $t/\mathcal{T} = 4/5$ 76
- 4.9 History of the space-averaged TEF (3.4) (left) and spanwise velocity perturbations (δw) at the channel centers for cases A1: $\mathcal{T} = 5$ (a&b), A2: $\mathcal{T} = 10$ (c&d), C1: $\mathcal{T} = 20$ (e&f) as the reference, A3: $\mathcal{T} = 40$ (g&h), A4: $\mathcal{T} = 80$ (i&j), A5: $\mathcal{T} = 120$ (k&l), and A6: $\mathcal{T} = 160$ (m&n) at $Re_b = 3000$, $M_b = 1.5$. In all cases forcing amplitude for each case is constant $A_f = 1/\mathcal{T}$. The wave height (min-to-max value) corresponding to each case is also denoted on each plot. Time-averaged $\overline{\text{TEF}}$ taken during the limit-cycle oscillations is reported on all plots via dashed-line (---) and the changes in this quantity due to excitation is printed on the graphs. 79
- 4.10 Phase-locked averaged spanwise velocity \widetilde{W} at five different instances of one period (\mathcal{T}); (right) excitation at $\omega_f = 2\pi/80$ and $A_f = 0.0125$, (middle) $\omega_f = 2\pi/20$ and $A_f = 0.05$, and (left) $\omega_f = 2\pi/5$ and $A_f = 0.2$. The vertical dashed line (---) represents the viscous penetration length $l_{\text{visc}} = 2\pi\sqrt{2\nu_w/\omega_f}$, (●) shows the starting phase of a period $t/\mathcal{T} = 0/5$, (■) $t/\mathcal{T} = 1/5$, (▲) $t/\mathcal{T} = 2/5$, (◆) $t/\mathcal{T} = 3/5$, and (▶) $t/\mathcal{T} = 4/5$ 80
- 4.11 Space-time correlation in the spanwise velocity, \widetilde{W} (top row), streamwise velocity, \widetilde{U} (middle row), and temperature, \widetilde{T} (bottom row) for three different excitation frequencies; $\mathcal{T} = 10$ (first column), $\mathcal{T} = 20$ (second column), $\mathcal{T} = 80$ (third column). 81
- 4.12 Streaming velocity components in both streamwise (left) and spanwise (middle) directions along with the streaming temperature (right). Simulations are performed at $Re_b = 3000$ and $M_b = 1.5$ subjected to the spanwise forcing of form (4.1) at $A_f\mathcal{T} = 1$ A1: $\omega_f = 2\pi/5$ and $A_f = 0.2$ (●), A2: $\omega_f = 2\pi/10$ and $A_f = 0.1$ (■), C1: $\omega_f = 2\pi/20$ and $A_f = 0.05$ (▲), and A5: $\omega_f = 2\pi/120$ and $A_f = 0.00834$ (◆) 81
- 4.13 Second-order turbulent statistics at $Re_b = 3000$ and $M_b = 1.5$ subjected to the spanwise excitation at $A_f\mathcal{T} = 1$; unexcited case (---), A1: $\omega_f = 2\pi/5$ and $A_f = 0.2$ (●), A2: $\omega_f = 2\pi/10$ and $A_f = 0.1$ (■), C1: $\omega_f = 2\pi/20$ and $A_f = 0.05$ (▲), and A5: $\omega_f = 2\pi/120$ and $A_f = 0.00834$ (◆) . . . 83

Figure	Page
4.14 Temperature fields near the bottom wall at $y^+ \approx 4$. Simulations are performed at $Re_b = 3000$ and $M_b = 1.5$; excited case at $A_f = 0.0125$ and $\mathcal{T} = 80$, corresponding to A4 (right), unexcited case (middle), and temperature perturbation, δT (left). Each row corresponds to one instance within the first period of the limit cycle oscillations; from top to bottom $t/\mathcal{T} = 0$, $t/\mathcal{T} = 1/4$, $t/\mathcal{T} = 2/4$, and $t/\mathcal{T} = 3/4$	84
5.1 The schematic view of the computational setup for the validation study (left) and the present test case for acoustic excitation of spatially-developing boundary layer (right). The blue shaded area represents the region where the sponge layer is active in the streamwise direction, recycling the outlet to the inlet condition and the red shaded area shows the wall-normal sponge-layer enforcing the free-stream condition. The gray planes illustrate the walls and thick black lines	86
5.2 Comparison of skin friction coefficient, C_f , calculated in the present study against the DNS results of Sayadi et al [62] (left). Our Large Eddy Simulation is performed on a grid of size $N_x \times N_y \times N_z = 960 \times 160 \times 64$, while the DNS of Sayadi et al [62] has $N_x \times N_y \times N_z = 4096 \times 550 \times 512$ grid points. Time averaged streamwise flow velocity scaled with the free stream speed of sound calculated using LES (right)	88
5.3 Skin friction coefficient, C_f , along the bottom wall where $Re_x \in [0.7 \times 10^5 - 14.6 \times 10^5]$ using LES on a $N_x \times N_y \times N_z = 960 \times 160 \times 64$ grid (left). Time averaged streamwise flow velocity scaled with the free stream speed of sound in the spatially developing channel (right). Operating conditions are reported in (5.4).	90
5.4 Schematic view of the computational setup for the Linear Stability Analysis as well as the imposed boundary conditions. The shaded blue region represents the sponge zone <i>implemented in the base flow calculations</i> . Vertical dashed lines (- - -) indicate the location where the LSA's boundary conditions are applied and the red dot is the starting point of the suction and blowing <i>in the base flow calculations</i>	91
5.5 Eigenspectrum associated with the base flow described in section 5.2 subjected to the boundary conditions shown in figure 5.4. Due to the symmetric nature of eigenspectrum around $\mathcal{R}(\omega)$, only the right side is shown. Three modes are highlighted here; M0 representing a stationary mode, M1 belonging to a family of unstable modes, and M2 as the least stable mode.	92
5.6 Mode shear stress, \widehat{uv} , (—) and heat flux, \widehat{Tv} , (- - -) for M0, M1, and M2 identified in figure 5.5. Profiles are plotted along the channel height at the mid-plate $x = 0.151$	92

Figure	Page
5.7 Streamwise velocity and temperature eigenfunctions, respectively \hat{u} and \hat{T} associated with mode M2 in figure 5.5.	93
5.8 Skin friction coefficient C_f in the excited ($-\cdot\cdot-$) and unexcited ($-$) cases along the channel (left). Shear Enhancement Factor, SEF, ($-\cdot\cdot-$) as well as Thermal Enhancement Factor, TEF, ($-$) for the acoustically excited spatially developing boundary layer. The gray shaded areas show the region where the forcing amplitude $> 0.01A_f$	95
5.9 Temporal evolution of temperature perturbation at the channel center scaled by the local static temperature, T_{cl} (left). The dashed line ($- - -$) tracks the maximal and minimal values of each cycle. History of SEF ($-\cdot\cdot-$) and TEF($-$) averaged over the entire bottom wall, excluding the sponge zones, for eight pulsation periods (right). Segments highlighted with red represent the phases in one period where TEF is larger than SEF, highlighted in blue	96
5.10 Streaming temperature, T_{st} , (left) and streaming velocity in streamwise direction, U_{st} (right) normalized by the center-line values. The gray shaded region shows the area where forcing amplitude $> 0.01A_f$	96
5.11 Phase-locked averaged skin friction coefficient, C_f , (left) and Nu (right) at four different instances of one excitation period (\mathcal{T}). The reference values corresponding to the time-averaged $\overline{C_f}$ and \overline{Nu} of the unexcited case are plotted with dashed-lines ($- - -$). The gray-shaded area indicates the region where the forcing amplitude $> 0.01A_f$. Each row corresponds to one instance; top row: $t/\mathcal{T} = 0/4$, second row: $t/\mathcal{T} = 1/4$, third row: $t/\mathcal{T} = 2/4$, and the bottom row: $t/\mathcal{T} = 3/4$	97
5.12 Instantaneous iso-value contours of Q-criterion in the excited condition at four instances of one period (\mathcal{T}). The structures are colored by their corresponding wall-normal velocity component from blue (negative) to red (positive values).	99

ABSTRACT

Rahbari, Iman Ph.D., Purdue University, December 2019. Acoustic Streaming in Compressible Turbulent Boundary Layers. Major Professor: Guillermo Paniagua, School of Mechanical Engineering.

The growing need to improve the power density of compact thermal systems necessitates developing new techniques to modulate the convective heat transfer efficiently. In the present research, acoustic streaming is evaluated as a potential technology to achieve this objective. Numerical simulations using the linearized and fully non-linear Navier-Stokes equations are employed to characterize the physics underlying this process. The linearized Navier-Stokes equations accurately replicate the low-frequency flow unsteadiness, which is used to find the optimal control parameters. Local and global stability analysis tools were developed to identify the modes with a global and positive heat transfer effect.

High-fidelity numerical simulations are performed to evaluate the effect of the excitation at selected frequencies, directed by the linear stability analysis, on the heat and momentum transport in the flow. Results indicate that, under favorable conditions, superimposing an acoustic wave, traveling along with the flow, can *resonate* within the domain and lead to a significant heat transfer enhancement with minimal skin friction losses. Two main flow configurations are considered; at the fixed Reynolds number $Re_b = 3000$, in the supersonic case, 10.1% heat transfer enhancement is achieved by an 8.4% skin friction increase; however, in the subsonic case, 10% enhancement in heat transfer only caused a 5.3% increase to the skin friction. The deviation between these two quantities suggests a violation of the Reynolds analogy. This study is extended to include a larger Reynolds number, namely $Re_b = 6000$ at $M_b = 0.75$ and a similar response is observed. The effect of excitation amplitude and

frequency on the resonance, limit-cycle oscillations, heat transfer, and skin friction are also investigated here.

Applying acoustic waves normal to the flow in the spanwise direction disrupts the near-wall turbulent structures that are primarily responsible for heat and momentum transport near the solid boundary. Direct numerical simulations were employed to investigate this technique in a supersonic channel flow at $M_b = 1.5$ and $Re_b = 3000$. The external excitation is applied through a periodic body force in the spanwise direction, mimicking loudspeakers placed on both walls that are operating with a 180° phase shift. By keeping the product of forcing amplitude (A_f) and pulsation period (\mathcal{T}) constant, spanwise velocity perturbations are generated with a similar amplitude at different frequencies. Under this condition, spanwise pulsations at $\mathcal{T} = 20$ and $\mathcal{T} = 10$ show up to 8% reduction in Nusselt number as well as the skin friction coefficient. Excitation at higher or lower frequencies fails to achieve such high level of modulations in heat and momentum transport processes near the walls.

In configurations involving a spatially-developing boundary layer, a computational setup that includes laminar, transitional, and turbulent regions inside the domain is considered and the impact of acoustic excitation on this flow configuration has been characterized. Large-eddy simulations with dynamic Smagorinsky sub-grid scale modeling has been implemented, due to the excessive computational cost of DNS calculations at high-Reynolds numbers. The optimal excitation frequency that resembles the mode chosen for the fully-developed case has been identified via global stability analysis. Fully non-linear simulations of the spatially-developing boundary layer subjected to the excitation at this frequency reveal an interaction between the *pulsations* and the perturbations originated from the tripping which creates a re-laminarization zone traveling downstream. Such technique can locally enhance or reduce the heat transfer along the walls.

1. INTRODUCTION

The growing need to improve the power density of compact thermal systems necessitates developing new techniques to modulate the convective heat transfer efficiently. In the present research, acoustic streaming is evaluated as a potential technology to achieve this objective. Numerical Simulations using the linearized and fully non-linear Navier-Stokes equations are employed to characterize the physics underlying this process.

1.1 Literature Review

Acoustic streaming is broadly referred to a steady flow field induced in the flow passage by fluctuating acoustic waves. This process has been widely investigated in the past few decades thanks to its abundant applications across the disciplines, including microfluidics [1], ocean engineering [2], and thermoacoustics [3]. Extensive reviews on different mechanisms driving the acoustic streaming are given in Riley [4] and Boluriaan and Morris [5]. In the present research, we focus on the steady streaming that appear in straight channels due to an external pulsation.

When an acoustic wave passes over a solid boundary, a thin region near the wall is observed wherein the viscous effect on the wave decays exponentially. This layer is known as the *Stokes Layer*, and its thickness reads $\delta_s = \sqrt{2\nu/\omega_f}$, where ν and ω_f indicate the kinematic viscosity and angular velocity of the wave, respectively. Under favorable conditions, such acoustic waves can lead to the *steady (acoustic) streaming*.

Rayleigh [6] who studied the acoustic streaming between two parallel plates, as a result of a longitudinal standing wave, found the *outer-streaming* velocity proportional to M_a^2 , where $M_a = \tilde{U}/c_0$ is acoustic Mach number, \tilde{U} is the amplitude of velocity oscillations at the source and c_0 represents the speed of sound. Later, Schlichting [7]

extended this work to analyze the streaming within an incompressible oscillating boundary layer and suggested that the *inner-streaming* velocity is also of the order of M_a^2 , $\mathcal{O}(M_a^2)$. These theoretical approaches were derived only for very small oscillation amplitudes. To assess if the non-linear effects due to large oscillations are significant, Menguy and Gilbert [8] introduced a non-linear Reynolds number $Re_{nl} = 2M_a^2/Sh^2$, where $Sh = \delta_s/\sqrt{2}\delta$ is the shear number and δ represent the channel half-width (half the distance between two parallel plates). The theoretical streaming velocity equations mentioned above are only valid if $Re_{nl} \ll 1$. Therefore, in practical cases, employing a direct simulation of Navier-Stokes equations may be necessary. Yano [9] solved 2D compressible Navier-Stokes and energy equations to simulate the streaming in a half wave-length standing wave resonator. He showed that unless at very high frequency or in highly viscous fluids, the amplitude of oscillations initially grows at the rate $\mathcal{O}(M_a t)$ and reaches a quasi-steady state with periodic shock-waves of amplitude $\mathcal{O}(\sqrt{M_a})$. In this case, streaming velocity is proportional to M_a .

Acoustic streaming has also been used for heat transfer enhancement. Vainshtein et al. [10] considered a longitudinal standing wave formed between two parallel plates kept at different temperatures and studied the effect of streaming on the heat transfer in this gap. They observed that such mechanism can enhance the heat transfer up to one order of magnitude compared to the case with only still air. Aktas et al. [11] studied the heat transfer in a shallow enclosure where horizontal walls are adiabatic and side walls are kept at different temperatures where one side-wall oscillates at the resonant and off-design frequencies. Under the resonant conditions, the streaming velocity becomes significant, and the time-averaged convective heat transfer coefficient (\bar{h}) near the stationary wall increases by almost one order of magnitude. On the contrary, off-design oscillations fail to create a sensible streaming velocity or a considerable change in \bar{h} , therefore indicating the significance of resonance in creating time-averaged changes in the flow. Aktas and Ozgumus [12] extended this work to higher Re_{nl} and observed shock-wave oscillations (similar to Yano [9]) in the channel.

They also investigated how the formation of the streaming pattern can enhance the heat transport between two fixed horizontal parallel plates.

All the aforementioned studies were carried out for the *pure oscillatory* cases, while in *pulsating flows*, the Stokes layer interacts with the background hydrodynamics and thermal boundary layers in a non-linear fashion. Two dimensionless parameters are conventionally introduced to study such phenomenon; ratio of the external wave amplitude to the bulk velocity of the background flow $a_w = \tilde{U}/U_b$ and normalized wave frequency $\omega_f^+ = \omega_f \nu / u_\tau^2$, where $u_\tau = \sqrt{\tau_w / \rho}$ is the friction velocity. As long as a_w is less than 1, parameter ω_f^+ mainly determines the flow regime [13], [14].

- Quasi-Laminar: At high frequencies (where $0.02 \lesssim \omega^+ \lesssim 0.04$), the edge of the Stokes layer falls within the viscous sub-layer where turbulent mixing is minimum. In this regime, the acoustic waves interact with the flow only through mean quantities. In other words, the period of oscillations is shorter than turbulence timescales; therefore, these waves may not be modulated by such turbulent structures.
- Quasi-Steady: At low frequencies pulsations (where $0.003 \lesssim \omega^+ \lesssim 0.006$), Stokes layer's edge may reside in the buffer layer where turbulent mixing is important. As such, a portion of acoustic energy is extracted from the wave and distributed among smaller turbulent structures [15]. This non-linear process greatly impacts the oscillatory wave, and under specific conditions, may alter the time-averaged velocity and temperature profiles [13].
- Very high-frequency: A very high-frequency regime ($0.04 \lesssim \omega^+$) has been identified where pulsations can make noticeable changes in time-averaged turbulent flow properties. Several studies, including Tardu et al. [16] and Scotti and Piomelli [14], attributed such behavior to the pairing of pulsation frequency and bursting frequency of coherent structures in the inner-layer suggested by Mizushima et al. [17]. This observation is supported by results of Havemann and Rao [18], Habib et al [19] and Said et al [20].

1.2 Research Objectives

The Stokes layer, formed as a result of passing a sound wave over a solid boundary, interacts with the hydrodynamic and thermal boundary layers. This process, under favorable conditions, creates the *acoustic streaming*, which modifies the near-wall gradients and controls the heat and momentum transport through the boundary. The first objective of this research is to **develop adequate mathematical tools** to study acoustic wave-boundary layer interaction.

Utilizing these tools, the first target of this research is to achieve a **heat transfer enhancement using acoustic streaming** and unveil its application in designing compact thermal systems.

The next objective is to numerically **demonstrate the heat transfer abatement via applying acoustic waves** and to identify the underlying mechanism.

Evaluation of acoustic streaming in a spatially developing boundary layer and its impact on the heat and momentum transport in such configurations is the other objective of the present research.

1.3 Research Methodology

In order to fulfill the above-mentioned objectives, the present research has been divided into four work packages. In the first part, a **Local Stability solver based on the spectral method** and a **Global Stability solver based on compact scheme** are developed to obtain accurate information regarding the low-frequency characteristics of the flow and a **high-order compact finite difference solver** is employed for **Direct and Large Eddy Simulation of the acoustic wave and turbulence interaction**.

In the second task, Linear Stability Analysis is used to identify the optimal conditions where **imposing streamwise acoustic waves** can interact with the hydrodynamic and thermal boundary layers and result in a global increase in heat transfer without substantial skin friction augmentation. Direct Numerical Simulation is

performed to assess this technique and extend the findings to the conditions where non-linear interactions become dominant.

A similar procedure is pursued to utilize acoustic streaming in heat transfer abatement across the boundaries. Unlike the previous section, **acoustic waves are applied in the spanwise direction**, and Direct Numerical Simulations are employed to identify the conditions where an optimal reduction in heat transfer can be achieved.

In the last work element, Global Stability Analysis is used to characterize the optimal frequency for **acoustic excitation of a spatially-developing boundary layer**. Large Eddy Simulations are then performed based on these findings aiming to investigate the effect of acoustic waves on heat and momentum transport in a spatially-developing flow field.

1.4 Research Guideline

Chapter 2 introduces the numerical techniques employed in this research; high-order spatial discretization and time-stepping methods utilized in solving the Navier-Stokes equations are presented in section 2.2. Linearized Navier-Stokes equations are presented in section 2.3 followed by the discussion on the employed numerical techniques in sections 2.4 and 2.5. Chapter 3 proposes a methodology to superimpose the acoustic waves parallel to the fully-developed compressible boundary layers with the aim of enhancing the heat transfer with minimal skin friction losses. Linear Stability analysis framework developed in this research is employed to find the optimum wave frequency accompanied by a detailed non-linear analysis of acoustic wave-boundary layer interaction. The role of resonance, excitation amplitude, Reynolds number, and domain size in the streaming process is assessed by considering a comprehensive set of simulations.

Chapter 4 explores the superposition of acoustic waves to the compressible boundary layer, in the spanwise direction and its impact on the heat transfer reduction.

Chapter 5 aims at extending the analysis conducted for the excitation of fully-developed channel flow via resonating acoustic waves traveling along with the flow, to include the spatially-developing boundary layer. Finally, the main conclusions drawn from this study are summarized in chapter 6.

2. NUMERICAL METHODS

In this chapter, numerical tools developed for the simulation of acoustic excitation of compressible boundary layers are briefly explained. Fully non-linear Navier Stokes and continuity equations are presented in section (2.1) followed by discussions, in section (2.2), on the numerical scheme employed to solve these equations. Section 2.3 introduces the linearized Navier-Stokes equations and outlines the numerical techniques considered to solve them.

The content of this chapter is, in part (Sections 2.3, 2.4, and 2.5), reproduced with permission from:

Rahbari, I., & Scalo, C. (2017). Linear Stability Analysis of Compressible Channel Flow over Porous Walls. In *Whither Turbulence and Big Data in the 21st Century?* (pp. 451-467). Springer, Cham [21].

Rahbari, I., & Scalo, C. (2017). Quasi-Spectral Sparse Bi-Global Stability Analysis of Compressible Channel Flow over Complex Impedance. In *55th AIAA Aerospace Sciences Meeting* (p. 1879) [22].

2.1 Fully-compressible Navier-Stokes Equations

Fully compressible continuity, momentum and energy equations in the Cartesian coordinate system takes the non-dimensional form as:

$$\begin{aligned} \frac{\partial \rho}{\partial t} + \frac{\partial}{\partial x_j}(\rho u_j) &= 0 \\ \frac{\partial}{\partial t}(\rho u_i) + \frac{\partial}{\partial x_j}(\rho u_i u_j) &= -\frac{\partial p}{\partial x_i} + \frac{1}{Re} \frac{\partial}{\partial x_j}(\tau_{ij}) + f_i \delta_{1i} \quad , \text{ where } i, j \in \{1, 2, 3\} \\ \frac{\partial E}{\partial t} + \frac{\partial}{\partial x_j}[(E + p)u_j] &= \frac{1}{Re} \frac{\partial}{\partial x_j} \left(k \frac{\partial T}{\partial x_j} \right) + \frac{1}{Re} \frac{\partial}{\partial x_k}(\tau_{jk} u_j) + f_i u_i \delta_{1i} \end{aligned} \tag{2.1}$$

where $(x_1, x_2, x_3) = (x, y, z)$ represent streamwise, wall-normal, and spanwise direction and $f_i \delta_{1i}$ indicates a volume forcing in x-direction. Total energy (E) and viscous stress tensor (τ^{ij}) read:

$$E = \frac{p}{\gamma - 1} + \frac{1}{2} \rho u_i u_i, \quad \tau_{ij} = \mu \left(\frac{\partial u_i}{\partial x_j} + \frac{\partial u_j}{\partial x_i} - \frac{2}{3} \frac{\partial u_k}{\partial x_k} \delta_{ij} \right) \quad (2.2)$$

where the molecular dynamic viscosity follows the exponential form $\mu/\mu_w = (T/T_w)^{0.7}$. This set of equations is closed by considering the equation of state for the perfect gas.

In fully-developed channel flow simulations, wall temperature T_w^* , speed of sound at wall temperature c_w^* , bulk density ρ_b^* , and channel half-width δ^* are taken as the reference values for temperature, velocity, density and length scales, respectively. Viscosity at the wall temperature, μ_w , is considered as the reference value for this quantity. Equation of state in this case takes the form $p = \frac{1}{\gamma} \rho T$. This non-dimensionalization is adopted following Coleman et al. [23].

For numerical simulations involving the spatially developing boundary layer, temperature is scaled by $(\gamma - 1)T_\infty^*$, and velocity, density, and pressure with respect to c_∞^* , ρ_∞^* and $\rho_\infty^* c_\infty^{*2}$ where subscript ∞ represents the free-stream condition. For non-dimensionalization purposes, in simulation of fluid flow at the entrance region of a channel, center-line quantities, $(\)_{cl}$, replace the free-stream quantities. Therefore, the dimensionless equation of state reads $p = \frac{\gamma-1}{\gamma} \rho T$. This non-dimensionalization follows Nagarajan et. al [24].

2.2 Numerical Methods for Navier Stokes Simulations

In the present study, the high-order compact finite difference scheme on a staggered grid arrangement is utilized for spatial discretization of Navier-Stokes equations. Time-advancement is carried out via an explicit Runge-Kutta or an implicit Beam-Warming method. These numerical techniques are briefly introduced in this section; however, a complete explanation can be found in [25].

2.2.1 Compact Finite Difference Method

The governing system of equations is discretized in space using a high-order compact finite difference scheme. Conventionally, the first derivative is approximated by [26]:

$$\hat{\alpha}f'_{i-1} + f'_i + \hat{\alpha}f'_{i+1} = b\frac{f_{i+2} - f_{i-2}}{4\Delta x} + a\frac{f_{i+1} - f_{i-1}}{2\Delta x} \quad (2.3)$$

where $a = \frac{2}{3}(2 + \hat{\alpha})$ and $b = \frac{1}{3}(-1 + 4\hat{\alpha})$. This formula leads to a sixth-order accurate method by setting $\hat{\alpha} = 1/3$. The second derivative is given by

$$\hat{\alpha}f''_{i-1} + f''_i + \hat{\alpha}f''_{i+1} = b\frac{f_{i+2} - f_{i-2}}{4\Delta x^2} + a\frac{f_{i+1} - f_{i-1}}{\Delta x^2} \quad (2.4)$$

where $a = \frac{4}{3}(1 - \hat{\alpha})$ and $b = \frac{1}{3}(-1 + 10\hat{\alpha})$. To achieve the formal sixth-order accuracy, $\hat{\alpha} = 1/3$ should be considered. This family of high-order schemes is later extended to the staggered grid arrangement by Nagarajan et al. [27] providing a substantially improved accuracy over the conventional technique. Following this method, the first derivative is obtained by:

$$\hat{\alpha}f'_{i-1} + f'_i + \hat{\alpha}f'_{i+1} = b\frac{f_{i+3/2} - f_{i-3/2}}{3\Delta x} + a\frac{f_{j+1/2} - f_{j-1/2}}{\Delta x} \quad (2.5)$$

where $a = \frac{2}{3}(2 + \hat{\alpha})$ and $b = \frac{1}{3}(-1 + 4\hat{\alpha})$ and the sixth-order accuracy is recovered by assuming $\hat{\alpha} = 9/62$. This scheme requires interpolations between the nodal and mid-points which, to retain the formal accuracy, is found via

$$\hat{\alpha}f^I_{i-1} + f^I_i + \hat{\alpha}f^I_{i+1} = b\frac{f_{i+3/2} - f_{i-3/2}}{2} + a\frac{f_{j+1/2} - f_{j-1/2}}{2} \quad (2.6)$$

where $a = \frac{1}{8}(9 + 10\hat{\alpha})$ and $b = \frac{1}{8}(-1 + 6\hat{\alpha})$. Achieving the sixth-order accurate interpolation is possible by setting $\hat{\alpha} = 3/10$. One-sided differentiation and interpolation formula for near boundary points are presented in [27].

2.2.2 Explicit Time Advancement

A compact third-order Runge-Kutta method is employed for explicit time-advancement. For a generic ODE of form:

$$\frac{dU}{dt} = f(y, t) \quad (2.7)$$

Time-advancement from t^n to t^{n+1} can be found following

$$\begin{aligned} U^{n+1/3} &= U^n + a_{11}\Delta t f(U^n, t^n) \\ U^{n+2/3} &= U^n + a_{21}\Delta t f(U^n, t^n) + a_{22}\Delta t f(U^{n+1/3}, t^{n+1/3}) \\ U^{n+1} &= U^n + a_{31}\Delta t f(U^n, t^n) + a_{32}\Delta t f(U^{n+2/3}, t^{n+2/3}) \end{aligned} \quad (2.8)$$

where

$$[a_{11}, a_{21}, a_{22}, a_{31}, a_{32}]^T = \left[\frac{8}{15}, \frac{1}{4}, \frac{5}{12}, \frac{1}{4}, \frac{3}{4} \right]^T$$

2.2.3 Implicit Time Advancement

Implicit time marching is performed according to the Beam and Warming formulation [28]. System of equations (2.1) can be rewritten as:

$$\frac{\partial U}{\partial t} + \frac{\partial F^j}{\partial x_j} + \frac{\partial V^{1j}}{\partial x_j} + \frac{\partial V^{2j}}{\partial x_j} = 0 \quad (2.9)$$

where F^j and V^j represent the viscous and inviscid fluxes and U is the vector of flow variables. Following [28], a second-order A-stable implicit time-advancement is employed in this study,

$$\frac{3U^{n+1} - 4U^n + U^{n-1}}{2\Delta t} = -G(U^{n+1}, t^{n+1}) \quad (2.10)$$

where

$$G = \frac{\partial F^j}{\partial x_j} + \frac{\partial V^{1j}}{\partial x_j} + \frac{\partial V^{2j}}{\partial x_j}$$

Thereafter, G^{n+1} is linearized considering:

$$G^{n+1} = G^n + \frac{\partial G^n}{\partial U} (U^{n+1} - U^n) + \mathcal{O}(\Delta t^2)$$

which leads to:

$$\left(I + \frac{2}{3} \Delta t \frac{\partial G^n}{\partial U} \right) \underbrace{(U^{n+1} - U^n)}_{\Delta U^n} = \frac{1}{3} \underbrace{(U^n - U^{n-1})}_{\Delta U^{n-1}} - \frac{2}{3} \Delta t G^n + \mathcal{O}(\Delta t^2) \quad (2.11)$$

Although this system of equations can be solved directly for ΔU^n , the computational cost of the matrix inversion becomes prohibitive in practice. To overcome this issue, following Beam and Warming [28], an iterative approach is adopted along with diagonalization of inviscid terms in x and z directions. For complete explanation on this numerical technique, one may refer to Nagarajan [25] or Beam and Warming [28].

2.2.4 Large Eddy Simulation Technique

Turbulent flows at high Reynolds numbers contain eddies with time and length scales that span over several orders of magnitude. Resolving all these scales, using Direct Numerical Simulation of Navier-Stokes equations, requires a substantial computational effort. To alleviate this issue in high-Reynolds spatially developing boundary layer, the Large-Eddy Simulation technique has been employed. Spatially filtered form of the governing equations (2.1) and (2.2) are written as:

$$\begin{aligned} \frac{\partial \check{\rho}}{\partial t} + \frac{\partial}{\partial x_j} (\check{\rho} \{u_j\}) &= 0 \\ \frac{\partial}{\partial t} (\check{\rho} \{u_i\}) + \frac{\partial}{\partial x_j} (\check{\rho} \{u_i\} \{u_j\}) &= -\frac{\partial \check{p}}{\partial x_i} + \frac{1}{Re} \frac{\partial}{\partial x_j} (\{\sigma_{ij}\}) - \frac{1}{Re} \frac{\partial}{\partial x_j} (\tau_{ij}^{\text{sgs}}) + f_i \delta_{1i} \\ \frac{\partial \check{E}}{\partial t} + \frac{\partial}{\partial x_j} \left[\overline{(E + p)} \{u_j\} \right] &= \frac{1}{Re} \frac{\partial}{\partial x_j} \left(k \frac{\partial \check{T}}{\partial x_j} \right) + \frac{1}{Re} \frac{\partial}{\partial x_k} (\{\sigma_{jk}\} \{u_j\}) \\ &\quad - \frac{1}{Re} \frac{\partial}{\partial x_k} (q_k^{\text{sgs}}) + f_i \{u_i\} \delta_{1i} \end{aligned} \quad (2.12)$$

where \sim represents the spatial filtering and $\{ \}$ is defined as Favre-filtering $\{g\} = \widetilde{\rho g} / \widetilde{\rho}$. The term $\{\sigma_{ij}\}$ refers to the resolved stress tensor, while τ_{ij}^{sgs} and q_k^{sgs} are under-resolved stress tensor and heat fluxes:

$$\tau_{ij}^{\text{sgs}} = \check{\rho} (\{u_i u_j\} - \{u_i\} \{u_j\}), \quad \text{and} \quad q_j^{\text{sgs}} = \check{\rho} (\{T u_j\} - \{T\} \{u_j\}) \quad (2.13)$$

Sub-grid stress terms are modeled via the Dynamic Smagorinsky model wherein

$$\begin{aligned} \tau_{ij}^{\text{sgs}} - \frac{1}{3} \tau_{kk}^{\text{sgs}} \delta_{ij} &= -2C^2 \Delta^2 \check{\rho} |\{S\}| \left(\{S_{ij}\} - \frac{1}{3} \{S_{kk}\} \delta_{ij} \right) \\ \tau_{kk}^{\text{sgs}} &= 2C_I \check{\rho} \Delta^2 |\{S\}|^2 \end{aligned} \quad (2.14)$$

and

$$q_j^{\text{sgs}} = -\frac{\check{\rho} C^2 \Delta^2 |\{S\}|}{Pr_t} \frac{\partial \{T\}}{\partial x_j} \quad (2.15)$$

where $|\{S\}| = \sqrt{2\{S_{ij}\}\{S_{ij}\}}$ and $S_{ij} = 1/2 (\partial u_i / \partial x_j + \partial u_j / \partial x_i)$. Parameters C , C_I , and Pr_t are found dynamically using Germano identity following Moin et al. [29] together with modifications proposed by Lilly [30]. These parameters are averaged only in spanwise direction for stability purposes. A complete derivation of these equations are presented in Nagarajan et al. [27].

2.3 Linearized Navier-Stokes Equations

Compressible Navier-Stokes equations (2.1) can be re-written in the following form:

$$\frac{\partial}{\partial t} \mathcal{M}(\mathbf{q}) + \mathcal{L}(\mathbf{q}) + \mathcal{N}(\mathbf{q}, \mathbf{q}) = 0 \quad (2.16)$$

where \mathbf{q} is a vector of primitive or conservative variables and \mathcal{L} and \mathcal{N} are respectively linear and non-linear operators. A generic instantaneous quantity, $q(x, y, z, t)$, can be

decomposed into a base state, $\bar{q}(x, y, z)$, and a small fluctuation term $\varepsilon q'(x, y, z, t)$. Applying this decomposition and retaining only the first order fluctuations yields

$$\frac{\partial}{\partial t} \mathcal{M}(\varepsilon \mathbf{q}') + \mathcal{L}(\bar{\mathbf{q}}) + \mathcal{L}(\varepsilon \mathbf{q}') + \mathcal{N}(\bar{\mathbf{q}}, \bar{\mathbf{q}}) + \mathcal{N}(\bar{\mathbf{q}}, \varepsilon \mathbf{q}') = 0 \quad (2.17)$$

Considering Equation (2.16), mean flow ($\bar{\mathbf{q}}$) satisfies:

$$\mathcal{L}(\bar{\mathbf{q}}) + \mathcal{N}(\bar{\mathbf{q}}, \bar{\mathbf{q}}) = 0 \quad (2.18)$$

Subtracting (2.18) from (2.17) yields Linearized Navier-Stokes Equations (LNSE):

$$\frac{\partial}{\partial t} \mathcal{M}(\mathbf{q}') + \mathcal{N}_{\bar{\mathbf{q}}}(\mathbf{q}') = 0 \quad (2.19)$$

To analyze the asymptotically unstable modes of the base flow, one may assume perturbations take the form:

$$q'(x, y, z, t) = \hat{q}(x, y, z) e^{-j\omega t} \quad (2.20)$$

where ω is the complex angular velocity of each mode, $\Re\{\omega\}$ is the angular velocity and $\Im\{\omega\}$ shows the growth rate of each mode. Substituting this perturbation in Equation (2.20) results in a generalized eigenvalue problem:

$$\mathbf{A}\hat{\mathbf{q}} = \omega \mathbf{B}\hat{\mathbf{q}} \quad (2.21)$$

where,

$$\begin{pmatrix} A_u^X & A_v^X & A_w^X & A_p^X & A_T^X \\ A_u^Y & A_v^Y & A_w^Y & A_p^Y & A_T^Y \\ A_u^Z & A_v^Z & A_w^Z & A_p^Z & A_T^Z \\ A_u^C & A_v^C & A_w^C & A_p^C & A_T^C \\ A_u^E & A_v^E & A_w^E & A_p^E & A_T^E \end{pmatrix} \begin{pmatrix} \hat{\mathbf{u}} \\ \hat{\mathbf{v}} \\ \hat{\mathbf{w}} \\ \hat{\mathbf{p}} \\ \hat{\mathbf{T}} \end{pmatrix} = \omega \begin{pmatrix} B_u^X & B_v^X & B_w^X & B_p^X & B_T^X \\ B_u^Y & B_v^Y & B_w^Y & B_p^Y & B_T^Y \\ B_u^Z & B_v^Z & B_w^Z & B_p^Z & B_T^Z \\ B_u^C & B_v^C & B_w^C & B_p^C & B_T^C \\ B_u^E & B_v^E & B_w^E & B_p^E & B_T^E \end{pmatrix} \begin{pmatrix} \hat{\mathbf{u}} \\ \hat{\mathbf{v}} \\ \hat{\mathbf{w}} \\ \hat{\mathbf{p}} \\ \hat{\mathbf{T}} \end{pmatrix} \quad (2.22)$$

In A and B matrices, superscripts represent the equations used to derive the coefficient and subscripts specify the quantity to which each coefficient belongs. For example, in linearized x -momentum equation, all terms that include $\hat{\mathbf{u}}$ are factorized into A_u^X . It is worth noting that these matrix elements are essentially operators that may include spatial derivatives and mean flow quantities.

If the base flow as well as boundary conditions are homogeneous in one or two directions, spatial Fourier decomposition can simplify the fluctuation forms leading to two common classes of linear stability analysis, i.e. local and global stability analysis. The following sections, introduce these subjects along with the numerical methods developed for each class.

2.4 Numerical Methods for Local Stability Analysis

In local stability analysis, the base flow is assumed to vary only in one direction, for instance, y , and boundary conditions for perturbations are considered periodic in the other two directions, namely x and z . Incorporating the spatial Fourier transform, the perturbation form (2.20) is rewritten as

$$q'(x, y, z, t) = \hat{q}(y) e^{j(kx + \beta z)} e^{-j\omega t} \quad (2.23)$$

where k and β are wavenumbers in x and z directions, respectively. Considering this form of perturbations in Equation (2.21) substantially reduces the size, and subsequently, computational cost of the eigenvalue problem. A complete derivation of the matrix elements in (2.22) for this type of stability analysis is presented in Malik [31]. A Spectral collocation method is often used for spatial discretization of Equation (2.21).

2.4.1 Spectral Method

Spectral method is a common scheme to discretize the linear Navier-Stokes equations, especially in the local stability problems. This method approximates a variable Φ by an N -th order polynomial:

$$\Phi(\xi) = \sum_{k=0}^N a_k T_k(\xi) \quad (2.24)$$

where $T_k(\xi)$ is the Chebyshev polynomial of order k defined in $\xi \in [-1, 1]$ whose zeros (ξ_n) are calculated from

$$\xi_n = \cos(\pi n / N) \quad \text{for } n = 0, 1, 2, \dots, N \quad (2.25)$$

Derivative of Φ with respect to ξ is found via

$$\left. \frac{\partial \Phi}{\partial \xi} \right|_{\xi_i} = \sum_{k=0}^N a_k D_{i,k}(\xi) \quad (2.26)$$

where,

$$D_{0,0}^\xi = \frac{2N^2 + 1}{6} \quad (2.27)$$

$$D_{i,i}^\xi = -\frac{\xi_i}{2(1 - \xi_i^2)} \quad i = 1, \dots, N-1$$

$$D_{i,j}^\xi = \frac{c_i (-1)^{i+j}}{c_j (\xi_i - \xi_j)} \quad i \neq j, \quad i, j = 1, \dots, N-1$$

$$D_{N,N}^\xi = -\frac{2N^2 + 1}{6} \quad (2.28)$$

and

$$c_i = \begin{cases} 2 & \text{if } n = 0 \text{ or } N \\ 1 & \text{otherwise} \end{cases}$$

Higher derivative matrices can be found via matrix multiplication of the first derivative matrices, for example,

$$\bar{\rho}\hat{u} + \frac{\partial\hat{u}}{\partial y} + \frac{\partial^2\hat{u}}{\partial y^2} = \left(\bar{\rho} + \frac{\partial}{\partial y} + \frac{\partial^2}{\partial y^2}\right)\hat{u}$$

can be written in the matrix form as

$$(\bar{\rho}I + D_y + D_y^2)\hat{u}$$

This differentiation method is applied in Equations (2.21) and (2.22) and, therefore, the unknown vector becomes:

$$\begin{aligned}\hat{\mathbf{u}} &= [\hat{u}_1, \hat{u}_2, \dots, \hat{u}_n], \quad \hat{\mathbf{v}} = [\hat{v}_1, \hat{v}_2, \dots, \hat{v}_n], \quad \hat{\mathbf{w}} = [\hat{w}_1, \hat{w}_2, \dots, \hat{w}_n] \\ \hat{\mathbf{p}} &= [\hat{p}_1, \hat{p}_2, \dots, \hat{p}_n], \quad \hat{\mathbf{T}} = [\hat{T}_1, \hat{T}_2, \dots, \hat{T}_n]\end{aligned}\tag{2.29}$$

where n is the number of grid points. The resulting eigenvalue problem (2.21) has a $5n \times 5n$ dimension, and since n is typically of the order of $\mathcal{O}(100)$, it can be simply solved by a QR algorithm.

2.4.2 Validation of the Local Stability Solver

Validation is first carried out against the Local Stability Analysis results for compressible Couette flow by Hu and Zhong [32,33]. Iso-thermal conditions, $T_\infty = 1$, and the tangential velocity, U_∞ are imposed at the top wall as well as no-slip and adiabatic conditions at the bottom wall. Reynolds number and Mach number based on the top wall velocity are Re_∞ and M_∞ . In this section, all quantities are normalized with speed of sound based at the top wall temperature, bulk density and the total

wall-to-wall distance. To achieve a fair comparison with Hu and Zhong [32, 33], the equation for dynamic viscosity is changed to:

$$\mu = T^{1.5} \frac{1 + C}{T + C}, \quad \text{where } C = 0.5 \quad (2.30)$$

and $Pr = 0.72$ (only for the sake of this comparison). Excellent agreement is found as shown by the eigenvalue spectra and eigenfunctions (figures 2.1 and 2.2). A grid convergence study of the eigenvalues is presented in table 2.1. This type of stability

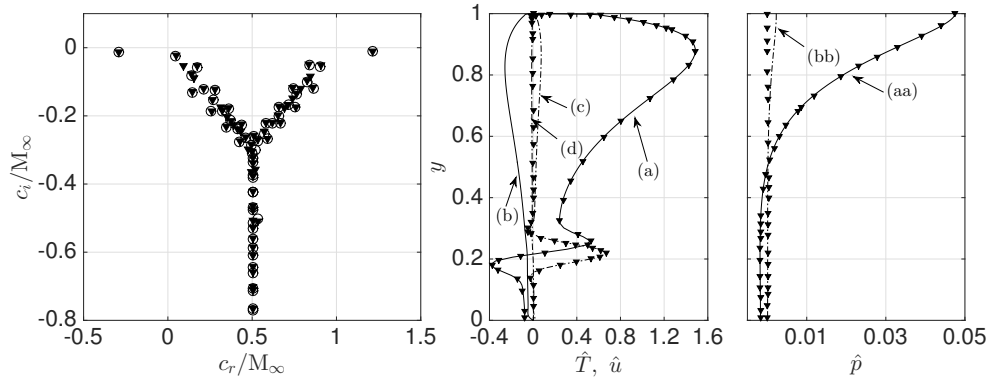


Figure 2.1. Comparison of complex wave velocity spectrum for compressible Couette flow at $\mu_\infty = 2$, $Re_\infty = 2 \times 10^5$, $k = 1$ using $N=100$ grid points (\circ) with results from Hu and Zhong [33] (\blacktriangledown). Real part (—) and imaginary part (— · —) of velocity, \hat{u} , temperature, \hat{T} , and pressure, \hat{p} , eigenfunctions of the most unstable mode at $M_\infty = 5$, $Re_\infty = 5 \times 10^5$, $\alpha = 3$ with (a): $\Re\{\hat{T}\}$, (b): $\Re\{\hat{u}\}$, (c): $\Im\{\hat{T}\}$, (d): $\Im\{\hat{u}\}$, (aa): $\Re\{\hat{p}\}$, (bb): $\Im\{\hat{p}\}$.

analysis may be useful in some applications, however, if the base flow quantities depend on more than one direction, or if the geometry cannot be represented by periodic boundary conditions for perturbation, Local Stability Analysis may not be the ideal choice.

Table 2.1.

Comparison of complex wave velocity, c , of the most unstable mode for compressible Couette flow with the reference values taken from Hu and Zhong [32] for several Re_∞ , M_∞ and k . Grid convergence study shown for $N=100$, $N=200$ and $N=300$, are respectively placed on the top, middle and bottom rows for each case.

Hu and Zhong [33]		Current Study	
c_r/M_∞	c_i/M_∞	c_r/M_∞	c_i/M_∞
Re $_\infty = 5 \times 10^6$, M $_\infty = 5$, $\alpha = 2.1$, Mode I			
+0.972869314676	-0.003456356315	+0.972869 <u>280518</u>	-0.0034563 <u>23886</u>
+0.972869272448	-0.003456466520	+0.97286927244 <u>5</u>	-0.003456466743
+0.972869272450	-0.003456466522	+0.97286927235 <u>5</u>	-0.0034564665 <u>05</u>
Re $_\infty = 5 \times 10^6$, M $_\infty = 5$, $\alpha = 2.1$, Mode 0			
+0.040730741952	+0.000876050503	+0.04073059629 <u>2</u>	+0.000874754264
+0.040722854287	+0.000885530891	+0.04072285437 <u>3</u>	+0.000885530566
+0.040722853034	+0.000885531421	+0.04072285303 <u>2</u>	+0.000885531421
Re $_\infty = 2 \times 10^5$, M $_\infty = 2$, $\alpha = 0.1$, Mode I			
+1.213965119859	-0.011585118523	+1.21396511985 <u>1</u>	-0.011585118547
+1.213965119817	-0.011585118448	+1.21396511985 <u>2</u>	-0.011585118547
+1.213965119854	-0.011585118558	+1.21396511985 <u>2</u>	-0.011585118547
Re $_\infty = 2 \times 10^5$, M $_\infty = 2$, $\alpha = 0.1$, Mode 0			
-0.291572925106	-0.013821128462	-0.29157292510 <u>9</u>	-0.013821128464
-0.291572925140	-0.013821128536	-0.29157292510 <u>9</u>	-0.013821128464
-0.291572925108	-0.013821128457	-0.29157292510 <u>9</u>	-0.013821128464

2.5 Numerical Methods for Global Stability Analysis

Global stability analysis focuses on the flow configurations where the base flow is not periodic (sometimes referred to as three-dimensional or Tri-global Stability Analysis) or can be assumed periodic only in one direction (Bi-global Stability Anal-

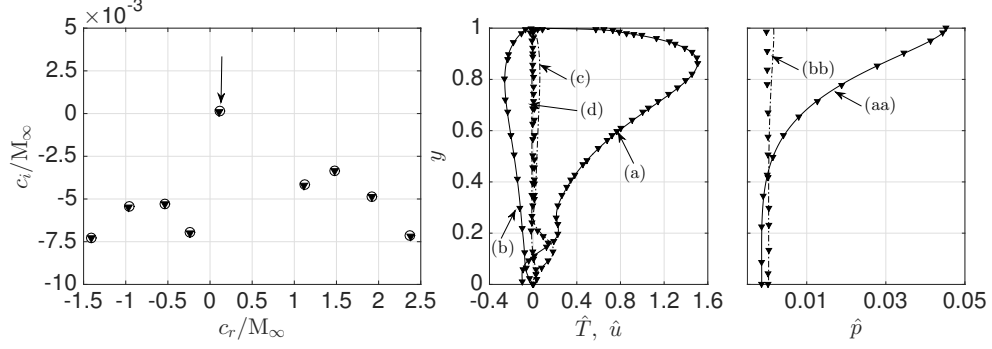


Figure 2.2. Comparison of complex phase velocity spectrum for laminar compressible Couette flow at $M_\infty = 5$, $\text{Re}_\infty = 1 \times 10^5$ and $k = 2.5$ using $N=100$ grid points (\blacktriangledown) against Hu and Zhong [32]. Real part (—) and imaginary part (— · —) of velocity, \hat{u} , temperature, \hat{T} , and pressure, \hat{p} , eigenfunctions of the most unstable mode (indicated with downward arrow) with (a): $\Re\{\hat{T}\}$, (b): $\Re\{\hat{u}\}$, (c): $\Im\{\hat{T}\}$, (d): $\Im\{\hat{u}\}$, (aa): $\Re\{\hat{p}\}$, (bb): $\Im\{\hat{p}\}$.

ysis) [34]. The former case is very computationally demanding and is not the focus of the present work. In the latter, one may consider the perturbations to take the form:

$$q'(x, y, z, t) = \hat{q}(x, y) e^{j\beta z} e^{-j\omega t} \quad (2.31)$$

assuming that the flow and boundary conditions are periodic in z -direction. For this kind of stability analysis, the elements of \mathbf{A} and \mathbf{B} matrices in Equation (2.22) are presented in Theofilis and Colonius [35].

2.5.1 Spectral Methods for GSA

Extending the one-dimensional formulation for the function estimation using the spectral method (2.24) to multiple dimensions reads,

$$\Phi(\xi, \eta) = \sum_{k=0}^{N_\xi} \sum_{l=0}^{N_\eta} a_{k,l} T_k(\xi) T_l(\eta) \quad (2.32)$$

where ξ and η are zeros of the Chebyshev polynomial of order N_ξ and N_η (2.25). The 1D-derivative matrix operators in each direction is found via Equation (2.27), where D matrix has $[N_\xi \times N_\xi]$ or $[N_\eta \times N_\eta]$ dimension. Two-dimensional operators are simply found via:

$$\begin{aligned} D_\xi &= D \otimes I \quad \text{and} \quad D_\eta = I \otimes D \\ D_{\xi\xi} &= D^2 \otimes I \quad \text{and} \quad D_{\eta\eta} = I \otimes D^2 \quad \text{and} \quad D_{\xi\eta} = D_\xi \times D_\eta \end{aligned} \quad (2.33)$$

It is worth noting that ξ and η are defined in $[-1, 1]$, therefore an appropriate transformation may need to be considered if the physical domain does not conform with this domain.

Applying this method to discretize the linearized Navier-Stokes equations leads to the generalized eigenvalue problem of form (2.22) and the unknown vector becomes similar to (2.29) where $n = N_\xi \times N_\eta$ and, therefore, size of the eigenvalue problem (2.21) becomes $5n \times 5n$. A **spy** plot of the **A** and **B** matrices using this discretization method are shown in figure 2.3. Given the computational cost of the QR algorithm,

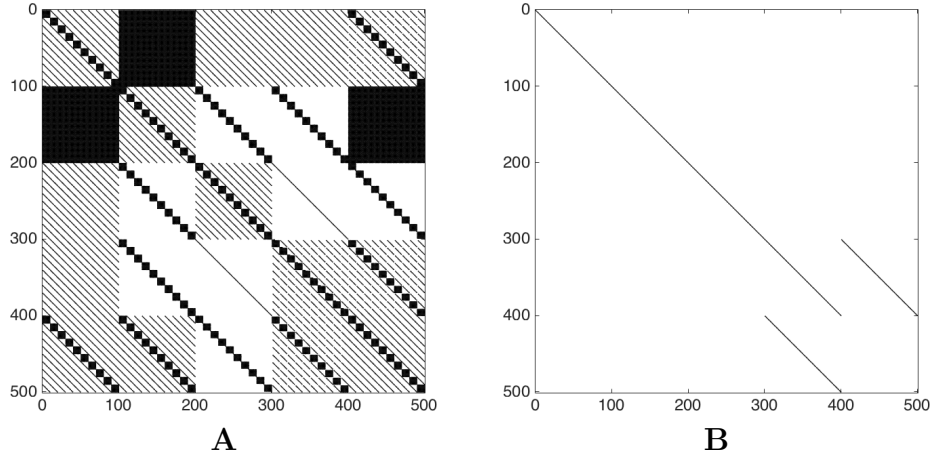


Figure 2.3. Spy plots of **A** and **B** matrices using dense implementation of compact scheme for a grid of 10×10 .

which scales with $\mathcal{O}(n^3)$, solving the Equation (2.21) soon becomes prohibitive. For

example, if we use 100 grid points in each direction, size of matrices in Global Stability Analysis is 10^2 times larger, in the leading dimension, and subsequently cost of the eigenvalue problem becomes $\mathcal{O}(10^6)$ times more expensive than Local Stability Analysis. In the other hand, due to fully dense nature of the derivative matrix operators, iterative eigenvalue solvers, e.g. Arnoldi algorithm [36], are not very effective as well, especially in terms of memory requirements. In order to have a sparse, and yet high-order, derivative operators, compact finite difference method has been chosen for this study.

2.5.2 Compact Finite Difference for GSA

Recall the first derivative approximation using compact finite difference method (2.3):

$$\hat{\alpha}f'_{i-1} + f'_i + \hat{\alpha}f'_{i+1} = \frac{b}{4\Delta x}(f_{i+2} - f_{i-2}) + \frac{a}{2\Delta x}(f_{i+1} - f_{i-1}) \quad ((2.3) \text{ revisited})$$

Following the matrix notation, this equation is rewritten as:

$$L \mathbf{f}' = R \mathbf{f} \quad (2.34)$$

Where L and R are banded tri-diagonal and penta-diagonal matrices, respectively. The discrete derivative matrix operator calculated explicitly using this scheme, $D = L^{-1}R$, is dense (see figure 2.4), therefore, demands the computational cost very similar to that of the spectral methods. In Global Stability Analysis, it is more convenient to have spatial derivatives explicitly in terms of primitive (or conservative) variables so that the unknown vector only contains the primitive variables (2.29). In the literature, whenever compact scheme is employed to discretize linearized Navier-Stokes equations, D matrix is used to find the first and second derivatives, \mathbf{f}' and \mathbf{f}'' , explicitly in terms of \mathbf{f} , (for example in [37] and [38]). This method hereafter is referred to as *explicit implementation* of compact finite difference. As such, sparsity pattern of A

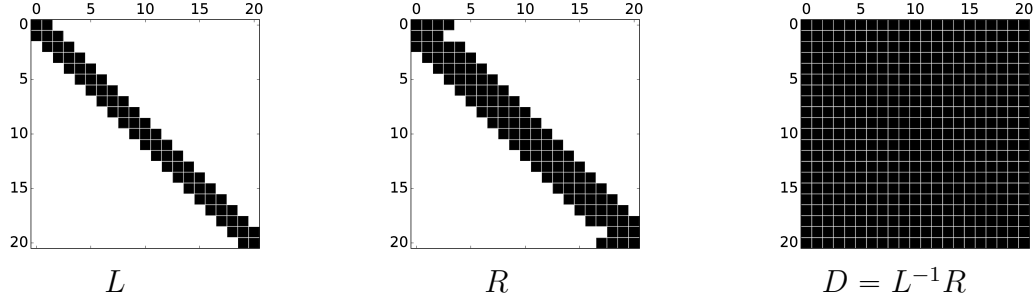


Figure 2.4. Spy plots of compact finite difference operators, L and R , and explicit derivative matrix, D . As it is shown, L and R operators are banded (tri- and penta-diagonal) matrices while the D matrix is dense.

and B matrices generated using this implementation becomes very similar to the one of spectral method shown in figure 2.3.

The optimal approach to use the compact scheme is to incorporate L and R matrices inside the system of equation without any inversion to keep the system as sparse as possible. The new implementation proposed in this research is designed to make this accomplished.

2.5.3 Sparse Implementation of Compact Finite Difference for GSA

As explained before, to fully exploit the advantages of compact schemes, one should use the sparse form, incorporating both L and R matrices when setting up the final matrices in the generalized eigenvalue problem. For this purpose, the first and

second spatial derivatives of the primitive variables are also included in the eigenvector $\hat{\mathbf{q}}$ so that, unlike Equation (2.29), the first block of unknowns, $\hat{\mathbf{u}}$, becomes:

$$\hat{\mathbf{u}} = \left[\underbrace{\hat{u}_0, \dots, \hat{u}_{n-1}}_{\hat{u}_i}, \underbrace{\hat{u}_{x0}, \dots, \hat{u}_{x_{n-1}}}_{\hat{u}_{x_i}}, \underbrace{\hat{u}_{xx0}, \dots, \hat{u}_{xx_{n-1}}}_{\hat{u}_{xx_i}}, \underbrace{\hat{u}_{xy0}, \dots, \hat{u}_{xy_{n-1}}}_{\hat{u}_{xy_i}}, \right. \\ \left. \underbrace{\hat{u}_{y0}, \dots, \hat{u}_{y_{n-1}}}_{\hat{u}_{y_i}}, \underbrace{\hat{u}_{yy0}, \dots, \hat{u}_{yy_{n-1}}}_{\hat{u}_{yy_i}} \right]^T \quad (2.35)$$

Similarly, one can form the unknown blocks for $\hat{\mathbf{v}}$ and $\hat{\mathbf{w}}$. The temperature vector, $\hat{\mathbf{T}}$, will be similar except that cross derivative does not come into the calculation:

$$\hat{\mathbf{T}} = \left[\underbrace{\hat{T}_0, \dots, \hat{T}_{n-1}}_{\hat{T}_i}, \underbrace{\hat{T}_{x0}, \dots, \hat{T}_{x_{n-1}}}_{\hat{T}_{x_i}}, \underbrace{\hat{T}_{xx0}, \dots, \hat{T}_{xx_{n-1}}}_{\hat{T}_{xx_i}}, \underbrace{\hat{T}_{y0}, \dots, \hat{T}_{y_{n-1}}}_{\hat{T}_{y_i}}, \underbrace{\hat{T}_{yy0}, \dots, \hat{T}_{yy_{n-1}}}_{\hat{T}_{yy_i}} \right]^T \quad (2.36)$$

and $\hat{\mathbf{p}}$ will be:

$$\hat{\mathbf{p}} = \left[\underbrace{\hat{p}_0, \dots, \hat{p}_{n-1}}_{\hat{p}_i}, \underbrace{\hat{p}_{x0}, \dots, \hat{p}_{x_{n-1}}}_{\hat{p}_{x_i}}, \underbrace{\hat{p}_{y0}, \dots, \hat{p}_{y_{n-1}}}_{\hat{p}_{y_i}} \right]^T \quad (2.37)$$

To set up \mathbf{A} and \mathbf{B} matrices, the linear stability equations are written at the first row blocks associated with each variable, i.e., the x and y -momentum equations are written in the rows associated with \hat{u}_i and \hat{v}_i blocks and compact derivative formulation (2.34) is incorporated in the newly appeared blocks, e.g., rows corresponding to \hat{u}_{x_i} , \hat{u}_{xx_i} . For better description of this approach, the structure of the first two blocks of \mathbf{A} matrix, A_u^X and A_v^X , are shown in figure 2.5 where L_x and R_x are compact finite difference operators (2.34) in x -direction; similarly, L_y and R_y are these operators in y -direction. The rest correspond to different terms in the linearized Navier-Stokes equations. Finally, \mathbf{A} and \mathbf{B} matrices for a 10×10 grid are shown in figure 2.6. Comparing figures 2.3 and 2.6 shows that using the new formulation, the final matrices

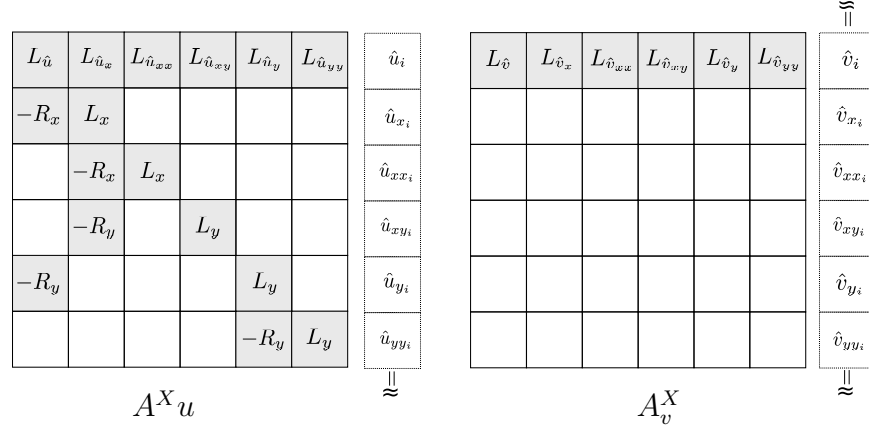


Figure 2.5. Sample structure of A_u^X and A_v^X as part of the \mathbf{A} matrix (2.22). Blocks having non-zero entries are shaded while the ones with all zero elements are left white. The corresponding segments in the array $\hat{\mathbf{q}}$ are shown in the right. L_x and R_x are compact finite difference operators (2.34) in x -direction; similarly, L_y and R_y are these operators in y - direction. The rest correspond to different terms in the linearized Navier-Stokes equations.

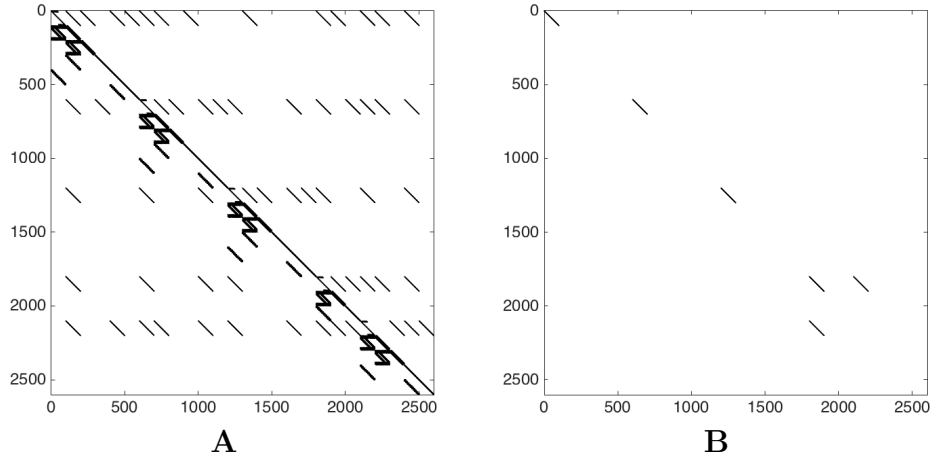


Figure 2.6. Spy plots of \mathbf{A} and \mathbf{B} matrices using the implicit(sparse) implementation of compact scheme for a grid of 10×10

are much sparser, however bigger in dimensions. The number of non-zero elements in these matrices are shown in table 2.2. The advantages of this method become more pronounced by increasing the number of grid points so that for a moderate grid size (128×128), the new approach generates matrices that are more than 280 times sparser. The generalized eigenvalue problem (2.21) is solved using SLEPc, Scalable

Table 2.2.

Comparison of number of non-zero elements, $\text{nnz}()$, in matrices **A** and **B** (2.21), generated using implicit versus explicit compact scheme implementation for a model problem

Grid Size ($N_x \times N_y$)	$\text{nnz}(A)$ Implicit	$\text{nnz}(A)$ Explicit	$\text{nnz}(B)$ Implicit	$\text{nnz}(B)$ Explicit
16×16	46,680	263,073	5,610	1,530
32×32	182,807	3,684,908	22,506	6,138
64×64	740,565	54,590,571	90,090	24,570
128×128	2,980,309	840,071,345	360,426	98,298

Library for Eigenvalue Problem Computations [39]. The Arnoldi algorithm, based on Krylov subspace iteration, is used to solve the eigenvalue problem. A brief description of this algorithm is included in the following.

Arnoldi Algorithm

Let matrix M be a generic complex valued matrix for which the decomposition $M = QHQ^*$ holds where Q and H are unitary and upper Hessenberg matrices, respectively. One can write this decomposition for the first m columns as:

$$M_{[n \times n]} Q'_{[n \times m]} = Q'_{[n \times (m+1)]} H'_{[(m+1) \times m]} \quad (2.38)$$

where prime denotes a portion of the original matrix.

$$\begin{bmatrix} M \end{bmatrix} \begin{bmatrix} q_1 & q_2 & \cdots & q_m \end{bmatrix} = \begin{bmatrix} q_1 & q_2 & \cdots & q_{m+1} \end{bmatrix} \begin{bmatrix} h_{11} & h_{12} & \cdots & h_{1m} \\ h_{21} & h_{22} & \cdots & h_{2m} \\ & \ddots & & \vdots \\ & & \ddots & \vdots \\ & & & h_{m+1,m} \end{bmatrix}$$

The basic Arnoldi algorithm uses the stabilized Gram-Schmidt process to find a sequence of orthonormal vectors, e.g. q_1, q_2, q_3, \dots , such that for every m and starting from a random b vector, $\mathcal{K}_m(M, b) = \text{span}\{q_1, q_2, \dots, q_m\}$. This algorithm can be summarized as:

Algorithm 1 Basic Arnoldi iteration algorithm

procedure BASIC ARNOLDI ITERATION ALGORITHM

selecting b arbitrarily which gives $q_1 = \frac{b}{\|b\|}$

for $m = 1, 2, \dots$ **do**

$p = Mq_m$

for $i = 1, 2, \dots, m$ **do**

$h_{im} = q_i^* p$

$p = p - h_{im} q_i$

end for

$h_{m+1,m} = \|p\|$

$q_{m+1} = \frac{p}{h_{m+1,m}}$

end for

end procedure

Removing the last row of $H'_{m+1 \times m}$ gives $\tilde{H}_{[m \times m]}$ which depending on m can be much smaller than M matrix. Eigenvalues of \tilde{H} are good approximations of those of M matrix and q_1 to q_m are the eigenvectors. The algorithm implemented in this study, through SLEPc, is a variant of the original Arnoldi algorithm called Explicitly Restarted Arnoldi with locking. More information on this can be found in the SLEPc user manual [40].

Shift-and-Invert Technique

The generalized eigenvalue problem (2.21) can be transformed into a standard eigenvalue problem:

$$\tilde{\mathbf{A}}u = \tilde{\Lambda}u \quad (2.39)$$

where $\tilde{\mathbf{A}} = (\mathbf{A} - \sigma\mathbf{B})^{-1}\mathbf{B}$ and $\tilde{\Lambda} = \frac{1}{\omega - \sigma}$. Using this transformation, the eigenvalues close to the σ become the largest in magnitude and will converge quickly in the Krylov-based algorithms. All calculations in these algorithms that require \tilde{A} are handled implicitly through PETSc so that all matrix inverse times vectors are viewed as solution of a linear system of equation. At each Krylov iteration, one system of equations should be solved, using direct scheme which is one of the most time consuming parts of the process of finding the eigenvalues. Direct solvers find the LU decomposition of the matrix and then solve for the multiple right hand sides which the later only requires a backward and forward substitutions. The distributed version of the SuperLU package is used herein which employs Message Passing Interface (MPI) to perform the Gaussian elimination in parallel [41, 42]. Matrices are partitioned so that each processor reads one block-row. Factorized matrices (L and U) are also distributed among several processors which necessitates performing the backward/forward substitutions in the distributed form that causes difficulties when using many processors.

2.5.4 Validation of the Global Stability Solver

In this section, we aim to study the accuracy of the developed Global Stability Solver in the leading edge boundary layer problem which is originally studied by Lin and Malik [43] using a spectral solver for an incompressible flow and then is extended to the compressible regime by Theofilis et al [44]. One interesting fact about this test case is the ease of calculating the base flow by solving a set of coupled Ordinary

Differential Equations, presented in equations (2.40), with high accuracy and low computational cost.

$$\begin{aligned}
 V_y &= -U + V \frac{T_y}{T} \\
 U_{yy} &= \frac{1}{\mu} \left(\frac{U^2 + V U_y}{T} - 1 - \frac{\partial \mu}{\partial T} T_y U_y \right) \\
 W_{yy} &= \frac{1}{\mu} \left(\frac{V W_y}{T} - \frac{\partial \mu}{\partial T} T_y W_y \right) \\
 T_{yy} &= \frac{Pr}{\mu} \left(-\frac{\partial \mu}{\partial T} \frac{T_y^2}{Pr} + \frac{T_y V}{T} - (\gamma - 1) M^2 \mu W_y^2 \right)
 \end{aligned} \tag{2.40}$$

This set of ODEs, subjected to the boundary conditions (2.41), is solved using the fourth-order Runge-Kutta scheme.

$$U(0) = V(0) = W(0) = 0 \quad \text{and} \quad U(\infty) = W(\infty) = T(\infty) = 1 \tag{2.41}$$

Velocity components as well as temperature base fields are calculated after solving the above-mentioned equations resulting in the base flow vector:

$$\bar{\mathbf{q}}(x, y, z) = (u, v, w, \rho, T)^T = \left(\frac{xU(y)}{\text{Re}}, \frac{V(y)}{\text{Re}}, W(y), \frac{1}{T(y)}, T(y) \right)^T \tag{2.42}$$

Linearized Navier-Stokes equations are solved at $\text{Re} = 800$, $M = 0.02$, based on span-wise velocity at the boundary layer edge, and $\beta = 0.255$. At the wall, all components of the velocity fluctuations are set to zero $(u', v', w') = 0$ as well as temperature fluctuation $T' = 0$. Zero Neumann boundary condition is imposed for pressure at the wall, $\partial p' / \partial y = 0$. At the far-field, all perturbations are assumed to decay to zero. Linear extrapolation is imposed at the left and right boundaries in x -direction.

For compact scheme, two consecutive grid transformations are used to map the uniform grid (in wall-normal direction denoted by $\chi \in [-1, 1]$) to the one used by Lin and Malik [43] in order to achieve a fair comparison. The first one, $\eta = \tanh(\gamma\chi)/\tanh(\chi)$ with $\gamma = 2$, provides a non-uniform grid with points clustered near

the boundaries, while the second transformation places half of the points in a very small distance adjacent to the wall (determined by y_i):

$$y = a \frac{1 + \eta}{b - \eta} \quad \text{where} \quad a = \frac{y_i y_\infty}{(y_\infty - 2y_i)} \quad \text{and} \quad b = 1 + \frac{2a}{y_\infty} \quad (2.43)$$

In the current study, $y_i = 0.5$ and $y_\infty = 100$ are considered. In x direction, a uniform grid is considered, $x \in [-100, 100]$. Eigenvalues of the first and second most unstable modes on a 48×48 grid are presented in the table 2.3 which indicates the accuracy of the developed code using compact scheme in Linear Stability Analysis. Number of non-zero elements after LU decomposition and total memory highmark

Table 2.3.

Global stability analysis of leading edge boundary layer at $Re = 800$, $M = 0.02$ and $\beta = 0.255$ on a 48×48 grid where $c_i = \omega_i/\beta$ and $c_r = \omega_r/\beta$. Subscripts GH and A1 represent the Görtler-Hämmerlin and first anti-symmetric modes. Deviating digits are underlined.

Grid: 48×48	c_{rGH}	c_{iGH}	c_{rA1}	c_{iA1}
Lin and Malik [43]	0.35840982	0.00585325	0.35791970	0.00409887
Theofilis et al. [44]	0.35844151	0.00585646	0.35793726	0.00401330
Current Study: implicit	0.358440 <u>71</u>	0.00585 <u>467</u>	0.3579 <u>5061</u>	0.00410000
Current Study: explicit	0.358444 <u>57</u>	0.00584 <u>620</u>	0.3579 <u>5353</u>	0.004091 <u>83</u>

for two different implementations of compact scheme are presented in figure 2.7. Explicit (traditional) implementation, similar to the spectral method implementation, demands much more memory such that the eigenvalue computations on the grids finer than 80×80 is not possible on our machines, however, computations on grid 200×200 are easily done using the new implementation.

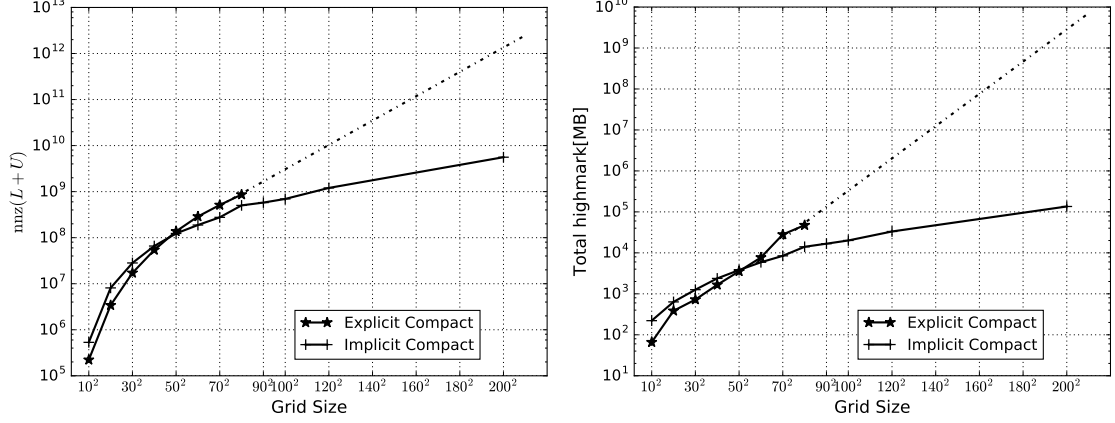


Figure 2.7. Total number of non-zero elements (left) and total highmark (right) for implicit and explicit implementations of compact scheme

2.6 Application of the Linear Stability Analysis in Turbulent Flow Simulations

Linear Stability Analysis involves approximation of flow quantities around an *equilibrium* or *base* state. In case the background flow is laminar, finding the solution for this state is straightforward and LSA is widely popular for identifying and control of such patterns in various flow configurations [45, 46]. On the other side, turbulent flows experience broadband fluctuations in all quantities. Under certain circumstances where studying low-frequency events, for example due to separation, in turbulent flow is the main target, Linear Stability Analysis based on "time-averaged flow field" has been successful [47, 48].

In order to conduct such analysis for turbulent boundary layer flows, in the absence of separation, considering time-averaged flow quantities as the *equilibrium state* solution, $\bar{q}(\mathbf{x})$, should be justified by analyzing the timescale of different terms involved in the equation for the evolution of turbulent fluctuations. As explained by Lee et. al [49] and Jimenez [50], in the regions where the timescale of non-linear terms is much larger than that of the linear terms, the effect of non-linear components would be minimal, and therefore Linearized Navier-Stokes equations can represent the dynamics of

fluctuations. Timescale of the linear terms is $\mathcal{O}(1/S)$ where S shows the mean shear and timescale of the non-linear terms is $\mathcal{O}\left(l_\varepsilon/(\overline{u'_i u'_i})^{1/2}\right)$ where l_ε is suggested by Lee et. al [49] as the dissipation length-scale, or the length-scale of the energy-containing eddies of turbulence in equilibrium, $l_\varepsilon = (\overline{u'_i u'_i})^{3/2}/\varepsilon$ and $\varepsilon = \nu \overline{\partial u'_i/\partial x_j \partial u'_i/\partial x_j}$ is the dissipation rate of turbulent kinetic energy. The ratio of these two timescales is defined as the shear parameter $S^* = S\overline{u'_i u'_i}/\varepsilon$ which should be large enough to assume the linearization to hold. This condition is met near the wall (S^* remains around 10 up to $y/\delta \lesssim 0.6$), while by approaching the channel core where the shear becomes weaker, this assumption may not be valid [50]. It should also be noted that, in the present research, only the molecular viscosity has been included in \mathcal{L} operator of Equation (2.18). This assumption holds for modes with acoustic nature, but may weaken the conclusions for the viscous modes.

3. ACOUSTIC EXCITATION FOR HEAT TRANSFER ENHANCEMENT IN HIGH-SPEED FLOWS

In the present chapter, acoustic excitation applied parallel to the flow direction, in the streamwise direction, and its impact on heat and momentum transfer is investigated using numerical simulations. In order to maximize the effect of pulsations on the flow, we identify the specific conditions required for the external wave to acoustically *resonate* within the domain. This is achieved using the Linear Stability Analysis (LSA) of the background flow without the excitation. Such information is used to select the frequency and shape of the external acoustic field for making desirable changes in the flow. This resonant frequency is close to the *bursting frequency* suggested to modify the time-averaged Nusselt (\overline{Nu}) and skin friction ($\overline{C_f}$) upon pulsation. Moreover, the sensitivity of the flow response to the resonant frequency is assessed by applying external waves of identical amplitude and shape but at off-resonance frequencies. The present research is the first study to achieve the "acoustic streaming" in the compressible flows, and it opens new avenues towards enhancing the heat transfer without excessive skin friction losses.

3.1 Problem Formulation

The proposed test case comprises repeating identical sections of length L_x where each one includes a duct with an array of acoustic drivers mounted on the side walls. Figure 3.1 shows a schematic view of the setup. By exploiting the geometrical symmetry, we only simulate one unit and impose periodic boundary condition in the streamwise direction. To avoid complexities associated with the corners and the boundary layer formed on the side-walls, we focus on mid-span region and implement

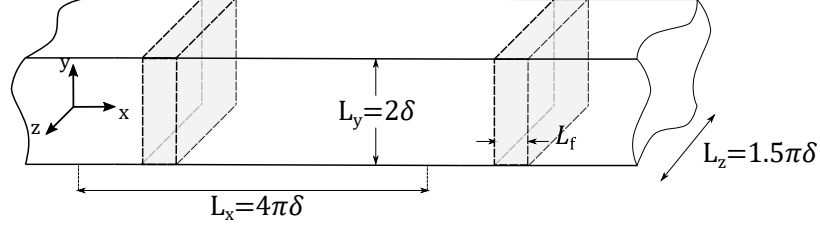


Figure 3.1. Schematic view of the proposed setup. The computational domain is of size $(L_x, L_y, L_z) = (4\pi\delta, 2\delta, 1.5\pi\delta)$. The shaded area of width L_f in each unit indicates the region where the effect of acoustic drivers mounted on side-walls is modeled via forcing function of form (3.1)

the periodic boundary condition in the spanwise direction. The effect of acoustic drivers is modeled with an external forcing following a bell-shape function:

$$\vec{f}_f(x, t) = A_f \exp\left(-\frac{(x - x_m)^2}{L_f^2}\right) \sin(\omega_f t) \vec{e}_x \quad (3.1)$$

where A_f is the forcing amplitude, L_f represents the thickness of the forcing region with midpoint x_m and ω_f sets the frequency of excitation. This force is added to the momentum equation as the source term, and the work performed by this source on the flow is considered in the energy equation following $\vec{f}_f \cdot \vec{u}$.

We first perform Direct Numerical Simulation of compressible channel flow without any external excitation. The time-averaged flow profiles are used as the base flow for the linear modal analysis. In search for the optimal excitation frequency, we solve the linearized Navier-Stokes equations and identify the modes that possess a large added heat-flux. In addition, the ideal mode should have a small decay rate, to modify the flow globally. We use this mode's frequency to operate the acoustic drivers and apply the forcing function (3.1) in the computational setup.

3.2 Results

In the section that follows, we first focus on the simulation of flow field without considering the effect of acoustic drivers. Time-averaged flow quantities serve as the base flow for the linearized Navier-Stokes analysis. Moreover, we compare these results with available datasets in the literature to assess the accuracy of our computational tool. Thereafter, we investigate the effect of acoustic excitation in the same flow configurations and analyze the modified boundary layer characteristics, including the skin friction and heat transfer enhancement.

3.2.1 Base Flow

As mentioned before, the computational setup consists of two parallel isothermal plates of size $L_x \times L_z = 4\pi\delta \times 1.5\pi\delta$ separated by a distance $L_y = 2\delta$. The forcing term on the right hand side of momentum and energy Equation (2.1), $f_i\delta_{1i}$, indicates a volume forcing in x-direction. At each time-step, bulk velocity U_b is locally computed following:

$$U_b(x, z) = \frac{\int_0^{L_y} \rho u \, dy}{\int_0^{L_y} \rho \, dy}$$

Then, spatially-averaged bulk velocity in the entire domain is calculated via,

$$U_{b,tot} = \frac{\int_0^{L_z} \int_0^{L_x} U_b(x, z) \, dx \, dz}{L_x L_z}$$

If $U_{b,tot}$ is different from the target value $U_{b,target}$, a forcing uniform term is added to the entire domain to retain the target value which corresponds to a constant mass flow-rate. This is a common practice when simulating turbulent channel flow which is followed by Coleman et. al [23] for compressible case, and Leveque et. al [51] in incompressible case. Such forcing strategy allows the “pressure gradient” to take

any non-uniform distribution within the domain (for example in the oscillatory case), given that the overall mass flow rate is constant.

For non-dimensionalization purposes, the reference temperature, velocity, and length scale are respectively wall temperature (T_w), speed of sound at wall temperature (c_w), and channel half width δ . Reynolds number based on bulk velocity U_b is $Re_b = \bar{\rho}U_b\delta/\mu_w = 3000$. To analyze the effect of flow compressibility on the results, two Mach numbers corresponding to subsonic ($M_b = U_b/c_w = 0.75$) and supersonic ($M_b = 1.5$) regimes are considered here. The later case is identical to the setup studied by Coleman et. al [23], therefore a comparison between the present simulation's results and data provided in [23] is shown here to demonstrate the accuracy of the present solver. The computational domain is discretized using $N_x \times N_y \times N_z = 144 \times 128 \times 96$ cells resulting in a resolution of $\Delta x^+ \sim 19$, $\Delta y^+_{min} = 0.24$, and $\Delta z^+ = 10.7$ where superscript $+$ indicates the quantities normalized with friction velocity, so that $y^+ = yu_\tau/\nu_w$. Time-averaged streamwise velocity and temperature as well as RMS of the fluctuating velocity components are presented in 3.2. Results show a promising agreement with Coleman et. al [23] both in terms of first and second order statistics. Similar number of grid points lead to $\Delta x^+ = 17.1$, $\Delta y^+_{min} = 0.21$, and $\Delta z^+ = 9.7$ for the subsonic case. Time-averaged streamwise velocity, density, and temperature profiles for the two aforementioned cases are illustrated in figure 3.3. One significant effect of compressibility can be seen in the temperature profiles, where the viscous heating increases the center-line temperature proportional to $T_c \propto M_b^2$. As such, in the present study, core region of the flow is approximately 8.7% and 37% hotter than the walls, in subsonic and supersonic cases, respectively. This is expected to provide a proper contrast when analyzing the effect of acoustic excitation on the heat transfer characteristics. It is also worth noting that the pressure is almost constant across the channel which, in turn, yields a mean density variation in wall-normal direction following the perfect gas law. These results serve as the equilibrium state, or base flow, for the linearized Navier-Stokes analysis.

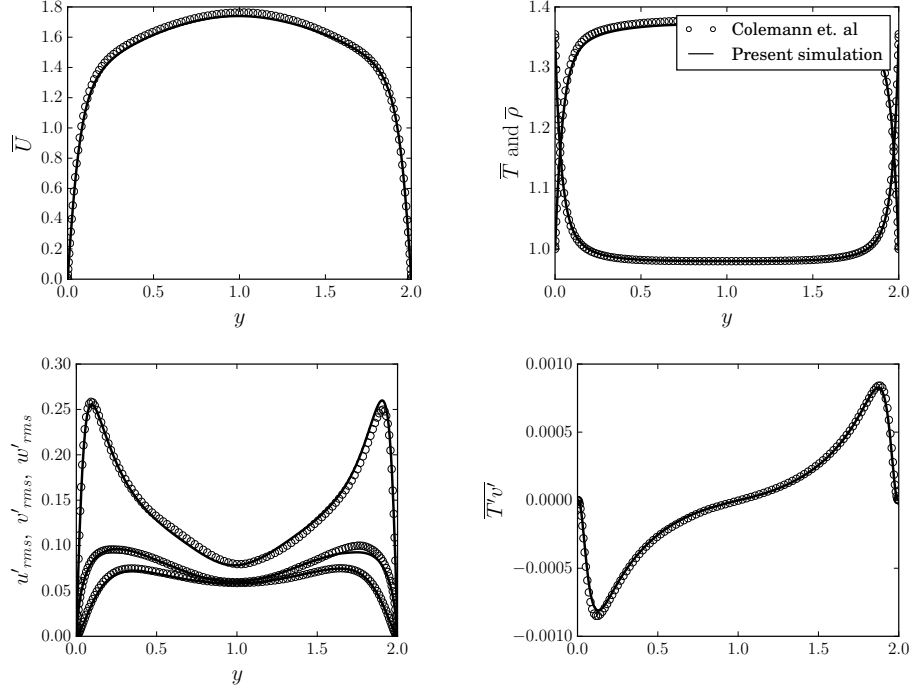


Figure 3.2. Mean streamwise velocity and temperature profiles as well as fluctuating velocity components at $Re_b = 3000$ and $M_b = 1.5$. Open circles (\circ) are taken from [23]

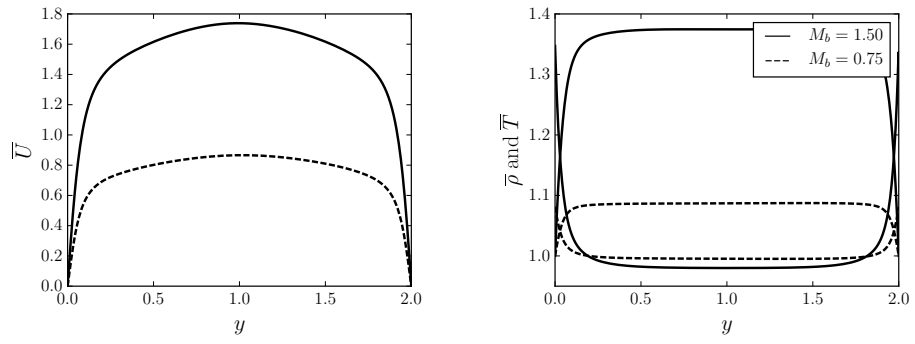


Figure 3.3. Time-averaged streamwise velocity, temperature and density at $Re_b = 3000$ and two different bulk Mach numbers, $M_b = 1.5$, and 0.75

3.2.2 Linearized Navier-Stokes Analysis

Linearized Navier-Stokes equations (2.21) and (2.23) are solved in order to investigate different families of modes present in this flow configuration and to identify the ones that are expected to create an effective increase in wall heat transfer throughout the channel. The streamwise wavenumber is considered $k = 0.5$ corresponding to the largest wave fitting in the domain of length $L_x = 4\pi$.

Eigenvalue spectrum in both subsonic and supersonic cases are shown in figure 3.4. This figure focuses on the most unstable modes in the spectrum. The Operators $\mathcal{R}\{.\}$ and $\mathcal{I}\{.\}$ return the real and imaginary parts of a variable. Horizontal axis represents the propagation speed of each mode and the vertical one shows the associated growth rate. The dashed-line specifies the threshold of neutrally stable modes so that modes closer to this line experience slower decay rate. All modes without external forcing are stable. Similar results are also reported by Friedrich & Bertolotti [52] using the Parabolized Stability Equations. These findings are consistent with that of Reynolds & Hussain [53] who observed that LSA of mean profiles corresponding to an incompressible turbulent channel flow remains stable up to $Re_\tau = \mathcal{O}(1000)$. As studied by [54] and Del Alamo & Jimenez [55], we can link the stable modes with the largest temporal growth rates to the near wall coherent structures. Here, we use the information provided by the LSA to decide which mode should be excited to create changes in the flow consistent with our goals.

In the present configuration, four major families of modes are observed; "Bulk modes" form a hook shape and travel downstream with the bulk velocity of the flow. "Fast acoustic" modes (e.g. R_1) are positioned on the right and the "slow" ones (e.g. L_1) are found on the left side of bulk modes. The other two isolated modes shown in this figure represent the wall modes $W_{1,2}$.

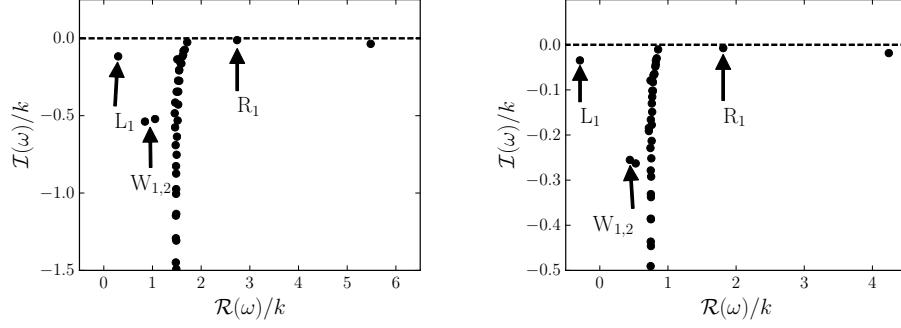


Figure 3.4. Eigenvalue spectrum of compressible channel flow at $Re_b = 3000$ and $M_b = 1.5$ (left) and $M_b = 0.75$ (right). Streamwise wavenumber is $k = 0.5$ corresponding to the largest mode that fits inside a domain of size $L_x = 4\pi$. R_1 and all other modes located on the right side of the hook-shape modes are fast acoustic modes, L_1 and other modes appearing on its left side are slow acoustic modes and W_i ($i = 1$ on the left and $i = 2$ is on the right) are wall modes

To further analyze these modes' properties, two parameters are defined based on their corresponding eigenfunctions:

$$\begin{aligned} \widehat{uv} &= \frac{2}{\mathcal{T}} \int_0^{\mathcal{T}} \mathcal{R}\{u'\} \mathcal{R}\{v'\} dt = \mathcal{R}\{\widehat{u}\widehat{v}^*\} \text{ mode shear stress} \\ \widehat{Tv} &= \frac{2}{\mathcal{T}} \int_0^{\mathcal{T}} \mathcal{R}\{T'\} \mathcal{R}\{v'\} dt = \mathcal{R}\{\widehat{T}\widehat{v}^*\} \text{ mode heat flux} \end{aligned} \quad (3.2)$$

where \mathcal{T} represents the period, \widehat{u} , \widehat{v} and \widehat{T} are streamwise velocity, wall-normal velocity and temperature eigenfunctions and superscript $*$ denotes complex conjugate. Figure 3.5 illustrates these quantities for three modes R_1 , W_1 and L_1 at two different Mach numbers. Modes belonging to the same family, exhibit similar behavior, however, near-wall changes are more pronounced in the supersonic case due to larger mean flow gradients in this region.

Wall modes W_i , have a large decay rate and, in case of excitation, can only affect the near-source region. Moreover, their corresponding added shear-stress is significantly higher than the added heat flux, and therefore they cannot be the ideal

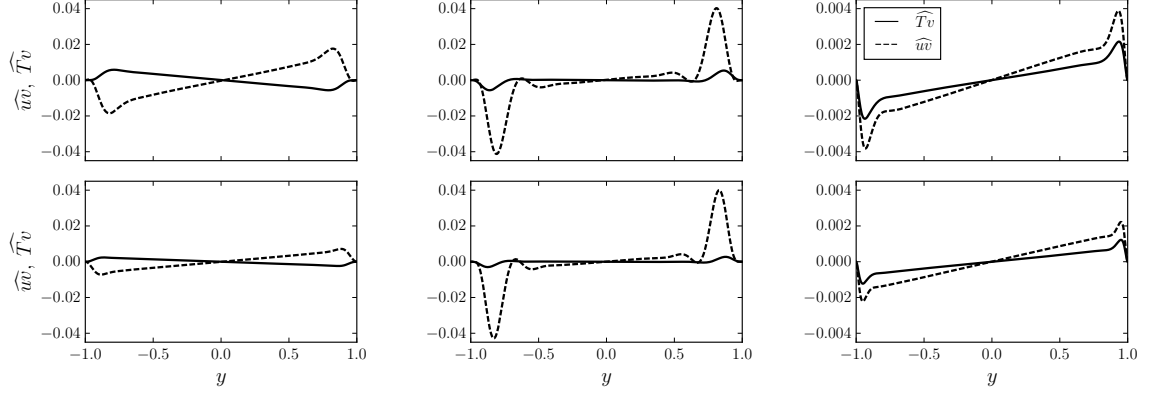


Figure 3.5. The added shear stress \widehat{uv} and added heat flux \widehat{Tv} for mode R_1 (right), W_1 (middle), and L_1 (left). Top row corresponds to the supersonic $M_b = 1.5$ and the bottom row is associated with the subsonic case $M_b = 0.75$

mode for making a effective heat transfer enhancement. Applying an external forcing activated only near the wall or modifying the wall boundary condition, for instance by employing a darcy-type porous media [21, 56] or acoustic liners [22], often results in excitation of this mode.

Slow acoustic (or left running) modes L_1 experience faster decay rate than R_1 modes, limiting their ability to make a global change in the flow. This mode's heat flux is still less than the shear stress while showing a 180° phase difference in this case. Targeting the L_1 modes can be challenging as well, since they travel upstream in the subsonic case.

Mode R_1 , on the other hand, has the largest imaginary part which translates into the lowest decay rate and therefore, if excited, can make a lasting change in the flow. Moreover, the heat flux corresponding to this mode is comparable with the its shear stress near the boundaries. Therefore, R_1 mode is chosen as the "resonant mode" for acoustic excitation.

Estimation of mode R_1 's velocity in the present test case may not be straightforward since the temperature raises up to 37% (at $M_b = 1.5$) and 8.6% (at $M_b = 0.75$)

from wall to the center-line, and therefore, speed of sound changes considerably across the channel. In the supersonic case, $\bar{U}_{\text{center-line}} + \bar{c}_{\text{center-line}} = 2.91$ while the LSA gives $c_{R_1} = 2.73$ and in the subsonic case, $\bar{U}_{\text{center-line}} + \bar{c}_{\text{center-line}} = 1.91$, however, the LSA shows $c_{R_1} = 1.81$.

The optimal wall-normal distribution of forcing term (A_f in Equation (3.1)) can be determined following the method of Lagrangian multiplier developed by Browne et. al [57] in discrete framework. However, in the present study, A_f is assumed uniform along channel height for simplicity and ease of future experimental implementation.

3.2.3 Fully Non-linear Navier-Stokes Simulations

After selecting the excitation frequency, fully non-linear Navier Stokes equations (2.1) are solved considering the forcing function of form (3.1). Given the reference parameters described in section 3.2.1, amplitude of forcing is non-dimensionalized with respect to $\bar{\rho}c_w^2/\delta$. According to the Equation (2.1), the periodic forcing acts as a pulsating pressure gradient with a Gaussian distribution function applied only in the forcing region, in which the max to min amplitude equals to twice A_f . In addition to the pulsation at the resonant frequency at each Mach number, C1 and C2 respectively referring to the supersonic and subsonic conditions described before, two more cases, labeled as C3 and C4, are also investigated to analyze the effect of off-design excitation on the flow. We study three cases, namely A1 to A3, identical to C2 but at different forcing amplitudes to reveal the relationship between the A_f and perturbations as well as their effect on the time-averaged flow quantities. D1 and D2 simulations show the impact of resonance at lower frequencies by considering larger domain lengths, i.e. $L_x = 6\pi$ and 8π (corresponding to $k = 2/3$ and $k = 1/4$). Extension of the results of case C2 to higher Reynolds number, namely at $Re_b = 6000$, is presented in case I1.

Simulation parameters for all the aforementioned cases are summarized in table 3.1. Non-dimensional Stokes layer thickness in all cases is very close to the buffer

Table 3.1.

Simulation parameters for the acoustically excited cases. Length of the forcing region in all cases is set to $L_f = 0.0745L_x$

Case	M_b	Re_b	Re_τ	A_f	ω_f	L_x	$N_x \times N_y \times N_z$	$\delta_s^+ = \delta_s u_\tau / \nu_w$
C1	1.50	3000	215	0.50	$2\pi/4.59$	4π	$144 \times 128 \times 96$	4.30
C2	0.75	3000	197	0.25	$2\pi/6.94$	4π	$144 \times 128 \times 96$	4.23
C3	1.50	3000	215	0.50	$2\pi/4.00$	4π	$144 \times 128 \times 96$	4.01
C4	1.50	3000	215	0.50	$2\pi/5.00$	4π	$144 \times 128 \times 96$	4.49
I1	0.75	6000	363	0.25	$2\pi/6.954$	4π	$288 \times 256 \times 192$	6.04
A1	0.75	3000	197	0.125	$2\pi/6.94$	4π	$144 \times 128 \times 96$	4.23
A2	0.75	3000	197	0.0625	$2\pi/6.94$	4π	$144 \times 128 \times 96$	4.23
A3	0.75	3000	197	0.03125	$2\pi/6.94$	4π	$144 \times 128 \times 96$	4.23
D1	0.75	3000	197	0.25	$2\pi/10.41$	6π	$216 \times 128 \times 96$	6.34
D2	0.75	3000	197	0.25	$2\pi/13.89$	8π	$288 \times 128 \times 96$	8.46

layer threshold of $y^+ \approx 5$. This is the lowest "resonant" frequency that fits in the studied computational domain. In C1 to C4 and A1 to A3, a computational domain identical to the unexcited case 3.2.1 is adopted. To assess the sensitivity of findings to the computational grid, case C1 and C2 are repeated with grid size $N_x \times N_y \times N_z = 216 \times 192 \times 144$ (1.5 times grid points in each direction compared to the initial setup) and little to no variation is observed in temporal statistics. Similarly, the effect of domain size on the results is studied by simulating a channel of length $2L_x$ with two identical acoustic drivers separated by distance L_x . This case also reproduced temporal statistics that closely follow those of C1 case, therefore indicating that the box size is sufficiently long in this analysis.

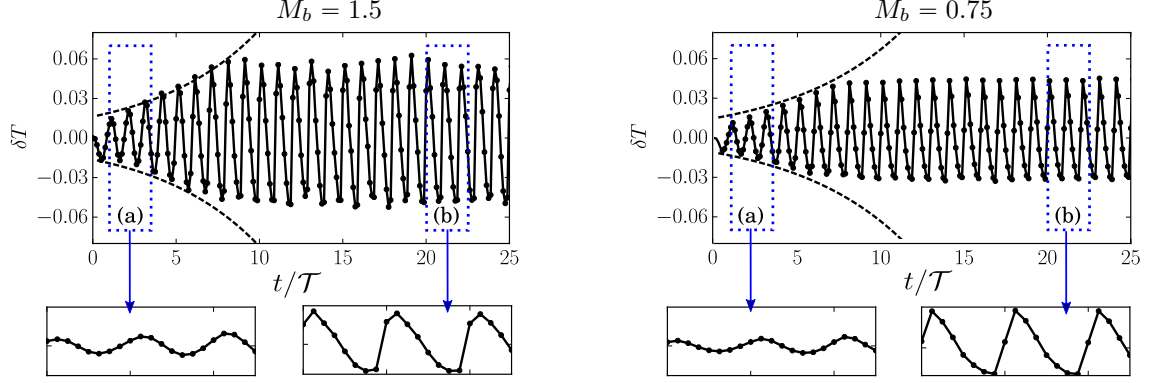


Figure 3.6. History of temperature perturbation $\delta T = T_{\text{exc}} - T_{\text{unexc}}$ at the center of the forcing region at $Re_b = 3000$ and two Mach numbers, C1: $M_b = 1.5$ (left) and C2: $M_b = 0.75$ (right)

Temporal Evolution of the Perturbations

In order to analyze the system response to the external fluctuations, we need to clearly differentiate the externally-induced perturbations from the background turbulent field. To aim this, we perform two separate sets of simulations for each case, one with the forcing (referred to as the "excited" case) and the other without any external fluctuations ("unexcited" case). Both cases are initialized with identical flow fields and all other simulation parameters including the grid and time-step size are kept unchanged. The perturbation field (δq) reads,

$$\delta q(\mathbf{x}, t) = q_{\text{exc}}(\mathbf{x}, t) - q_{\text{unexc}}(\mathbf{x}, t) \quad (3.3)$$

where q_{exc} represents a generic flow quantity in the excited configuration and q_{unexc} corresponds to the unexcited case. Figure 3.6 shows the temporal evolution of the temperature perturbations at the channel center spatially averaged within the forcing region. In the supersonic case, C1, (figure 3.6-left), external forcing is translated into temperature perturbations of amplitude 2% of T_w in the first cycle. Thereafter, this amplitude grows in three different stages. Initially, we observe an exponential growth.

Dashed-lines show this trend and the detailed view of region (a) suggests the pure sinusoidal form of the perturbations representing a *linear (modal) process*. In the second stage, the growth rate decreases followed by a steepening in the acceleration phase of the forcing period which indicates a *weakly non-linear process*. Distortions in the pure sinusoidal form of the perturbations manifest higher frequency waves appeared as a result of non-linear interactions. Finally, after 10 cycles, the perturbation amplitude remains nearly constant which marks the *limit-cycle region*. In this section, immediately after starting each period, temperature perturbation rises significantly and dissipates gradually. This implies the broad-band response of the system to a single-frequency force which, in turn, demonstrates the highly non-linear nature of this region (see region (b)). Similar behavior is observed in subsonic configuration, C2, (figure 3.6-right). Although the amplitude of δT in this case is always smaller than that of the supersonic configuration, the limit cycle is achieved in fewer periods, suggesting that the non-linear process is started earlier. suggesting a larger *relative* forcing amplitude than the supersonic case.

The next step is to analyze the effect of acoustic excitation on the heat and momentum transfer near the wall. Two parameters, Shear Enhancement Factor (SEF) and Thermal Enhancement Factor (TEF) are defined based on the space-averaged skin friction coefficient (C_f) and Nusselt number (Nu) to quantitatively study this process.

$$\text{SEF} = \frac{C_{f,\text{exc}}}{C_{f,\text{unexc}}} \quad \text{and} \quad \text{TEF} = \frac{Nu_{\text{exc}}}{Nu_{\text{unexc}}} \quad (3.4)$$

where,

$$Cf = \frac{\mu_w \frac{\partial U}{\partial y}|_w}{0.5 \rho U_b^2} \quad \text{and} \quad Nu = \frac{\frac{\partial}{\partial y} (T - T_w)|_w}{(T_b - T_w)/\delta}$$

Considering the modified Reynolds Analogy (Chilton-Colburn equation),

$$C_f = \frac{Nu}{Re_b Pr^{1/3}}$$

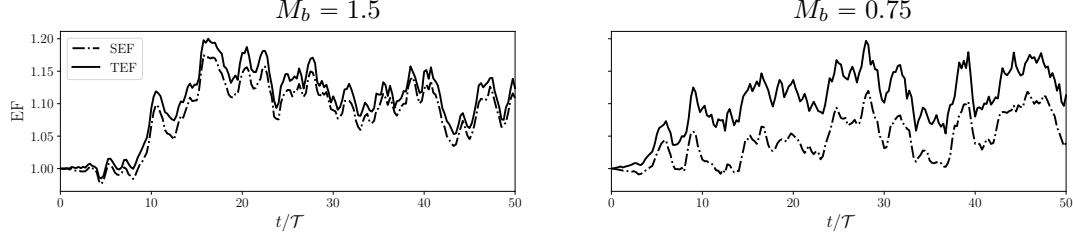


Figure 3.7. History of the space-averaged SEF and TEF at $Re_b = 3000$ and two Mach numbers, C1: $M_b = 1.5$ (left) and C2: $M_b = 0.75$ (right)

one may find the Nusselt number as a linear function of the skin friction (or vice versa). In the unexcited condition, this relationship holds at $Re_b = 3000$ and $M_b = 1.5$ with less than 1% of error, and at a similar Reynolds number and $M_b = 0.75$, with less than 3% error. If we assume this analogy to be valid in the excited flow configuration, as well:

$$C_{f,\text{exc}} = \frac{Nu_{\text{exc}}}{Re_b Pr^{1/3}}$$

Hence, $C_{f,\text{exc}}/C_{f,\text{unexc}} = Nu_{\text{exc}}/Nu_{\text{unexc}}$. Given the definitions of Shear and Thermal Enhancement Factors (3.4), this implies $SEF = TEF$. Therefore, we expect SEF and TEF closely follow each-other and comparing these two quantities is appropriate. In regions where an offset is observed between these two quantities, one may conclude that the Reynolds Analogy (or any simple linear relationship between C_f and Nu) does not hold.

At different Mach numbers, we have different heat loads $(T_b - T_w) \propto M_b^2$. Essentially, such load at $M_b = 0.75$ is four times smaller than that of $M_b = 1.5$. Since the amplitude of the excitation δT in both cases are similar, we expect the heat transfer process at smaller M_b to experience stronger alteration due to the excitation. Figure 3.7 presents the history of SEF and TEF over 50 periods for both C1 and C2 cases. These two quantities share similar trends; they both start from the unity (by definition), grow rapidly in time and finally oscillate around some mean values. Acoustic

excitation leads to higher thermal enhancement compared to the skin friction augmentation. The difference between SEF and TEF is significantly more pronounced in the subsonic configuration (C2), although having smaller δT amplitude.

Averaging these quantities over 100 excitation periods shows $\overline{\text{TEF}} = 1.101$ and $\overline{\text{SEF}} = 1.084$ for the supersonic (C1) and $\overline{\text{TEF}} = 1.109$ and $\overline{\text{SEF}} = 1.053$ for the subsonic case (C2). Therefore, heat transfer enhancement due to the excitation is 20% higher than the skin friction augmentation in C1, while in C2 configuration, acoustic excitation enhanced the heat transfer almost twice as much as the skin friction.

Adiabatic wall temperature T_{aw} is defined as “the temperature that a wall would acquire in case it was thermally insulated”. Here, we estimate this quantity via $T_{aw} = T_c \left(1 + Pr^{1/3} \frac{\gamma-1}{2} M_c^2\right)$ where T_c and M_c are static temperature and local Mach number at the channel center [58]. This quantity for the supersonic case is approximately $T_{aw} = 1.91$, and for the subsonic case is ≈ 1.22 while the wall temperature in both cases is constant at $T_w = 1$. Upon finding T_{aw} , one may calculate the heat transfer coefficient as $h = q'' / (T_{aw} - T_w)$. According to Maffulli & He [59], q'' is not a linear function of $T_{aw} - T_w$, instead, the slope $\partial q'' / \partial (T_{aw} - T_w)$ decreases as $(T_{aw} - T_w)$ becomes smaller. Therefore, in response to a constant change in wall temperature (δT_w), one may observe larger change of heat flux in the supersonic case. On the other hand, in case of a constant change in heat flux ($\delta q''$), for example due to the excitation, variation of the slope, i.e. h , may be more pronounced in the subsonic condition. Hence, we expect that acoustic pulsation with similar amplitude would be more effective in modifying the TEF of the subsonic case compared to the supersonic counterpart.

Near-wall Turbulent Structures

To investigate the effect of acoustic excitation on the heat transfer process near the solid boundary, instantaneous temperature perturbation fields are analyzed here.

Since subsonic and supersonic cases show similar behavior, discussion in this section is limited to the supersonic setup. Figure 3.8 focuses on the response of the system in the early stages of the excitation, i.e. region (a) in figure 3.6 (left), and illustrates the instantaneous temperature perturbations near the bottom wall (on the xz -plane at $y^+ \approx 4$) at four different instances of one excitation period. In overall, this figure shows the passage of an acoustic wave with an amplitude of almost 4% of the wall temperature. Weakly nonlinear interaction of the acoustic wave and near-wall streamwise streaks is noticeable in form of fluctuations superimposed on the spatial sinusoidal pattern and excessively hot or cold spots throughout the domain. Figure 3.9 shows

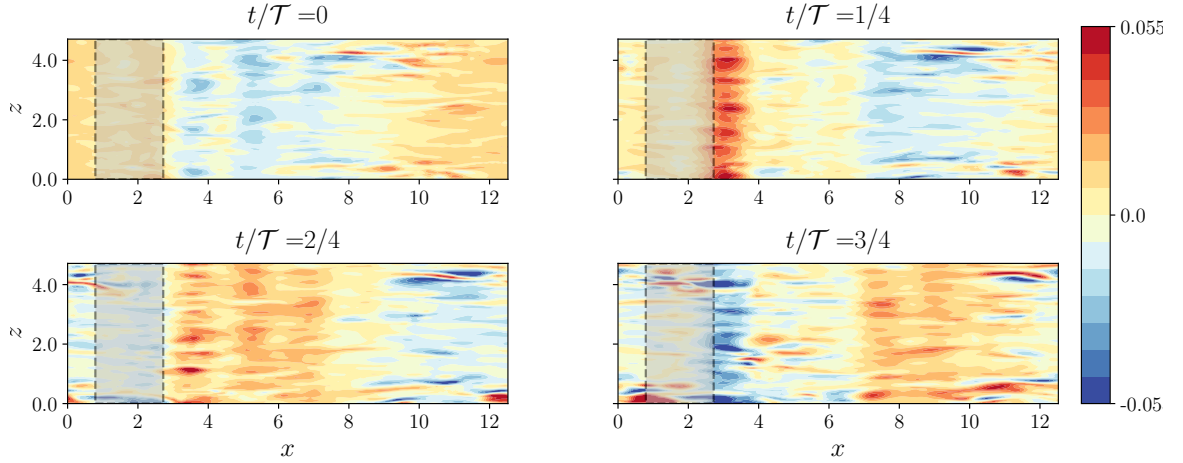


Figure 3.8. Instantaneous temperature perturbation field for acoustic excitation of supersonic turbulent boundary layer. A top view at the bottom wall at $y^+ \approx 4$ for four instances of one period within region (a) in figure 3.6 (left). The grey box indicates the region where forcing is active.

the passage of an acoustic wave in the limit cycle region. The wave front creates a strong spanwise structure travelling downstream with the speed $c_x = 4\pi/T_f = 2.74$ (non-dimensionalized by c_w) followed by a wake of weaker rollers. In this case, the amplitude of perturbations increases up to $22\%T_w$ with several locations experiencing unusually high and low temperatures. Classic near-wall turbulent structures are more

evident in this figure by streamwise low speed streaks disrupting the wave front and significantly modulating the region behind it.

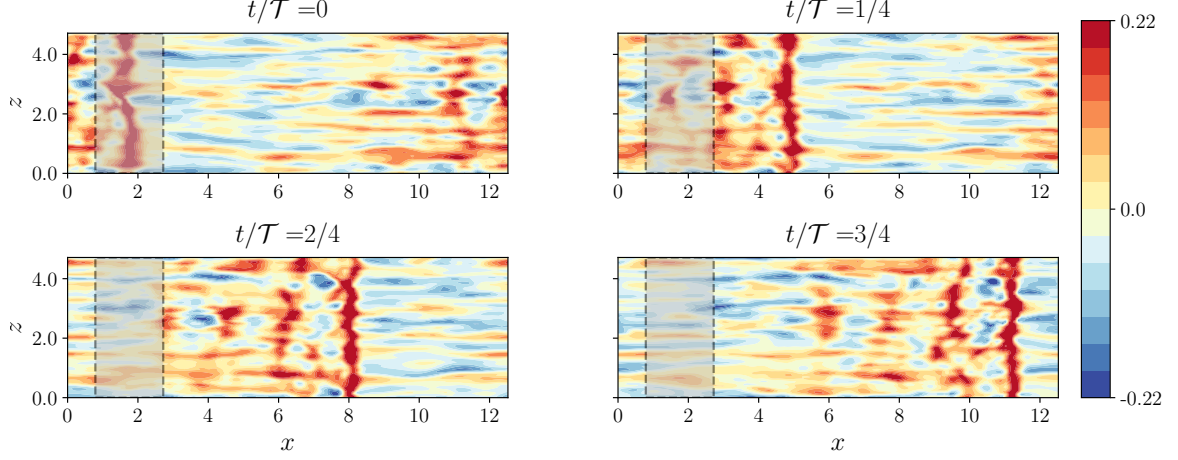


Figure 3.9. Instantaneous temperature perturbation field for acoustic excitation of supersonic turbulent boundary layer. A top view at the bottom wall at $y^+ \approx 4$ for four instances of one period within region (b) in figure 3.6 (left). The grey box indicates the region where forcing is active.

Vortical structures near the bottom wall, confined within the planes $y = 0$ and $y = 0.1$ are plotted via iso-value contours of Q-criterion for the case C1 in figure 3.10. Each row represents the instantaneous field at a given instance of a period in the limit-cycle region. The left column illustrates the near-wall structures of the unexcited case where the long streamwise vortices can be easily observed. However, in the excited case, the wave front creates the spanwise-uniform structures that roll in the $+z$ -direction and are convected downstream. In the wake of this wave front, the spanwise structures are weakened and finally break up. The snapshot in the last instance $t/\mathcal{T} = 3/4$, clearly shows that the impact of the wave front is completely vanished in the second half of the channel.

Figure 3.11 displays the time-space temperature field averaged in spanwise direction, once the perturbations are saturated, region (b) in Figure 3.6 (left). This representation allows to identify the different speed at which perturbations evolve.

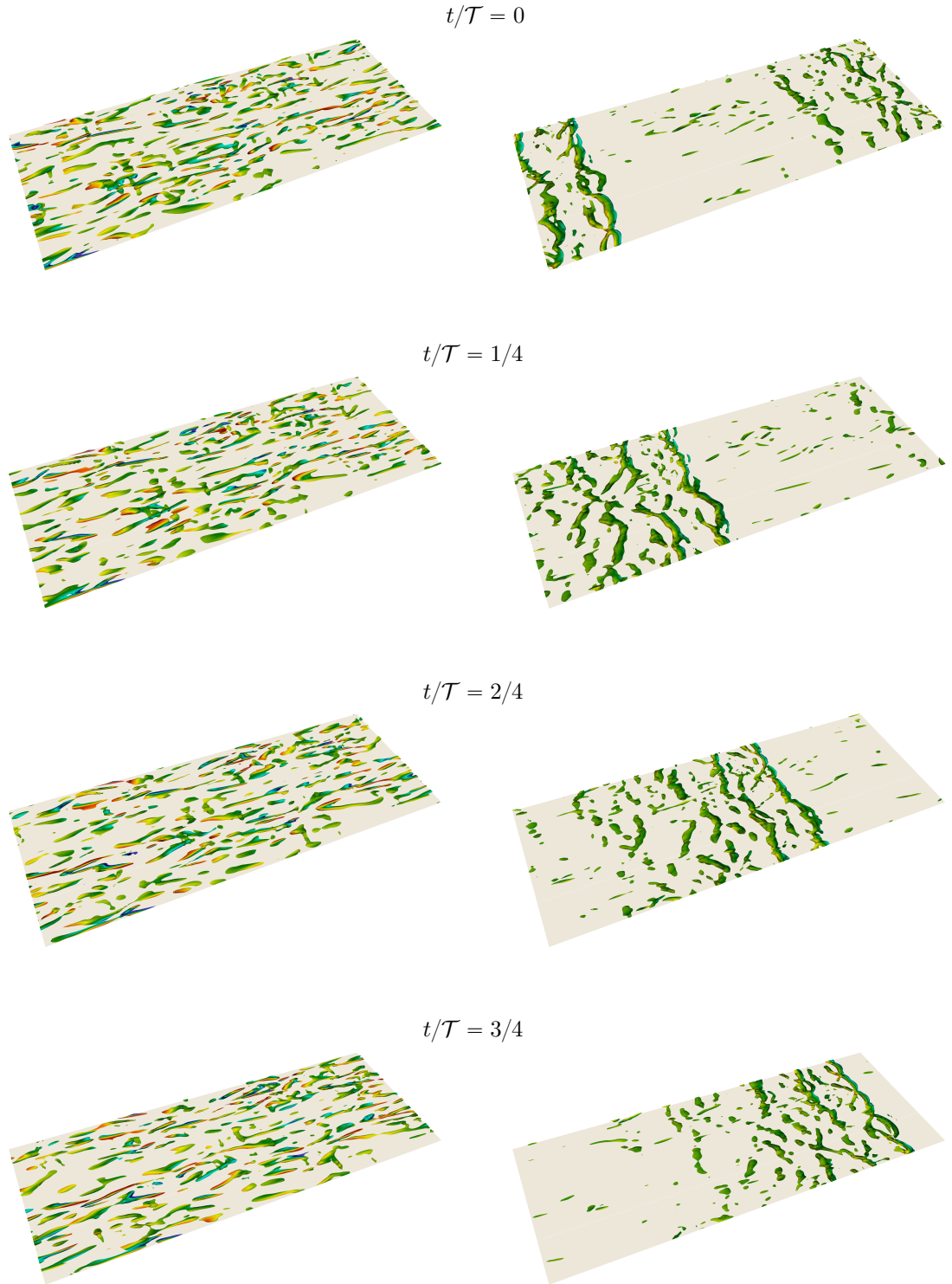


Figure 3.10. Instantaneous Q-criterion confined between the bottom wall and $y = 0.1$ in the unexcited (left) and the excited condition of C1 (right) for a supersonic turbulent channel flow at four instances of one period (\mathcal{T}). The structures are colored by their corresponding wall-normal velocity component from blue (negative) to red (positive values).

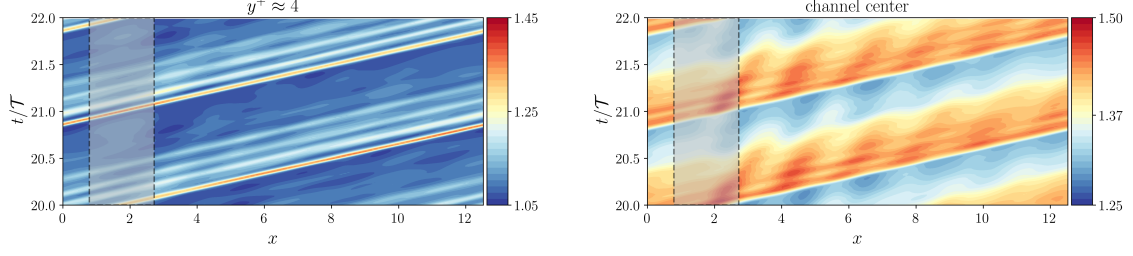


Figure 3.11. time- x representation of the spanwise-averaged temperature field near the bottom wall at $y^+ \approx 4$ (left) and at the channel center (right), over one pulsation cycle in the limit-cycle region.

Near the bottom wall at $y^+ \approx 4$ (left), the wave front is clearly visible along with the rollers that appear in the wake region retaining a constant speed across the domain. At the channel center (right figure), after the passage of the wave front, one can observe relatively strong waves that propagate downstream at very slow rates (high slopes in tx -plane), and therefore over one pulsation period \mathcal{T} , are confined within a narrow region in x . This suggests formation of structures with time-scale $\ll \mathcal{T}$ and length-scale $\ll L_x$ which can drive the streaming.

Streaming velocity and Temperature, defined as $U_{st} = \bar{U}_{exc} - \bar{U}_{ubnexc}$ and $T_{st} = \bar{T}_{exc} - \bar{T}_{ubnexc}$ for case C1 are illustrated in figure 3.12. Time-averaging is performed within $t/\mathcal{T} \in [10, 90]$ to only include the limit-cycle oscillations. As a result of non-linear interaction of perturbations with the background flow, and themselves, a periodic pattern with $k = 4$ has appeared in both T_{st} and U_{st} . In both plots, streaming quantities regions with positive streaming values appear to take larger magnitudes and stay closer to the wall, therefore, qualitatively, one may infer that Shear and Thermal Enhancement Factors (spatially averaged along the channel length) should be greater than unity. Larger TEF compared to SEF for this flow condition may also be attributed to the location of positive T_{st} which resides in a shorter distance from the wall.

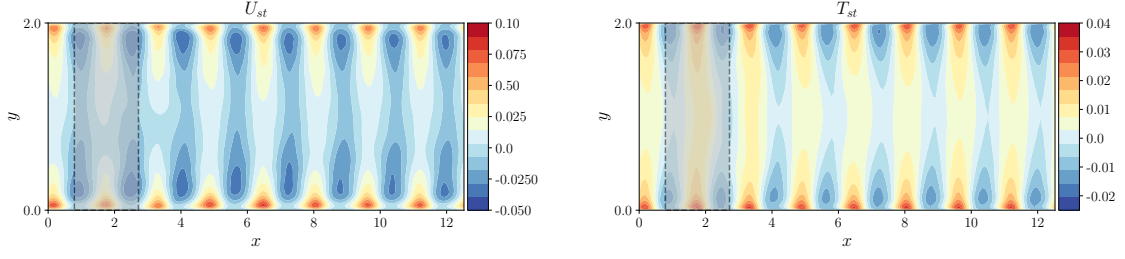


Figure 3.12. Contours of streaming velocity U_{st} (left) and temperature T_{st} for an acoustically excited supersonic channel flow at $Re_b = 3000$ and $M_b = 1.5$ with $A_f = 0.5$ and $\omega_f = 2\pi/4.59$ over $t/\mathcal{T} \in [10, 90]$

Data Reduction

Any instantaneous quantity can be decomposed into a "steady" and an "unsteady" component. The latter can be further decomposed into "harmonic" component and "random fluctuation" term:

$$\phi(\mathbf{x}, t) = \underbrace{\overline{\phi(\mathbf{x})}}_{\text{steady term}} + \underbrace{\widetilde{\phi(\mathbf{x}, t)}}_{\text{harmonic term}} + \underbrace{\phi'(\mathbf{x}, t)}_{\text{random fluctuation}} \quad (3.5)$$

where the harmonic term is found following the phase-locked averaging of the instantaneous quantity:

$$\langle \phi(\mathbf{x}, t) \rangle = \frac{1}{N+1} \sum_{n=0}^N \phi(\mathbf{x}, t + n\mathcal{T}) \quad (3.6)$$

and

$$\widetilde{\phi(\mathbf{x}, t)} = \langle \phi(\mathbf{x}, t) \rangle - \overline{\phi(\mathbf{x})}$$

where $\mathcal{T} = 2\pi/\omega_f$ and ω_f is the excitation frequency. Harmonic component of the streamwise velocity field, at four different instances of one period, are presented in figures 3.13 and 3.14 (top), for both supersonic and subsonic cases respectively. The bottom row of these two figures represents the harmonic temperature fields at the same instances. In supersonic case, the amplitude of harmonic component of stream-

wise velocity has reached to more than 17% of the bulk velocity of the flow and the amplitude of harmonic temperature component has raised to 15% of wall temperature. These amplitudes in subsonic flows are respectively 29% and 11%.

Formation of new near-wall spanwise structures travelling downstream is evident in both regimes. These rollers start with a circular shape right at the wave front and then, as a result of non-linear interaction with the classic near-wall streaks, become more inclined in the flow direction. Similar behaviour is observed in subsonic regime as well. However, in this regime, the effects seem more confined to the wall.

As suggested by the linear analysis in figure 3.5 (right), A significant portion of momentum and heat transfer is concentrated in the near-wall region of the harmonic term at this frequency. Moreover, the effect of excitation at this frequency on the heat transfer is more confined to the walls.

Following on the decomposition introduced in (3.5), second order statistics, such as Reynolds stresses, can also be decomposed into a background and harmonic parts [60]:

$$\langle \phi'_i \phi'_j \rangle = \overline{\phi'_i \phi'_j} + \widetilde{\phi'_i \phi'_j} \quad (3.7)$$

where the term on the left hand side is calculated via $\langle \phi'_i \phi'_j \rangle = \langle \phi_i \phi_j \rangle - \langle \phi_i \rangle \langle \phi_j \rangle$. The background stress is represented by $\overline{\phi'_i \phi'_j}$ and changes in the background by passing the harmonic structures at each instance are indicated by $\widetilde{\phi'_i \phi'_j}$.

Second-order time-averaged statistics can also be written as:

$$\overline{\phi'_i \phi'_j}|_{tot} = \overline{(\phi_i - \overline{\phi_i})(\phi_j - \overline{\phi_j})} = \overline{(\widetilde{\phi_i} + \phi'_i)(\widetilde{\phi_j} + \phi'_j)} = \overline{\widetilde{\phi_i} \widetilde{\phi_j}} + \overline{\phi'_i \phi'_j} \quad (3.8)$$

Following these equations, total values of the stress tensor (for brevity only $\overline{u'u'}|_{tot}$, $\overline{v'v'}|_{tot}$, and $\overline{u'v'}|_{tot}$) as well as turbulent heat flux ($\overline{T'v'}|_{tot}$) are decomposed to the background term and harmonic motion contribution. Results are plotted in figures 3.15 and 3.16 along with the profiles corresponding to the unexcited case. Contribution of the harmonic motion is shown by the blue lines, and in some cases, can be better visualized as the difference between total (green) and the background term (red).

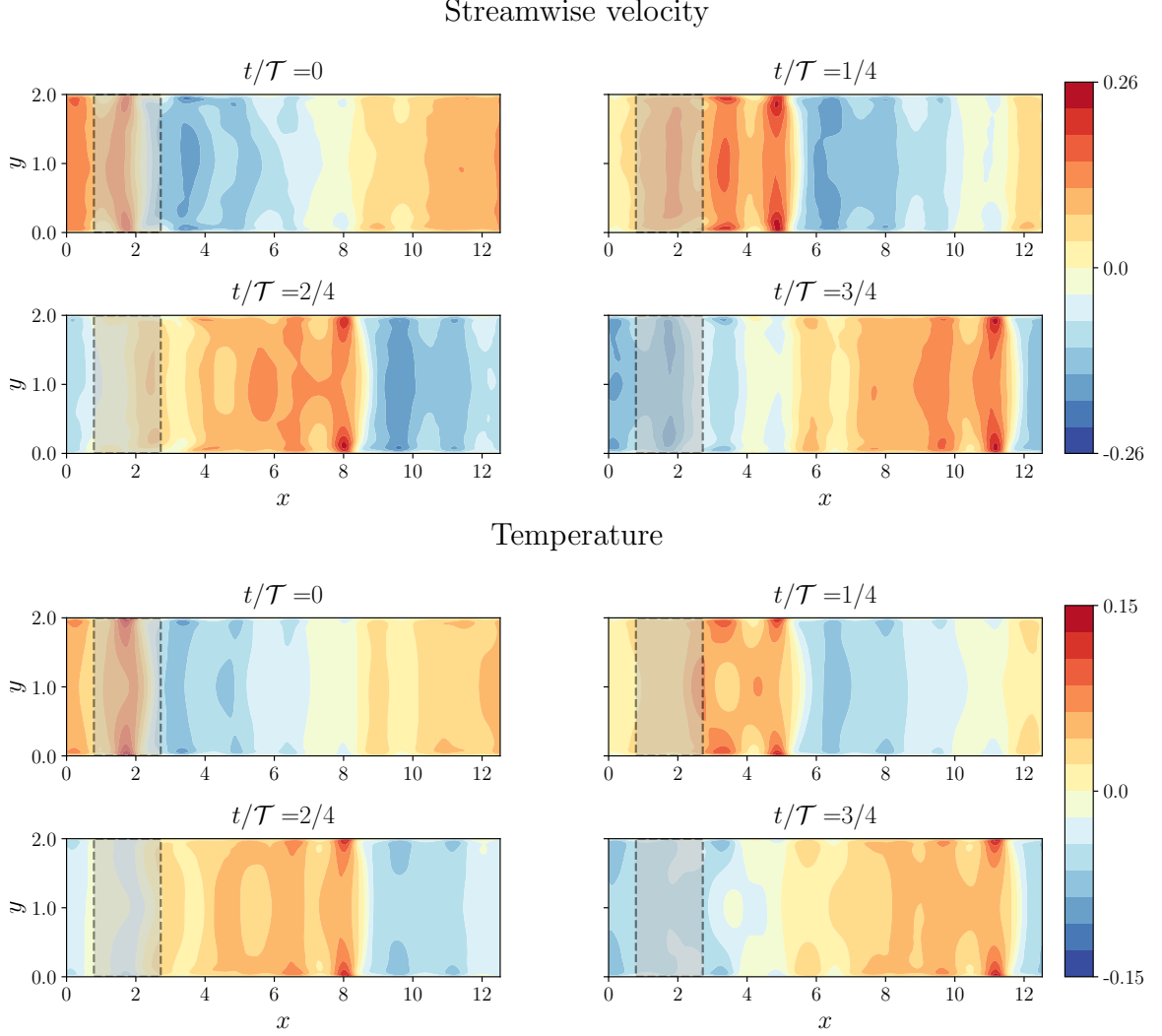


Figure 3.13. Harmonic component of streamwise velocity (top) and temperature field (bottom) in supersonic configuration

Deviation of the background term from the profiles corresponding to the unexcited case (dashed-line), indicates the presence of a non-linear process that spreads the energy from the eddies at the harmonic frequency (and corresponding sub-harmonics) to other uncorrelated frequencies. Considering the top-left figure ($\overline{u'u'}$), passage of the harmonic structures promotes the total streamwise velocity fluctuations in both bulk and near wall regions. This suggest that the oscillatory pressure waves can en-

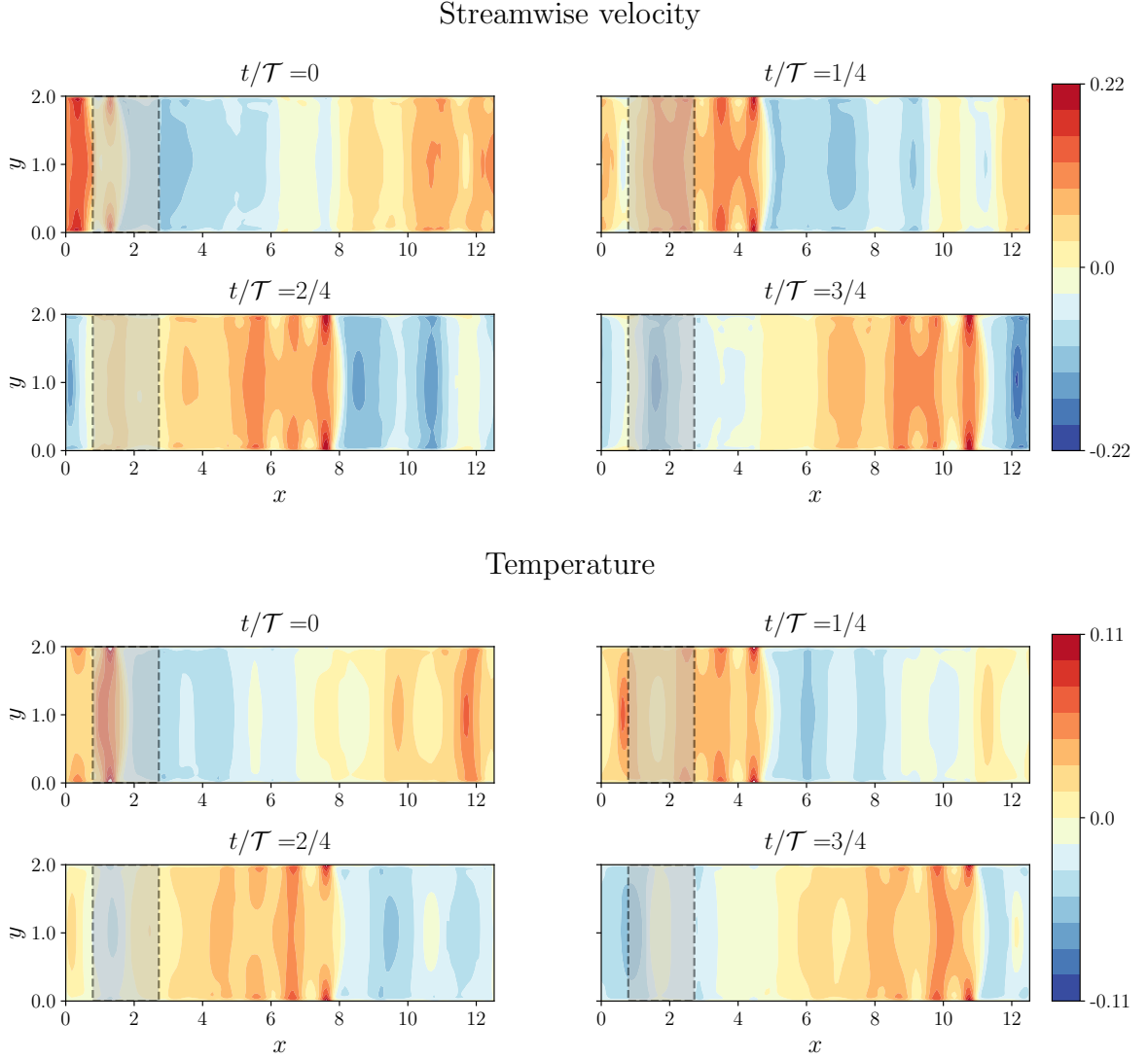


Figure 3.14. Harmonic component of streamwise velocity (top) and temperature field (bottom) in subsonic configuration

hance the intensity of predominantly random fluctuations present away from the walls. In the wall-normal direction, the excitation modifies the total turbulence intensity mainly through non-linear interactions and at frequencies other than the excitation frequency (and corresponding sub-harmonics).

Applying the acoustic excitation seem to have a limited effect on the skin friction. The background term is slightly increased near the wall and contribution of the

harmonic term in the total skin friction is negligible. On the contrary, the excitation leads to the considerable promotion of the background turbulent heat flux compared to the unexcited case through non-linear interactions and, separately, the harmonic motions (at the excitation frequency) show a positive effect on total turbulent heat flux.

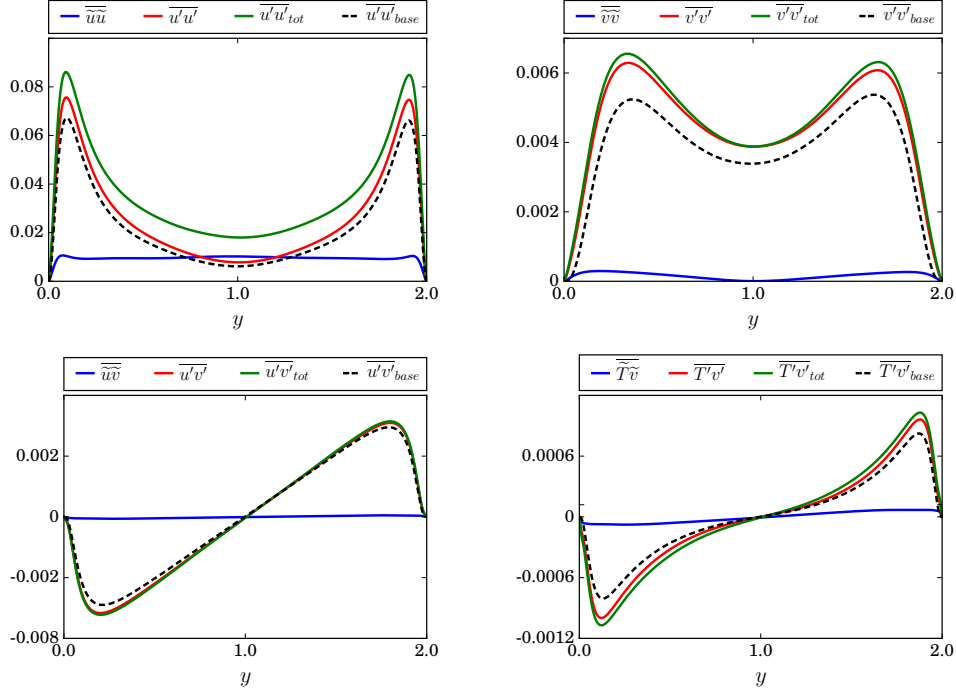


Figure 3.15. Decomposition of total Reynolds stress terms as well as turbulent heat flux into the background and harmonic terms for supersonic configuration

In the subsonic configuration, the effect of acoustic excitation is more clear. Turbulence intensity in streamwise and wall normal directions are promoted similar to the supersonic case. Turbulent heat flux, and especially the relative contribution of the harmonic motion, shows a significantly intensified response to the superposition of the acoustic waves compared to the other configuration. In the other hand, relative modifications on the skin friction stays the same.

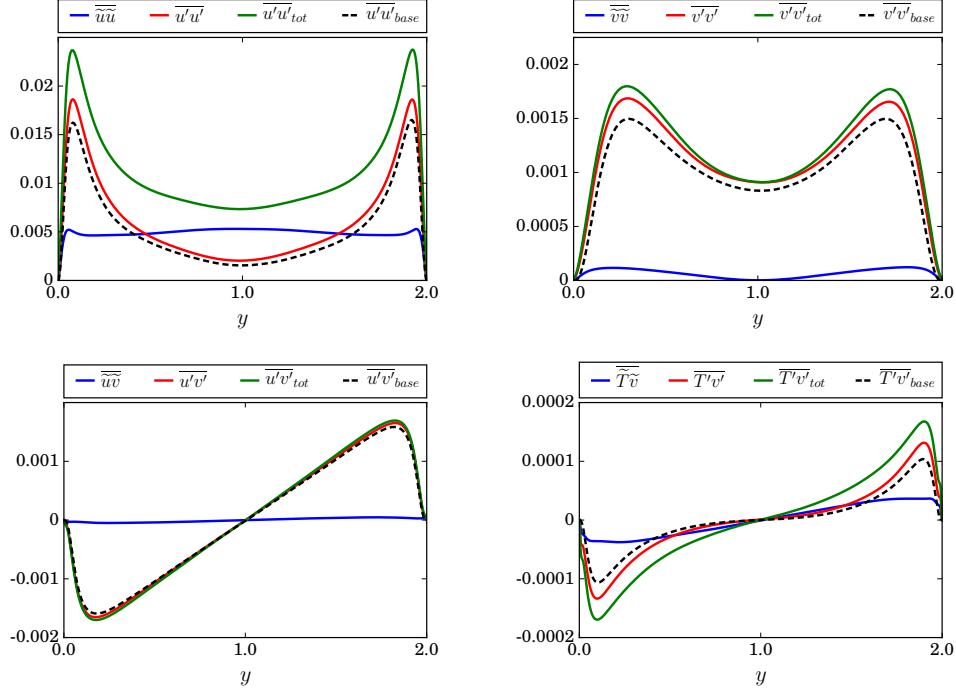


Figure 3.16. Decomposition of total Reynolds stress terms as well as turbulent heat flux into the background and harmonic terms for subsonic configuration

Therefore, the positive effect of acoustic excitation of this type on heat transfer transfer enhancement with minimally increasing the skin friction can be observed in second order time statistics as well.

3.2.4 On the Efficacy of the Linear Stability Analysis in Selecting the Optimal Modes

In the first step, the eigenfunctions associated with the mode R_1 in both supersonic (C1) and subsonic (C2) cases, in figure 3.4, are compared against the outcomes of the fully non-linear simulations. Figure 3.17 (a) and (e) illustrate the harmonic component of temperature \tilde{T} at phase $t/\mathcal{T} = 1/4$ in both supersonic C1 and C2, respectively. If no non-linear interactions were involved, either among the superim-

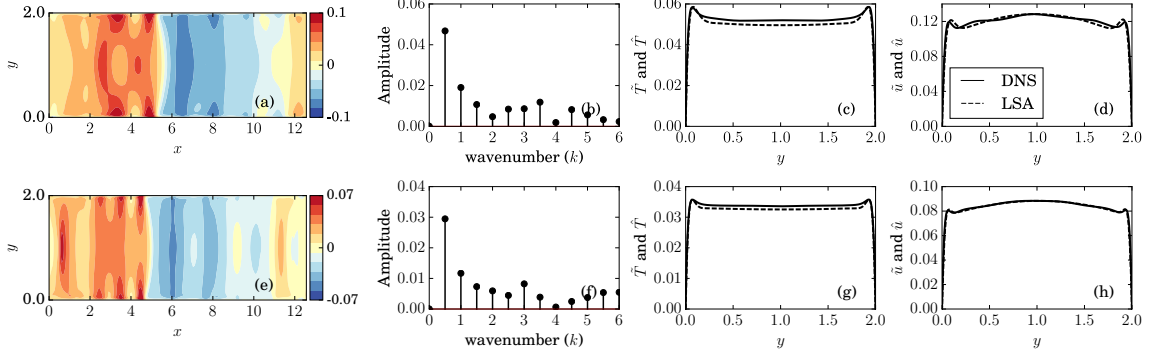


Figure 3.17. Phase-locked averaged temperature contours (at $t/\mathcal{T} = 1/4$) for supersonic (C1) and subsonic cases (C2) (a&e, respectively). Maximum and minimum values are truncated for better visualization. Spatial DFT of this field is illustrated in (b&f). Amplitude of the dominant mode ($k = 0.5$) is shown in (c&g) along with the temperature eigenfunction of the most unstable mode identified by LSA. Same procedure is repeated for the streamwise velocity in (d&h).

posed waves or between the waves and background turbulent field, we would expect to observe a single-frequency harmonic field, however, the present results suggest the presence of higher-frequency changes. A spatial Discrete Fourier Transform (DFT) is employed to extract the components corresponding to different wavenumbers. The highest amplitude is associated with $k = 0.5$, the wavenumber we set in the Linear Stability Analysis (LSA). Higher frequency components possess several times smaller amplitudes and are created as a result of non-linear interactions in the flow. We also compare the amplitude of \tilde{T} and \tilde{U} (harmonic component of streamwise velocity) corresponding to $k = 0.5$ against the mode shapes predicted by the LSA (performed on time-averaged unexcited flow quantities) in figure 3.17 (c&d) for C1, and (g&h) for C2. Results show an excellent agreement between these two profiles suggesting that the proposed technique resulted in exciting the specific mode identified by LSA.

In the second step, we consider two additional cases, C3 and C4, excited at off-optimal frequencies, namely $\omega_3 = 2\pi/4.00$ and $\omega_4 = 2\pi/5.00$, in order to assess

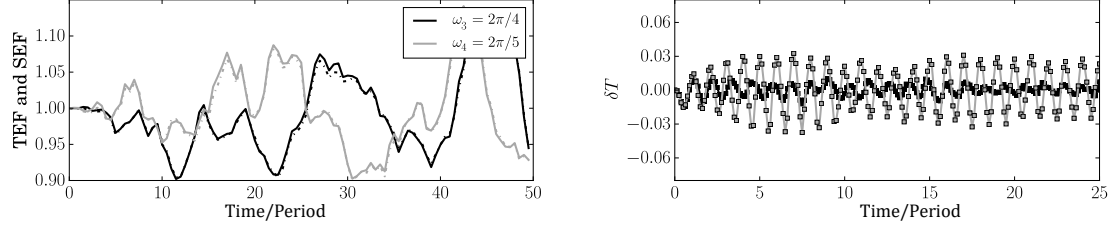


Figure 3.18. History of SEF and TEF (left) as well as temperature perturbation δT at the center of the forcing region (right) at $M_b = 1.5$ subjected to off-design excitation frequencies, case C3 in table 3.1 with $\omega_f = 2\pi/4.00$ is represented by black and case C4 with $\omega_f = 2\pi/5.00$ is shown as grey; on the left SEF (— · —) and TEF (—) overlap throughout the process.

the role of LSA in selecting the optimal excitation frequency. In both cases, the Stokes layer thickness as well as forcing amplitude is similar to C1 case, however, the acoustic resonance may not take place according to the LSA. Figure 3.18 reports the history of SEF and TEF as well as temperature perturbations. Growth of δT in these cases is significantly smaller than what observed in the corresponding resonant condition C1. Following a few excitation periods, the larger amplitude fluctuations interact non-linearly with the background flow which can either lead to the limit cycle oscillations (in the optimal condition), or experience stabilization. The latter is observed in the off-design frequencies through a periodic growth and decay in the perturbation amplitude. Moreover, SEF and TEF (figure 3.18-left) are tightly coupled and, although they both experience regions with values greater or smaller than unity, time-averaging over 50 cycles shows a minimal modification ($\approx 1\%$) in C_f and Nu . This highlights the need for applying the acoustic forcing at the optimal "resonant" frequency determined by Linear Stability Analysis.

3.2.5 Parametric Analysis of Acoustic Excitation for Heat Transfer Enhancement

The Effect of Forcing Amplitude on the Resonance and Streaming Quantities

Amplitude of acoustic forcing, i.e. A_f in Equation (3.1), plays a critical role in the formation of acoustic pulsations, their strength and possible interactions with the background turbulence. Here, three *additional* scenarios are introduced, A1 through A3, wherein the parameter A_f is varied in $[0.125, 0.0625, 0.03125]$ while keeping the forcing frequency constant at $\omega_f = 2\pi/6.94$. These simulations are performed at $Re_b = 3000$ and $M_b = 0.75$, starting from the same initial flow fields as the case C2, and with the same time-step size. Figure 3.19 (right) illustrates the temperature perturbations δT , in the first 25 excitation periods at center of the forcing region ($y = 1$). This quantity, similar to figure 3.6, is averaged in the forcing region $x \in [1.87 - 2.37]$ and along the spanwise direction. Wave heights (crest to trough distance) in the first pulsation period, as well as in the limit cycle oscillations, are reported in all four cases. This quantity in the start-up phase is linearly correlated with the forcing amplitude, e.g. A_f in case A3 (shown in plot f) is twice the forcing amplitude associated with case A2 (shown in plot h) and wave height in the start-up region is also approximately twice as much as case A2. As such, at high values of A_f , the initial perturbation amplitude is larger and non-linear effects dominate the oscillation dynamics faster and therefore, limit-cycle oscillation is reached in fewer pulsation periods. In this phase, however, the wave height approximately scales with $\approx \sqrt{A_f}$. These results are in line with findings of Yano [9] regarding the formation of periodic shock-waves and scaling of their amplitudes.

The overall effect of excitation amplitude on the near-wall heat and momentum transport has been investigated by looking at the history of Thermal and Shear Enhancement Factors, respectively shown by solid and dash-dotted lines in figure 3.19 (left). In case A3, with the smallest excitation amplitude $A_f = 0.03125$, SEF and

TEF exhibit almost identical behavior in time which indicates that momentum and heat transport processes, under the corresponding condition, are closely coupled. By increasing the excitation amplitude (from bottom to top), these two parameters gradually detach although following a similar trend. It suggests that such excitation can effectively energizes the heat transfer process while affecting the momentum transport to a lesser degree.

Figure 3.20 demonstrates the second-order turbulent statistics associated with the abovementioned cases, as well as the unexcited flow, along the channel height. Among all velocity fluctuation components, the prescribed acoustic excitation affects the streamwise component the most, where both the maximum value of $\overline{u'u'}$ and its magnitude at the channel center increase sharply by amplifying the forcing amplitude. This is expected as the forcing function (3.1) is only applied in the streamwise direction. The impact of such forcing on $\overline{v'v'}$ and $\overline{w'w'}$ is mainly visible near the peak-value and fades away closer to the channel center.

The most substantial impact of acoustic forcing is on the temperature fluctuations (shown on the bottom left). Therefore, we expect the turbulent heat flux $\overline{T'v'}$ to be more positively correlated with the amplitude of excitation than the Reynolds stress term $\overline{u'v'}$ and this is shown on the bottom-center and bottom-right plots. Both figures in the near-wall region, magnified in the insets, show a kink visible at large forcing amplitudes that is more pronounced in $\overline{T'v'}$ term and represents the dissipation introduced by near-wall weak periodic shock waves.

Figure 3.21 looks into the acoustic excitation and its effect on the background flow from a different perspective by considering the setting where, in case C1, the forcing term is turned-off after reaching the limit-cycle oscillations. The bottom row shows the temperature perturbation δT and top row presents the history of SEF and TEF highlighting the impact of excitation on heat and momentum transport near the wall. The vertical line at $t/\mathcal{T} = 50$ marks the instance where forcing is deactivated. Prior to this line, these two plots are identical to figure 3.19 (a and b), whereas upon crossing this point, the amplitude of perturbations decay exponentially. The inset

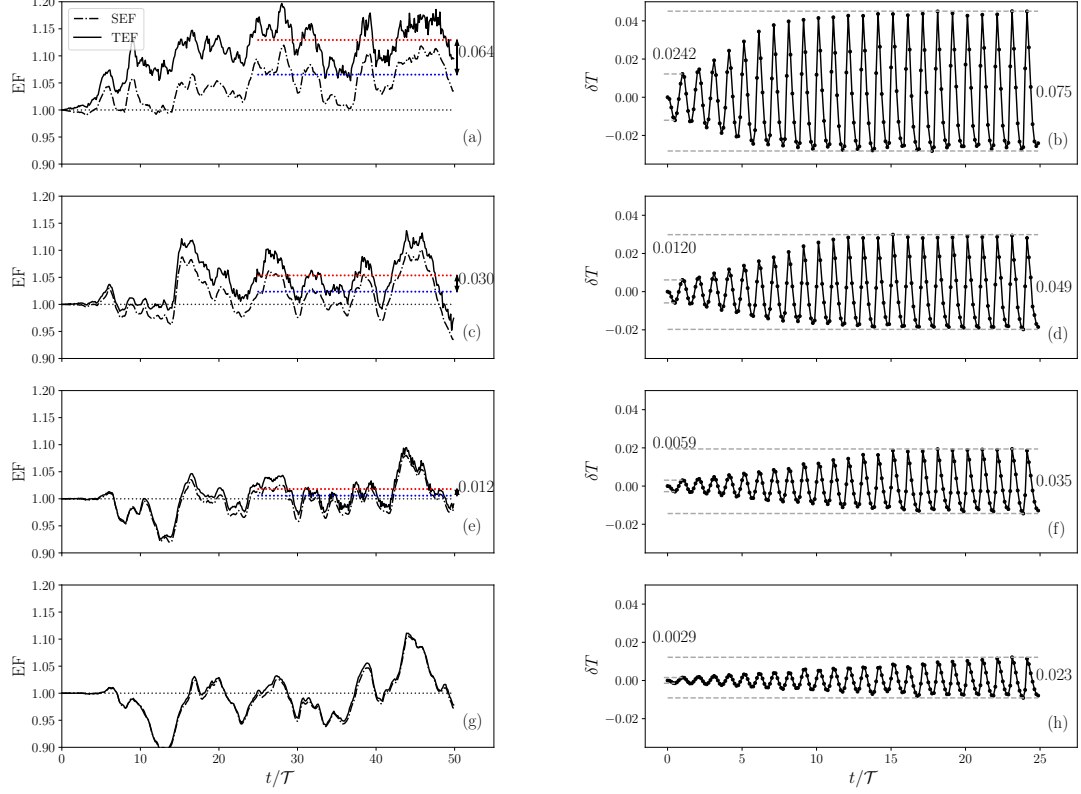


Figure 3.19. Temporal evolution of temperature fluctuations (δT) at the center of the forcing region, $y = 1$, at four different forcing amplitudes. This quantity is spatially averaged within $x \in [1.87-2.37]$ and $z \in [0, 1.5\pi]$ (right). Wave heights in the start-up as well as the limit-cycle regions are reported on the plots. History of SEF ($-\cdot-\cdot-$) and TEF ($---$) are also presented as a function of pulsation period (left). Plots (a and b) represent the case C2 with $A_f=0.25$, and (c and d) refer to the case A1 with $A_f = 0.125$. (e and f) and (g and h) are respectively associated with the cases A2 where $A_f = 0.0625$ and A3 where $A_f = 0.03125$. $\overline{\text{TEF}}$ (\cdots) and $\overline{\text{SEF}}$ (\cdots) taken over the last 25 cycles along with the offset between these two quantities are reported on the graphs.

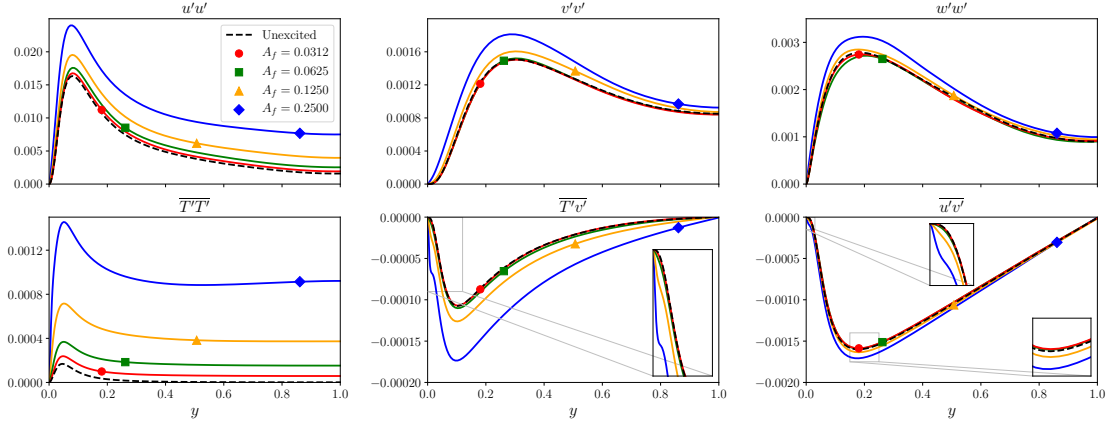


Figure 3.20. Second-order turbulent statistics at $Re_b = 3000$ and $M_b = 0.75$ subjected to excitation at different forcing amplitudes; unexcited case (---), A3 with $A_f = 0.031$ (●), A2 with $A_f = 0.062$ (■), A1 with $A_f = 0.125$ (▲) and C1 with $A_f = 0.250$ (◆). Time-averaging is taken over the first 50 pulsation periods and spatially averaged in streamwise and spanwise directions.

shows the level of temperature perturbations δT , 40 cycles after disabling the forcing term. Although the amplitude of perturbations is significantly reduced, sharp jumps at the starting instance of each cycle suggests the continuation of weak periodic shock waves even after cutting off the external source of pulsation. In terms of Enhancement Factors, there is a clear offset between SEF and TEF as long as excitation persists. Even after setting A_f to zero, there is a *relaxation period* where TEF remains larger than SEF for approximately 5 cycles (highlighted with red shadow) indicating that we can still obtain positive streaming effects by *periodic* activation of the external source to minimize the energy input. After this period, heat and momentum transport exhibit a strong pairing, similar to the case with low excitation amplitude, e.g. figure 3.19 (e and f), which theoretically approaches to unity for both quantities.

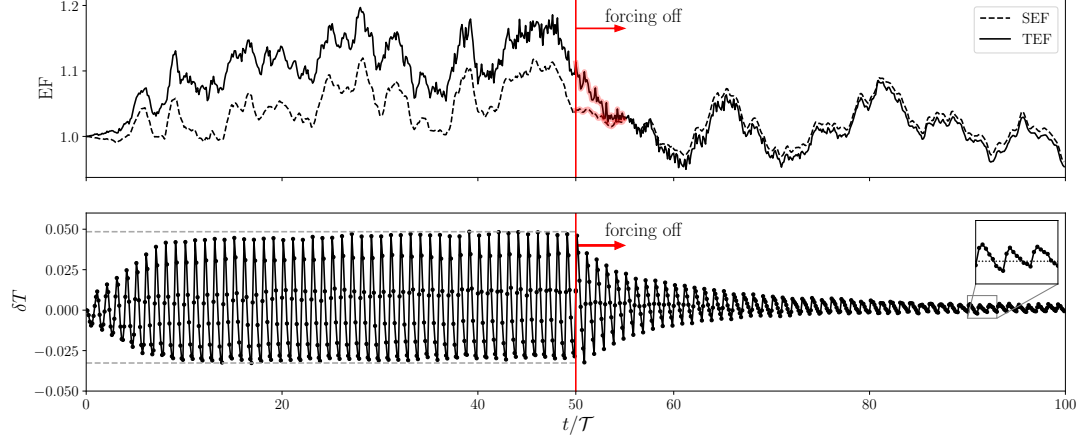


Figure 3.21. Response of an acoustically excited channel flow at $Re_b = 3000$ and $M_b = 0.75$ to sudden de-activation of forcing source. The system is initially subjected to the acoustic excitation at $A_f = 0.25$ and $\omega_f = 2\pi/6.94$. History of temperature perturbations δT (bottom) and SEF and TEF (top).

Acoustic Resonance at Higher Reynolds Number

Although all the simulations presented before are performed at $Re_b = 3000$, the conclusions drawn regarding the resonance and its impact on the heat and momentum transport are not limited to this specific condition. To elaborate more on this, case I1 has been selected where the Reynolds number is increased to $Re_b = 6000$, and Mach number is remained constant at $M_b = 0.75$. The domain size is identical to the case C2, and to keep the numerical resolution constant, number of grid points are increased twice in each direction, i.e. $N_x \times N_y \times N_z = 288 \times 256 \times 192$. Performing LSA on time-averaged quantities identifies the optimal excitation frequency at $\omega_f = 2\pi/6.954$ which is close to the value obtained for case C2 indicating that this mode is not too sensitive to the Re_b , unlike the M_b . Figure 3.22 displays the history of Enhancement Factors as well as temperature perturbations resulted from applying a forcing identical to the one used for C2. Time-averaging in the last 10 cycles shows $\overline{TEF} = 1.105$ and $\overline{SEF} = 1.033$ suggesting a net positive heat transfer enhancement compared to the

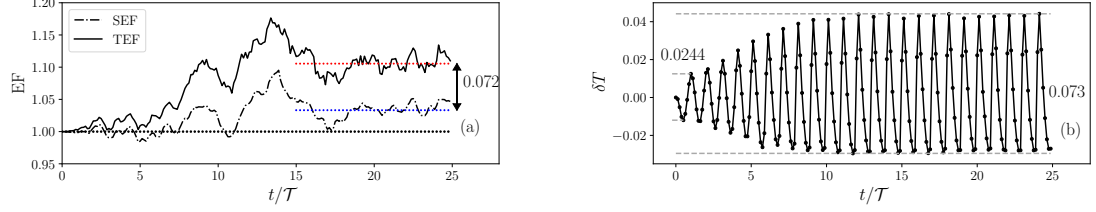


Figure 3.22. History of space-averaged Enhancement Factors (left) and temperature fluctuations at the channel center within the forcing region (right) at $Re_b = 6000$ and $M_b = 0.75$. Forcing function is shown in Equation (3.1) with $A_f = 0.25$ and $\omega_f = 2\pi/6.954$. SEF (---), TEF (—), $\overline{\text{TEF}}$ (·····), and $\overline{\text{SEF}}$ (· · · · ·)

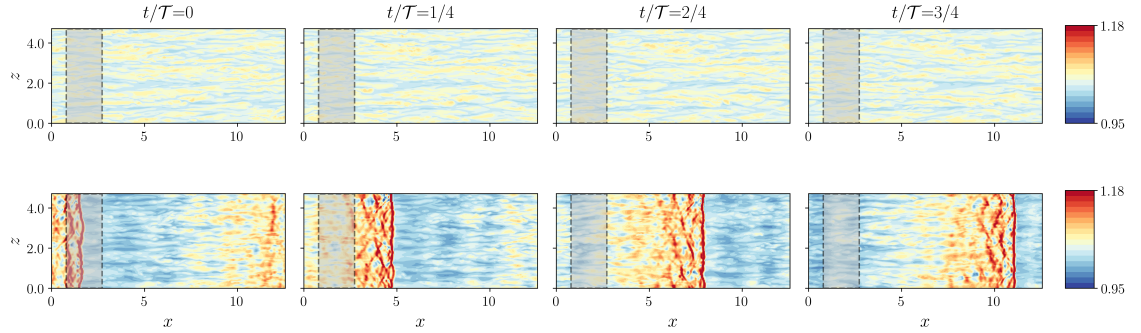


Figure 3.23. Instantaneous temperature field for an acoustically excited subsonic turbulent channel flow at $Re_b = 6000$ and $M_b = 0.75$. Top view at the bottom wall $y^+ \approx 4$ at four instances of one period. Top and bottom row respectively correspond to the unexcited and excited cases.

skin friction. Moreover, comparing the levels of δT in both start-up and limit-cycle regions with case C2 (figure 3.19 b) shows that the behavior of perturbations has remained mainly unchanged. Figure 3.23 shows the near wall turbulent structures, by looking at the temperature field at $y^+ \approx 4$, in both excited and unexcited case at four different instances of one period. Long streamwise streaks are clearly visible in the unexcited case (top row). However, the strong wave front, created as a result of resonance in the excited flow, followed by weaker waves, pass through these structures

and reshape them substantially. Between the passage of two wave trains there are some instances wherein turbulent flow relaxes towards its original state.

Resonance in Longer Domains

We have considered two cases, namely D1 and D2 in table 3.1, to study the acoustic resonance in longer domains. In these simulations, the operating conditions are similar to C2, i.e. $Re_b = 3000$ and $M_b = 0.75$, however, the domain length L_x is extended to $L_x = 6\pi$ and 8π and the number of grid points in this direction is also increased accordingly. The forcing function of form (3.1) is used with $A_f = 0.25$, similar to the case C2, and ω_f is found via the Linear Stability Analysis described in section 3.2.2. The history of temperature perturbations δT at the channel center, spatially averaged within the forcing region is plotted in figure 3.24 (b and d). Both cases show a transient growth in the amplitude of δT that quickly reaches the limit cycle oscillations within 10 pulsation periods. Shear and Thermal Enhancement Factors for these cases are plotted in figure 3.24 (a and c) where the solid line refers to the TEF and dash-dotted line shows the SEF. For comparison purpose, time-averaging is taken over the last 10 pulsation cycles for these two quantities and results are shown with red and blue dotted-lines, respectively. A clear separation is observed in both cases, suggesting a larger enhancement in Nu compared to the increase in C_f . For case D1, $\overline{TEF} = 1.100$ and $\overline{SEF} = 1.050$ while for case D2, $\overline{TEF} = 1.082$ and $\overline{SEF} = 1.038$. The offset in case D1 is slightly more pronounced, however, this may fall within the time-averaging uncertainty. One may conclude that by increasing the domain length, at least within the range studied in the present research, the impact of acoustic pulsations on the near-wall heat and momentum transport remains relatively intact, as long as the excitation frequency is adjusted accordingly.

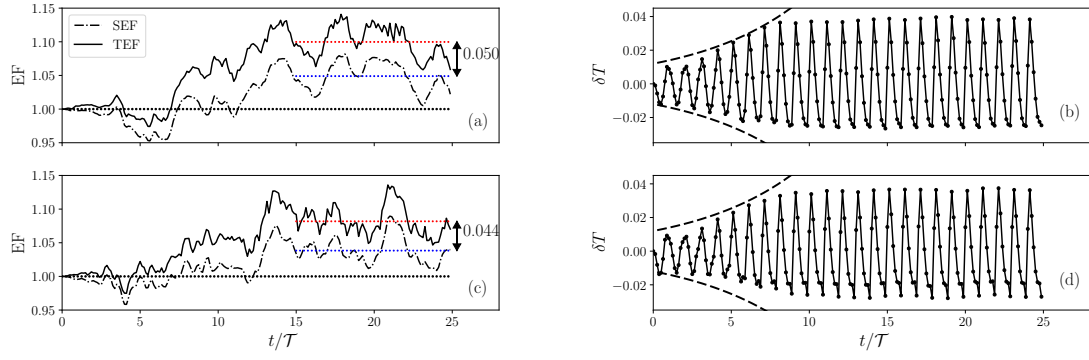


Figure 3.24. History of Shear and Thermal Enhancement Factors (a&c) as well as temperature perturbations δT at the channel center within the forcing region (b&c) for acoustically excited channels with length $L_x = 6\pi$ (top) and 8π (bottom). On the left, solid line refers to the TEF and dash-dotted line shows the SEF. Time-averaged value of these two quantities, taken over the last 10 cycles, are plotted with red and blue dotted-lines, respectively. Both cases show the resonance and a higher TEF compared to SEF (color online).

4. ACOUSTIC EXCITATION FOR HEAT TRANSFER REDUCTION IN HIGH-SPEED FLOWS

In the previous chapter, acoustic excitation was applied in the streamwise direction, where at relatively high forcing amplitudes, spanwise vorticities were formed that enhanced the heat transfer and skin friction. To alter the time-averaged flow variables, acoustic perturbations were required to overcome high inertial forces in the streamwise direction. Perpendicular to the flow direction, however, such inertial forces are negligible and therefore smaller perturbations may impact the flow more easily. The focus of this chapter is to analyze the effect of spanwise periodic excitation on the heat transfer and skin friction characteristics of wall-bounded compressible flow.

4.1 Problem Formulation

The proposed test case to explore the effect of spanwise acoustic excitation comprises repeating identical units of length L_x . Each unit includes a duct with an array of acoustic drivers mounted on both side walls operated 180° out of phase. A schematic view of this setup is shown in figure 4.1. Similar to the previous test case,

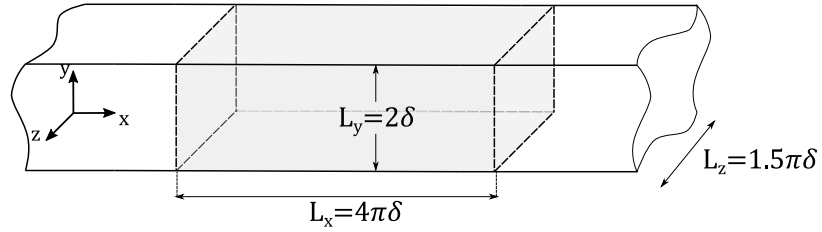


Figure 4.1. Proposed setup to analyze the acoustic excitation in the spanwise direction. Acoustic drivers are active in the entire shaded area. The effect of acoustic drivers mounted on side-walls operating 180° out of phase is modeled via forcing function of form (4.1)

only one unit needs to be simulated and given the geometrical symmetry present in the setup, the periodic boundary conditions is imposed in the streamwise direction. Complexities arising from the boundary layer formed on the side-walls are avoided by limiting the scope of the present study to the mid-span region and implementing the periodic boundary condition in the spanwise direction. Therefore, the simplified computational setup includes two parallel plates of length L_x and width L_z separated by distance 2δ . The effect of acoustic drivers is modeled with an external forcing following:

$$\vec{f}_f(\mathbf{x}, t) = A_f \sin(\omega_f t) \hat{e}_z \quad (4.1)$$

where A_f indicates the forcing amplitude and ω_f is the excitation frequency. Due to the out-of-phase operation of the speakers, the forcing only has one spanwise component. In the absence of any forcing in the streamwise direction, the perturbations decay rapidly upon leaving the affected region. Therefore, unlike the previous chapter, the entire side-walls are covered with the speakers, while the amplitude of forcing has been reduced. Moreover, it is assumed that all points along the spanwise direction instantly feel the perturbations. This is possible as a result of negligible "mean Mach number" in the spanwise direction. It should be noted that since the streamwise Mach number is relatively high, flow speed is comparable with the propagation speed of perturbations and therefore, this assumption would not hold for streamwise excitation.

Spatially uniform forcing allows for exploring smaller frequencies in a small domain since there is no need to accommodate for one (or more) wavelength in the direction of propagation within the domain. Therefore, studying the interaction of different turbulent scales and the Stokes layer is more visible.

Table 4.1.

Simulation parameters for the acoustic excitation normal to the flow in spanwise direction for a supersonic channel flow at $M_b = 1.5$

Case	Re_b	A_f	ω_f	$N_x \times N_y \times N_z$	$\delta_s^+ = \delta_s u_\tau / \nu_w$
C1	3000	0.05	$2\pi/20$	$144 \times 128 \times 96$	10.5
C2	3000	0.05	$2\pi/40$	$144 \times 128 \times 96$	14.8
C3	3000	0.05	$2\pi/80$	$144 \times 128 \times 96$	21.0
C4	3000	0.05	$2\pi/120$	$144 \times 128 \times 96$	25.7
A1	3000	0.20	$2\pi/5$	$144 \times 128 \times 96$	5.2
A2	3000	0.10	$2\pi/10$	$144 \times 128 \times 96$	7.4
A3	3000	0.025	$2\pi/40$	$144 \times 128 \times 96$	14.8
A4	3000	0.0125	$2\pi/80$	$144 \times 128 \times 96$	21.0
A5	3000	0.00834	$2\pi/120$	$144 \times 128 \times 96$	25.7
A6	3000	0.00625	$2\pi/160$	$144 \times 128 \times 96$	29.7

4.2 Results

Direct Numerical Simulation is performed for seven different frequencies at different forcing amplitude. These frequencies are chosen such that the resulting Stokes layer falls at different heights of the channel interacting with different regions of the near-wall turbulent boundary layer. Table 4.1 summarizes the simulation parameters and the associated Stokes boundary layer thickness where $\delta_s = \sqrt{2\nu_w/\omega_f}$ as well as its corresponding non-dimensional form $\delta_s^+ = \delta_s u_\tau / \nu_w$ in wall units.

In all the above-mentioned cases, a computational domain of size $L_x \times L_y \times L_z = 4\pi\delta \times 2\delta \times 1.5\pi\delta$ is discretized by $N_x \times N_y \times N_z = 144 \times 128 \times 96$ elements and fully compressible Navier-Stokes equations (2.1) are solved using the sixth-order compact finite difference scheme for spatial derivatives and a third-order Runge-Kutta method for time-advancement. Volume mass flow rate, and subsequently bulk Mach number M_b , by adjusting a forcing term in momentum and energy equations following the approach described in section 3.2.1.

One other simulation is also conducted without applying the additional forcing, which serves as the *reference unexcited solution*. Comparing this case with the acoustically excited simulations helps isolate the effect of the perturbation on the flow. All simulations are initialized with the same flow field obtained from the base flow calculations 3.2.1 and by keeping all other parameters, including time step size, constant.

4.2.1 Temporal Evolution of Perturbations

Since the boundary layer excitation is applied via imposing an external forcing of form (4.1), monitoring the resulting spanwise velocity perturbations, $\delta w = w_{\text{excited}} - w_{\text{unexcited}}$ can give a better understanding on how this forcing is translated into sensible flow quantities. Figure 4.2 (right column) plots the history of the spatially-averaged spanwise velocity perturbations at the channel center, $y^+ \approx 215$. In all these cases, velocity perturbation amplitude starts with oscillatory, but purely positive values, and eventually leads to zero-mean oscillations in the limit cycle, achieved around $t \approx 480$. Wave-height (min-to-max value) in each case is reported on 4.2 (right) which is inversely proportional to the excitation frequency. To analyze the effect of the prescribed excitation on the heat and momentum transport, history of Shear Enhancement Factor (SEF) and Thermal Enhancement Factor (TEF) are plotted in figure 4.2 (left column). Recall the Equation (3.4),

$$\text{SEF} = \frac{C_{f,\text{exc}}}{C_{f,\text{unexc}}} \quad \text{and} \quad \text{TEF} = \frac{Nu_{\text{exc}}}{Nu_{\text{unexc}}} \quad ((3.4))$$

where,

$$Cf = \frac{\mu_w \frac{\partial U}{\partial y}|_w}{0.5\rho U_b^2} \quad \text{and} \quad Nu = \frac{\frac{\partial}{\partial y}(T - T_w)|_w}{(T_b - T_w)/\delta}.$$

Utilizing these two quantities, C_f and Nu of the excited case at each point in time is compared against the corresponding values in the unexcited setup at the exact same time. The overall trend of both quantities shows an oscillatory yet decreasing

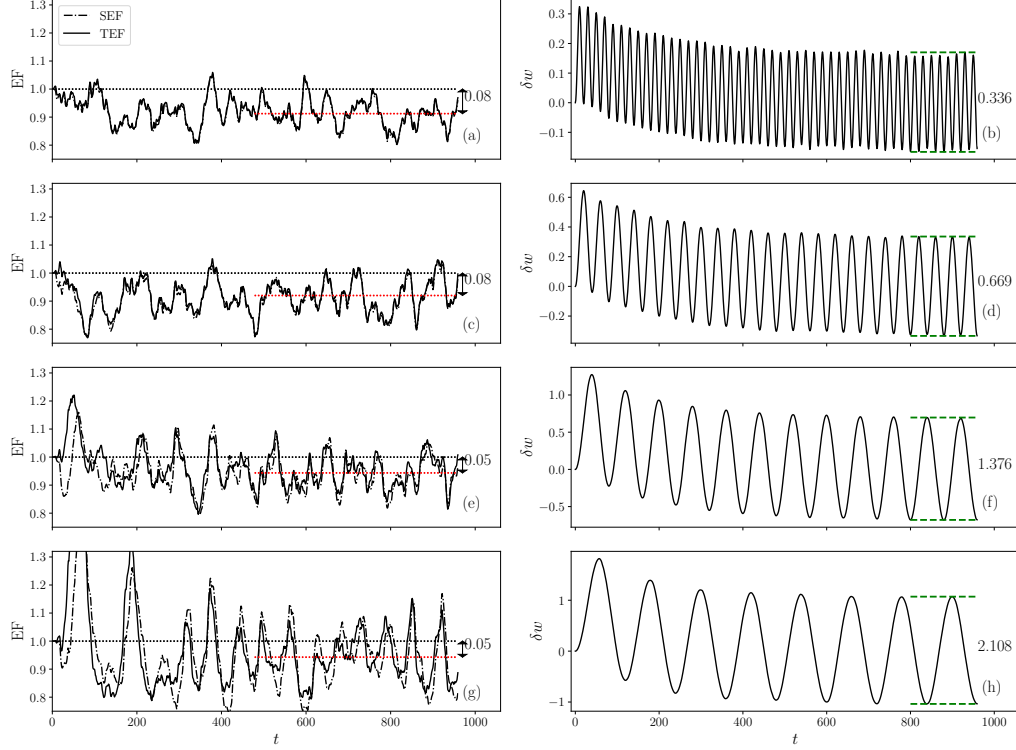


Figure 4.2. History of the space-averaged SEF ($-\cdot-\cdot-$) and TEF ($—$) (3.4) (left) and spanwise velocity perturbations (δw) at the channel centers for cases C1 to 4; (a&b): $\omega_f = 2\pi/20$, (c&d): $\omega_f = 2\pi/40$, (e&f): $\omega_f = 2\pi/80$, (g&h): $\omega_f = 2\pi/120$ at $Re_b = 3000$, $M_b = 1.5$. In all the cases studied here, the forcing amplitude is constant $A_f = 0.05$. Time-averaged $\overline{\text{TEF}}$ taken during the limit-cycle oscillations is shown on all plots via a dashed-line ($- - -$) and the changes in this quantity due to excitation is reported on the graphs. Moreover, the wave height corresponding to δw in each case is also denoted on the right column.

behavior. As discussed in the previous chapter, if the *Reynolds Analogy*, or any other linear relationship between C_f and Nu holds, SEF and TEF must remain equal in the entire process. This is valid in figure 4.2 (a) corresponding to the case C1 with the highest frequency, $\omega_f = 2\pi/20$. As the excitation frequency decreases, the amplitude of spanwise velocity fluctuations increases and the Stokes layer becomes thicker. Therefore, the resulting Stokes layer formed normal to the flow direction

interacts with the turbulent background flow more strongly and disrupts the near wall structures responsible for heat transfer and drag. This is visible from the deviation of SEF from TEF in plot (g). Time-averaged $\overline{\text{TEF}}$, taken in the limit cycle region is reported on each plot of figure 4.2. The largest heat transfer reduction is achieved in the first two cases with $\mathcal{T} = 20$ and 40, where Nu reduced by 8% as a result of acoustic excitation.

4.2.2 Near-wall Instantaneous Flow Fields

Near-wall coherent structures can be used to describe the main characteristics of a turbulent field and, herein, the instantaneous temperature field is employed to identify these structures. Figure 4.3 displays the temperature fields near the bottom wall (at $y^+ \approx 4$) in the excited (C1, $\omega_f = 2\pi/20$) and unexcited conditions $T_{\text{unexcited}}$. Temperature perturbations, δT , as a result of excitation has also been reported at four instances of a period. The unexcited case shows a pack of low-speed streamwise-oriented streaks, indicating the classical pattern of a low-Reynolds near-wall turbulent flow field. In this high-frequency case, a small distortion is seen in the near-wall structures, streaks are not completely streamwise, and some are slightly tilted up or downwards. Overall, the density of hot regions is shown to be decreased, which suggests a reduction in the near-wall heat transfer. Figure 4.4 and 4.5 illustrate these three quantities for case C2 and C3 where $\omega_f = 2\pi/40$ and $\omega_f = 2\pi/80$, respectively. In these figures, the interaction between the main and cross-flow is more accentuated due to larger spanwise velocity perturbation amplitude, δw . At $t/\mathcal{T} = 0$ and $t/\mathcal{T} = 2/4$, the streaks create a more acute angle with the streamwise direction and $t/\mathcal{T} = 1/4$ and $t/\mathcal{T} = 3/4$ instances, clearly mark the transition from negative to positive spanwise pulsations. Looking at the δT fields, one may observe that case C2 experiences an overall reduction in the concentration of the hot regions while drawing a similar conclusion from the outcomes of case C3 is less obvious. Essentially, large modifications in the skin friction and heat transfer characteristics of the flow can be

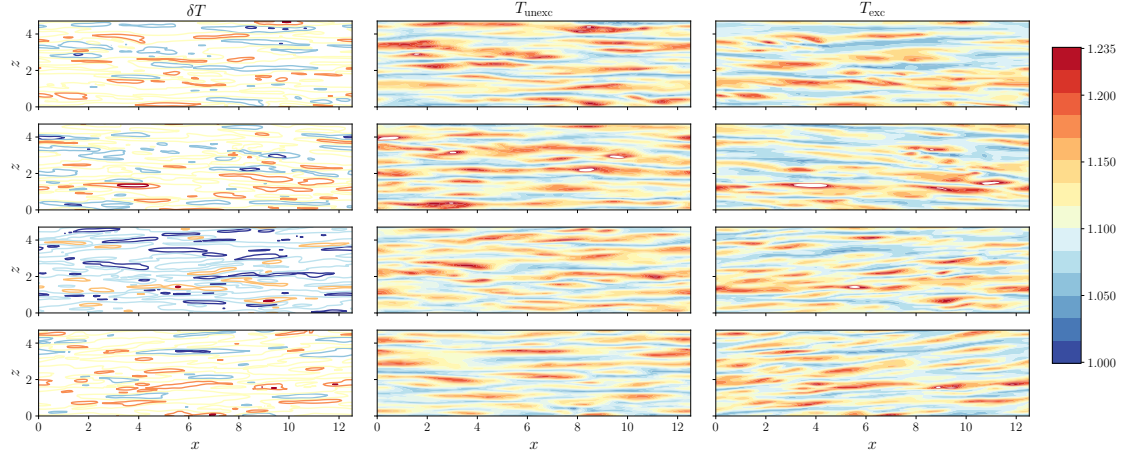


Figure 4.3. Temperature fields near the bottom wall at $y^+ \approx 4$. Simulations are performed at $Re_b = 3000$ and $M_b = 1.5$; excited case at $A_f = 0.05$ and $\mathcal{T} = 20$, corresponding to case C1 (right), unexcited case (middle), and temperature perturbation, δT (left). Each row corresponds to one instance within the first period of the limit cycle oscillations; from top to bottom $t/\mathcal{T} = 0$, $t/\mathcal{T} = 1/4$, $t/\mathcal{T} = 2/4$, and $t/\mathcal{T} = 3/4$

attributed to the alteration of these near-wall structures. To have a clear look at the near-wall vortical structures, the iso-value contours of Q-criterion for the case C1 are plotted in figure 4.6 at four instances of a period (\mathcal{T}). These graphs only focus on a sub-domain confined within the planes $y = 0$ and $y = 0.05$ and are acquired in a period after the transition phase is passed, namely $t \in [480, 485, 490, 495]$. The distortion in the near-wall streamwise structures is visible in all instances, especially in $t/\mathcal{T} = 0$ where a slit is formed from the bottom-left to top-right. Large structures are broken into less-organized and smaller ones which results in disrupting the cycle of turbulence generation.

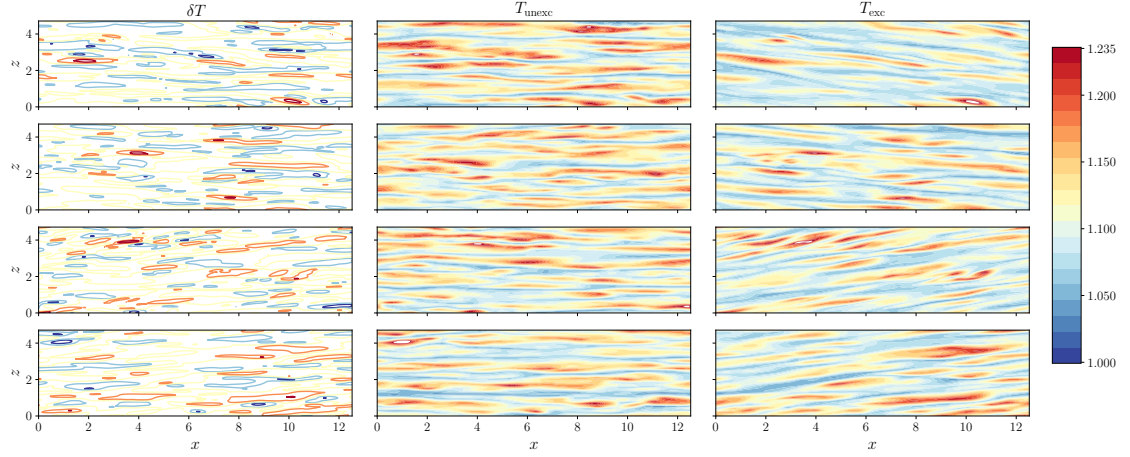


Figure 4.4. Temperature fields near the bottom wall at $y^+ \approx 4$. Simulations are performed at $Re_b = 3000$ and $M_b = 1.5$; excited case at $A_f = 0.05$ and $\mathcal{T} = 40$, corresponding to case C2 (right), unexcited case (middle), and temperature perturbation, δT (left). Each row corresponds to one instance within the first period of the limit cycle oscillations; from top to bottom $t/\mathcal{T} = 0$, $t/\mathcal{T} = 1/4$, $t/\mathcal{T} = 2/4$, and $t/\mathcal{T} = 3/4$

4.2.3 Time-averaged and Phase-Locked Averaged Statistics

The impact of spanwise pulsations on the first-order time statistics of the flow quantities is illustrated in figure 4.7. This figure displays the streaming velocity components in the spanwise and streamwise directions as well as the temperature, following

$$q_{st} = \bar{q}_{\text{excited}} - \bar{q}_{\text{unexcited}} \quad (4.2)$$

for C1 to C4 cases, where q is a generic quantity and \bar{q} represents the time-averaged quantity calculated during the limit-cycle oscillations (where $t > 480$). All the considered cases result in a similar distribution of U_{st} along the channel height; a non-zero streaming velocity appears near the wall, opposite to the flow direction, whose magnitude decreases by approaching the channel center and may take small positive values. The magnitude and location of the peaks in U_{st} are similar in case C1 and

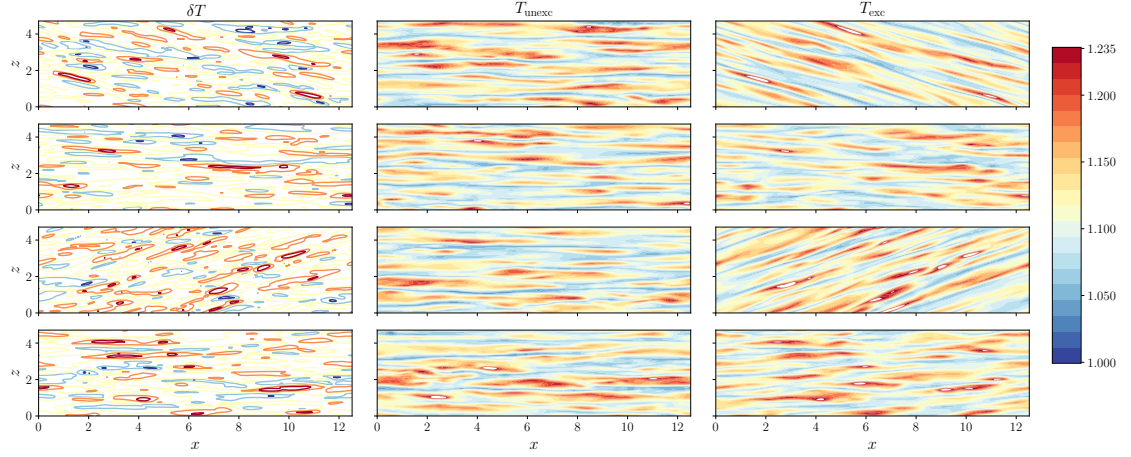


Figure 4.5. Temperature fields near the bottom wall at $y^+ \approx 4$. Simulations are performed at $Re_b = 3000$ and $M_b = 1.5$; excited case at $A_f = 0.05$ and $\mathcal{T} = 80$, corresponding to case C3 (right), unexcited case (middle), and temperature perturbation, δT (left). Each row corresponds to one instance within the first period of the limit cycle oscillations; from top to bottom $t/\mathcal{T} = 0$, $t/\mathcal{T} = 1/4$, $t/\mathcal{T} = 2/4$, and $t/\mathcal{T} = 3/4$

C2. At larger excitation periods, namely, case C3 and C4, the peak's location moves slightly towards the channel center, and the near-wall slope slightly decreases. This can also be verified in terms of SEF in figure 4.2. Spanwise component of the streaming velocity, W_{st} , peaks near $y \approx 0.25$, where its magnitude increases by reducing the excitation frequency. In high-frequency cases, the viscous effects are more confined near the wall, and the magnitude of W_{st} near the channel center remains small. At lower frequencies with larger perturbation's amplitudes and thicker Stokes layer thicknesses, the distribution of W_{st} is more complicated and involves multiple peaks. Streaming temperature T_{st} associated with high-frequency excitation, takes negative values near the boundary implying that the wall is cooled due to the excitation, while temperature profile near channel center is unchanged (at $\mathcal{T} = 20$) or slightly increases (at $\mathcal{T} = 40$). Results at lower frequencies indicate that the excitation contributes to heating the flow across the channel.

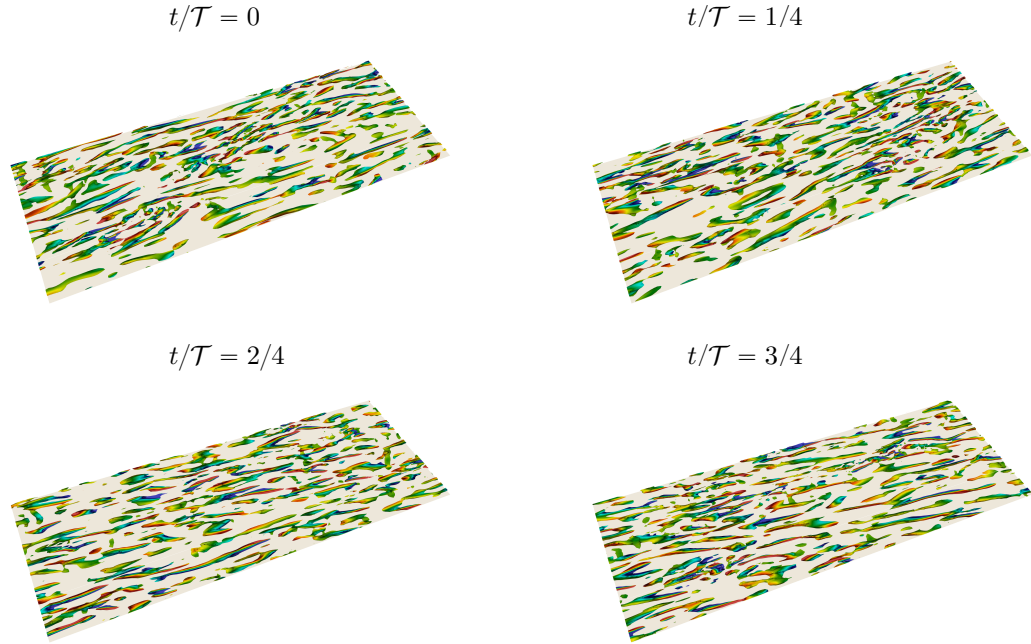


Figure 4.6. Instantaneous Q-criterion in a sub-domain confined between the bottom wall and $y = 0.05$ in the excited condition of C1 for a supersonic turbulent channel flow at four instances of one period (\mathcal{T}). The structures are colored by their corresponding wall-normal velocity component from blue (negative) to red (positive values).

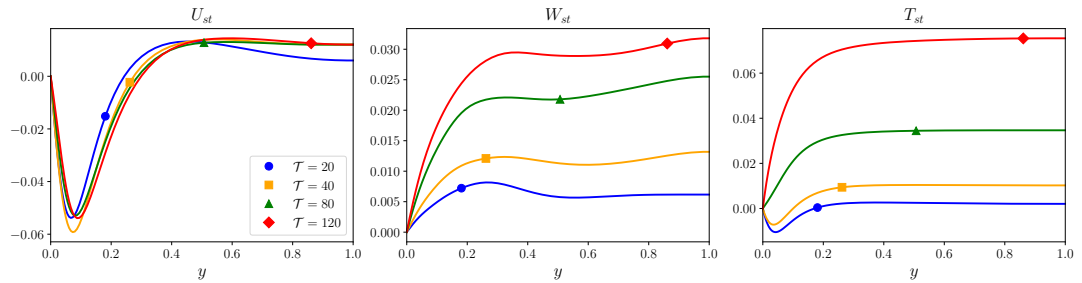


Figure 4.7. Streaming velocity components in both streamwise (left) and spanwise (middle) directions along with the streaming temperature (right). Simulations are performed at $Re_b = 3000$ and $M_b = 1.5$ subjected to the spanwise forcing of form (4.1) at $A_f=0.05$ for C1: $\omega_f = 2\pi/20$ (\bullet), C2: $\omega_f = 2\pi/40$ (\blacksquare), C3: $\omega_f = 2\pi/80$ (\blacktriangle), and C4: $\omega_f = 2\pi/120$ (\blacklozenge)

Decomposition of instantaneous flow quantities into the time-averaged, harmonic, and random terms is carried out following the Equation (3.5), repeated here:

$$\phi(\mathbf{x}, t) = \underbrace{\overline{\phi(\mathbf{x})}}_{\text{steady term}} + \underbrace{\widetilde{\phi(\mathbf{x}, t)}}_{\text{harmonic term}} + \underbrace{\phi'(\mathbf{x}, t)}_{\text{random fluctuation}} \quad ((3.5))$$

where the harmonic term is found from the phase-locked averaging at the excitation frequency:

$$\langle \phi(\mathbf{x}, t) \rangle = \frac{1}{N+1} \sum_{n=0}^N \phi(\mathbf{x}, t + n\mathcal{T}) \quad ((3.6))$$

where,

$$\widetilde{\phi(\mathbf{x}, t)} = \langle \phi(\mathbf{x}, t) \rangle - \overline{\phi(\mathbf{x})}$$

This formulation is employed to extract the harmonic component of spanwise velocity at cases C1 to C3 depicted in figure 4.8. The viscous penetration length $l_{\text{visc}} = 2\pi\sqrt{2\nu_w/\omega_f}$, calculated based on the viscosity at the wall is also marked on the plots. Since a large temperature gradient exists along the channel height, the fluid viscosity increases from the walls to the channel center, and therefore the presented relation for l_{visc} denotes the lower limit of this parameter. One should note that the y -axis

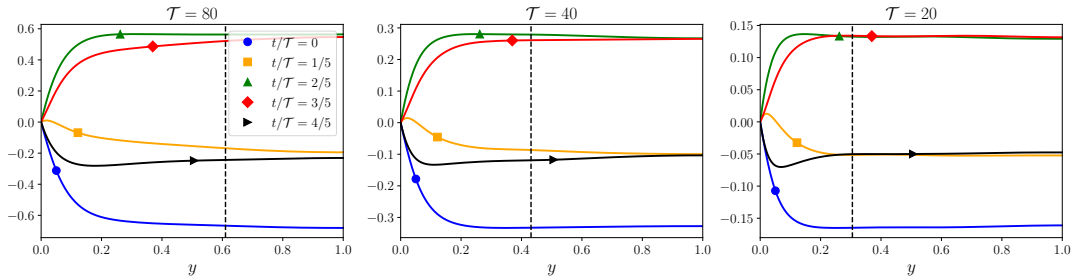


Figure 4.8. Phase-locked averaged spanwise velocity \widetilde{W} at five different instances of one period (\mathcal{T}); (right) excitation at $\omega_f = 2\pi/80$, (middle) $\omega_f = 2\pi/40$, and (left) $\omega_f = 2\pi/20$. The vertical dashed line (---) represents the viscous penetration length $l_{\text{visc}} = 2\pi\sqrt{2\nu_w/\omega_f}$, (\bullet) shows the starting phase of a period, i.e., $t/\mathcal{T} = 0/5$, (\blacksquare) $t/\mathcal{T} = 1/5$, (\blacktriangle) $t/\mathcal{T} = 2/5$, (\blacklozenge) $t/\mathcal{T} = 3/5$, and (\blacktriangleright) $t/\mathcal{T} = 4/5$

in figure 4.8 is doubled consecutively from right to left. We observe that the viscous effects are propagated further towards the channel center by increasing the period of excitation. This can be assessed by comparing the \widetilde{W} at $t/\mathcal{T} = 2/5$ and $t/\mathcal{T} = 3/5$ (positioned equally around the instance $t/\mathcal{T} = 1/2$). The closer these two profiles are, the less dissipation is present in the pulsations. Moreover, the overshoot observed at $t/\mathcal{T} = 4/5$ of $\mathcal{T} = 20$ is smoothed out in cases with lower frequency pulsation.

In all the simulations discussed above, cases C1 to C4, the forcing amplitude is kept constant while changing the excitation's frequency. This resulted in spanwise velocity perturbations with different amplitudes and also different Stokes layer thickness. These two factors affect the flow simultaneously, which complicates drawing a conclusion about the impact of each parameter on the heat transfer, drag, and turbulent statistics. Considering the figure 4.2, which suggests an inversely linear relationship between δw at the channel center and the forcing frequency ω_f , the parameter A_f/ω_f is kept constant in cases A1 to A6 in order to obtain a similar perturbation amplitude in the spanwise velocity and isolate the effect of forcing frequency on the results. Case C2 with $A_f = 0.05$ and $\omega_f = 2\pi/20$ is chosen as the reference, due to achieving the highest reduction in Nu as a result of the excitation corresponding to $A_f\mathcal{T} = 1$.

4.2.4 Temporal Evolution of the Perturbations Resulted from Different Forcing Amplitudes $A_f \propto 1/\mathcal{T}$

Temporal evolution of spanwise velocity perturbations in cases A1 to A6 along with case C1, (figure 4.9 e & f) as the reference case, are illustrated in figure 4.9. Min-to-max value of δw in the limit cycle is reported on each plot which for all cases lies $\in [0.318, 0.356]$ while the reference value, corresponding to case C1 is 0.336. This implies the level of spanwise perturbation is similar in all cases by keeping $A_f\mathcal{T}$ constant at unity. Analogous to figure 4.2, the oscillations begin as purely positive sinusoidal waves and after a transition region, at $t \approx 480$, δw oscillates around zero.

In these simulations, SEF and TEF closely follow each other, and therefore, only TEF is plotted in figure 4.9 along with the time-averaged $\overline{\text{TEF}}$ calculated during the limit-cycle oscillations reported in each case. Results suggest an optimum frequency for heat transfer (and drag) reduction around $\omega_f = 2\pi/10$ and $\omega_f = 2\pi/20$, corresponding to cases A2 and C1, respectively, with approximately 8% decrease in time and space-averaged \overline{Nu} . According to Jung et al [61], the excitation period can be non-dimensionalized with $\mathcal{T}^+ = \mathcal{T}u_\tau^2/\nu$, and its optimal value for drag reduction in an incompressible channel is $\mathcal{T}^+ = 100$. Dimensionless excitation period for A2 and C1 cases, as the optimal cases of the present work, are respectively $\mathcal{T}_{A2}^+ \approx 173$ and $\mathcal{T}_{C1}^+ \approx 346$ where the ν is calculated at the wall.

4.2.5 Time-averaged and Phase-Locked Averaged Statistics at Different Forcing Amplitudes $A_f \propto 1/\mathcal{T}$

The harmonic component of spanwise velocity for three cases at $A_f\mathcal{T} = 1$ is plotted in figure 4.10. One should note that here, all cases share the same y -axis, unlike figure 4.8, since the level of perturbations is kept the same in all cases. The theoretical value for the viscous penetration length l_{visc} , marked with the dashed lines, seems reasonable for high and medium frequency ($\omega_f = 2\pi/5$ and $\omega_f = 2\pi/20$), but is not as accurate in the low frequency case ($\omega_f = 2\pi/80$). The spanwise velocity perturbation near the Stokes layer thickness $\delta_s = \sqrt{2\nu_w/\omega_f}$ or $l_{\text{visc}}/2\pi$ overshoots the value at the channel core. This overshoot is most visible in the high-frequency case and becomes less effective as the excitation period increases. To better visualize the unsteady flow features, space-time correlations are illustrated in figure 4.11 for harmonic components of streamwise, spanwise, and temperature. Strong coupling is observed between these quantities. \widetilde{W} has a simple sinusoidal oscillation, with wavenumber $k = 1$ in time (horizontal axis). Sharp changes near the boundaries are also visible for the high-frequency cases. The second row of figure 4.11 represents the time evolution of harmonic streamwise velocity \widetilde{U} . A pattern with the wavenumber

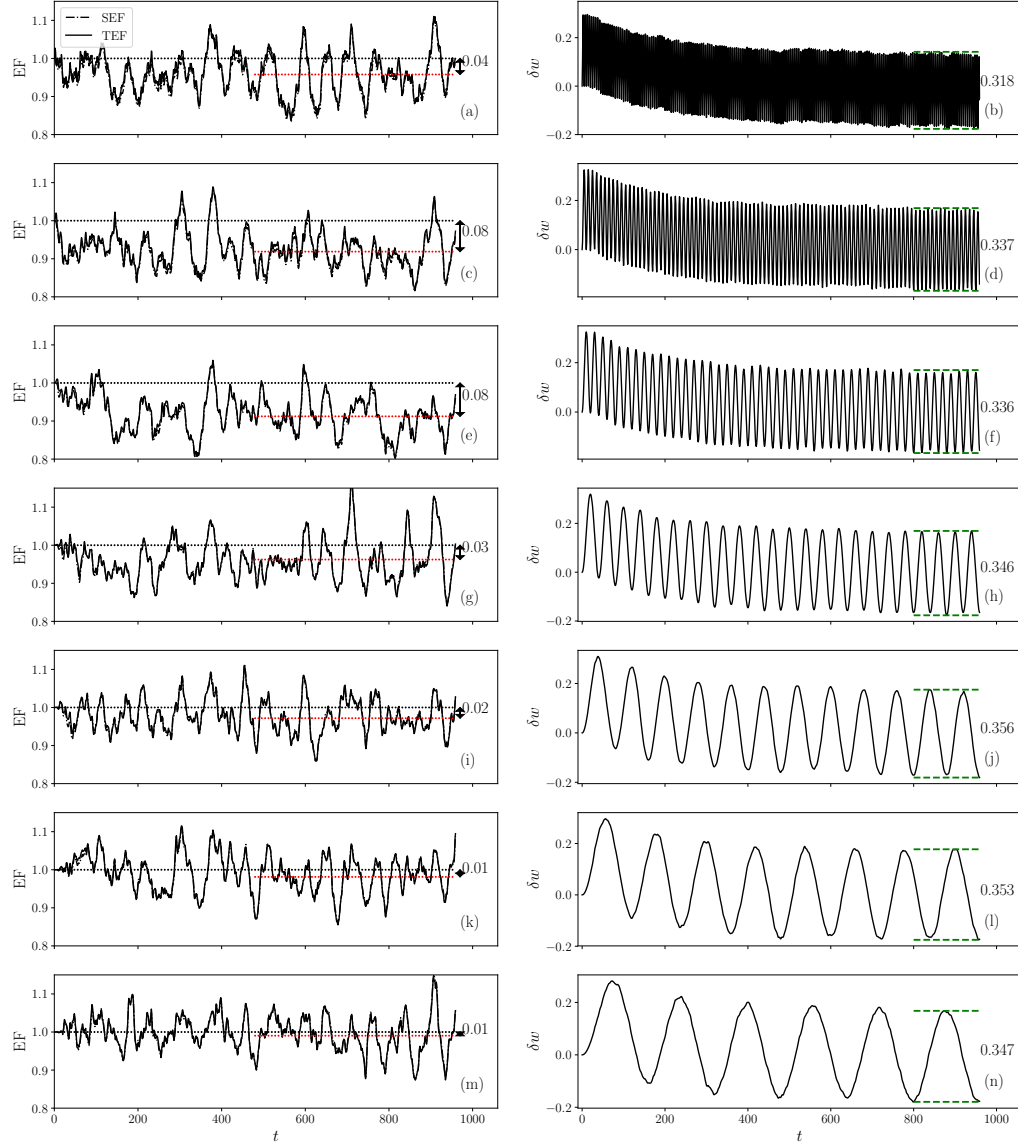


Figure 4.9. History of the space-averaged TEF (3.4) (left) and spanwise velocity perturbations (δw) at the channel centers for cases A1: $\mathcal{T} = 5$ (a&b), A2: $\mathcal{T} = 10$ (c&d), C1: $\mathcal{T} = 20$ (e&f) as the reference, A3: $\mathcal{T} = 40$ (g&h), A4: $\mathcal{T} = 80$ (i&j), A5: $\mathcal{T} = 120$ (k&l), and A6: $\mathcal{T} = 160$ (m&n) at $Re_b = 3000$, $M_b = 1.5$. In all cases forcing amplitude for each case is constant $A_f = 1/\mathcal{T}$. The wave height (min-to-max value) corresponding to each case is also denoted on each plot. Time-averaged $\overline{\text{TEF}}$ taken during the limit-cycle oscillations is reported on all plots via dashed-line (---) and the changes in this quantity due to excitation is printed on the graphs.

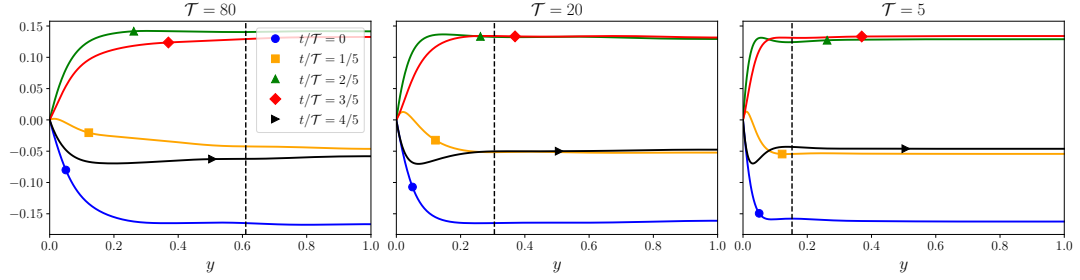


Figure 4.10. Phase-locked averaged spanwise velocity \widetilde{W} at five different instances of one period (\mathcal{T}); (right) excitation at $\omega_f = 2\pi/80$ and $A_f = 0.0125$, (middle) $\omega_f = 2\pi/20$ and $A_f = 0.05$, and (left) $\omega_f = 2\pi/5$ and $A_f = 0.2$. The vertical dashed line (---) represents the viscous penetration length $l_{\text{visc}} = 2\pi\sqrt{2\nu_w/\omega_f}$, (\bullet) shows the starting phase of a period $t/\mathcal{T} = 0/5$, (\blacksquare) $t/\mathcal{T} = 1/5$, (\blacktriangle) $t/\mathcal{T} = 2/5$, (\blacklozenge) $t/\mathcal{T} = 3/5$, and (\blacktriangleright) $t/\mathcal{T} = 4/5$

$k = 2$ can be clearly found in $\mathcal{T} = 10$ and $\mathcal{T} = 20$, while in the low-frequency case, the non-linear interaction with the background turbulent flow dissipates these perturbations and the dominant wave number remains at $k = 1$. Compared to the low and high-frequency cases, \widetilde{U} at $\mathcal{T} = 20$ is mostly concentrated near the walls, and oscillations vanish near the channel center at all instances of t/\mathcal{T} . Harmonic temperature component, \widetilde{T} , has a similar behavior as \widetilde{U} in time, while the effect of pulsation is more confined to the wall. Exposed to the prescribed perturbations, acoustic streaming appears in the flow that modifies the time-averaged velocity and temperature field. Streaming velocity in the spanwise and streamwise directions, as well as the streaming temperature profiles, are plotted in figure 4.12 for four different excitation frequency at $A_f\mathcal{T} = 1$. Similar to figure 4.7, profiles of $U_{f\perp}$ reveal the formation of the steady streaming in opposite to the main flow's direction effectively reducing the skin friction. By keeping the forcing amplitude (A_f) constant (in cases C1 to C4 shown in figure 4.7), the value of local minima near the wall is of the same order for all cases. However, we observe a non-monotonic behavior by increasing the A_f while keeping $A_f\mathcal{T}$ constant suggesting an interplay between these parameters

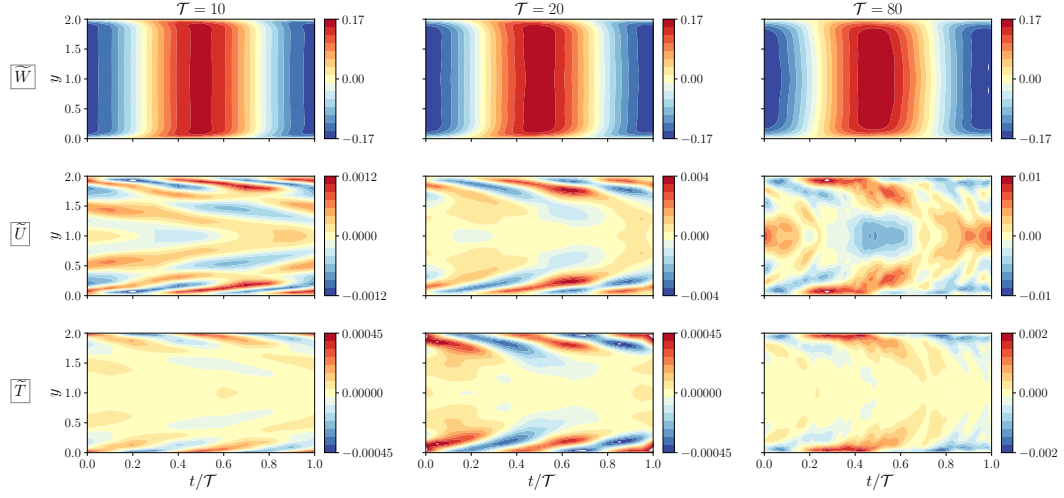


Figure 4.11. Space-time correlation in the spanwise velocity, \tilde{W} (top row), streamwise velocity, \tilde{U} (middle row), and temperature, \tilde{T} (bottom row) for three different excitation frequencies; $\mathcal{T} = 10$ (first column), $\mathcal{T} = 20$ (second column), $\mathcal{T} = 80$ (third column).

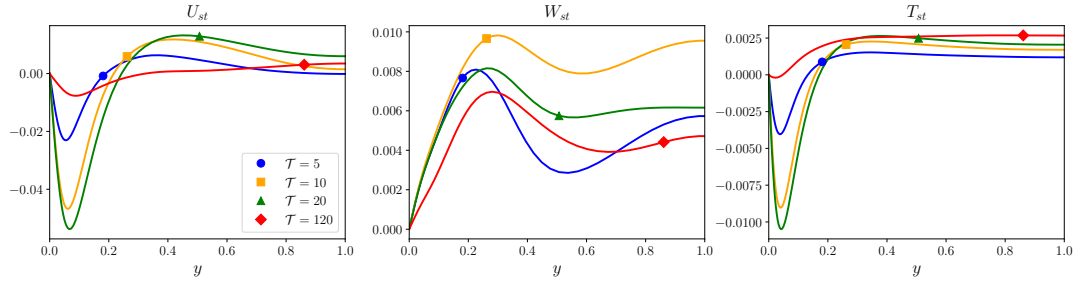


Figure 4.12. Streaming velocity components in both streamwise (left) and spanwise (middle) directions along with the streaming temperature (right). Simulations are performed at $Re_b = 3000$ and $M_b = 1.5$ subjected to the spanwise forcing of form (4.1) at $A_f \mathcal{T} = 1$ A1: $\omega_f = 2\pi/5$ and $A_f = 0.2$ (●), A2: $\omega_f = 2\pi/10$ and $A_f = 0.1$ (■), C1: $\omega_f = 2\pi/20$ and $A_f = 0.05$ (▲), and A5: $\omega_f = 2\pi/120$ and $A_f = 0.00834$ (◆)

which leads to an optimal condition at $\mathcal{T} = 0.05$ and $\mathcal{T} = 20$. A similar pattern is observed in streaming temperature; the local minima reaches its highest magnitude at $\mathcal{T} = 0.05$. It is worth noting that the location of this local minima point in U_{st} slightly moves towards the channel center with increasing the excitation frequency (it is also seen in the local maxima location), while in T_{st} it remains constant and is more confined to the wall. This shows that, under a specific condition, one can control the thermal and hydrodynamic boundary layer to respond differently to the pulsations. Streaming velocity in the spanwise direction, W_{st} , takes a similar form in all cases suggesting that the location of first overshoot is relatively independent of the excitation frequency.

Streamwise, wall-normal, and spanwise normal Reynolds stress terms at different pulsation periods, namely $\mathcal{T} = 5, 10, 20$ and 120 are plotted in figure 4.13 (top). Profiles corresponding to the unexcited case, as the reference values, are also reported with dashed-lines. The most visible difference due to the pulsation appears in the $\overline{w'w'}$; the peak values in all cases are more than twice larger than the unexcited value. The location of this peak monotonically moves closer to the channel center by increasing the pulsation period. Wall-normal component, $\overline{v'v'}$, decreases by applying the spanwise excitation. Low-frequency case (at $\mathcal{T} = 120$), minimally deviates from the unexcited case and the optimal reduction is achieved at $\mathcal{T} = 10$ and $\mathcal{T} = 20$. The streamwise component, $\overline{u'u'}$, remains nearly unchanged as a result of pulsation, except the peak value which again reaches the minimum at $\mathcal{T} = 10$ and $\mathcal{T} = 20$. Similar behavior is observed in $\overline{T'T'}$. Therefore, considering these four terms, it is expected that the turbulent heat flux, $\overline{T'v'}$, and Reynolds shear stress, $\overline{u'v'}$, would also experience a negligible change due to the low-frequency excitation. By tuning the ω_f to the optimal range, an effective reduction is achieved in both quantities.

Instantaneous temperature fields near the bottom wall at $y^+ \approx 4$, in both excited and unexcited conditions, as well as the temperature perturbations, δT , are displayed in figure 4.14 for case A4 that shows a small reduction in \overline{TEF} . Comparing this plot against case C3 in figure 4.5 that is excited at the same frequency, but with four times

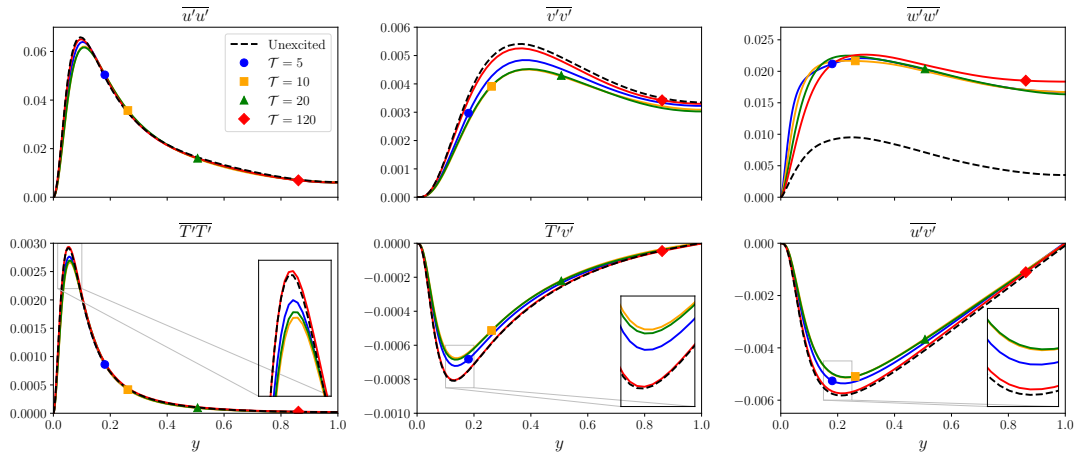


Figure 4.13. Second-order turbulent statistics at $Re_b = 3000$ and $M_b = 1.5$ subjected to the spanwise excitation at $A_f \mathcal{T} = 1$; unexcited case (---), A1: $\omega_f = 2\pi/5$ and $A_f = 0.2$ (●), A2: $\omega_f = 2\pi/10$ and $A_f = 0.1$ (■), C1: $\omega_f = 2\pi/20$ and $A_f = 0.05$ (▲), and A5: $\omega_f = 2\pi/120$ and $A_f = 0.00834$ (◆)

larger forcing amplitude, reveals that in phases $t/\mathcal{T} = 0$ and $t/\mathcal{T} = 2/4$, the deviation of near-wall streamwise streaks from their original orientation is directly proportional with the forcing amplitude. In the other two instances where the spanwise velocity perturbation changes direction; at $t/\mathcal{T} = 1/2$, case A4 has similar or even hotter streaks, while at $t/\mathcal{T} = 3/4$, case C3 contains streaks with higher intensities. It can also be seen that compared to this condition, case C1 (with $A_f = 0.05$ and $\mathcal{T} = 20$) shown in figure 4.3 resulted in *less organized* streaks which can explain a higher shear and heat transfer reduction in C1.

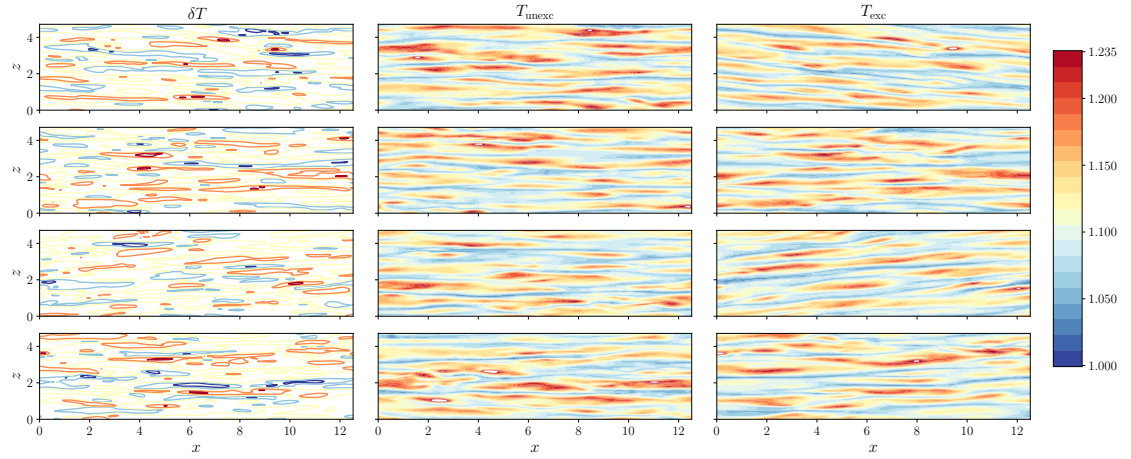


Figure 4.14. Temperature fields near the bottom wall at $y^+ \approx 4$. Simulations are performed at $Re_b = 3000$ and $M_b = 1.5$; excited case at $A_f = 0.0125$ and $\mathcal{T} = 80$, corresponding to A4 (right), unexcited case (middle), and temperature perturbation, δT (left). Each row corresponds to one instance within the first period of the limit cycle oscillations; from top to bottom $t/\mathcal{T} = 0$, $t/\mathcal{T} = 1/4$, $t/\mathcal{T} = 2/4$, and $t/\mathcal{T} = 3/4$

5. ACOUSTIC EXCITATION OF A SPATIALLY DEVELOPING BOUNDARY LAYER

A new computational setup is proposed to concentrate on the entrance region of the channel. In this case, the boundary layer undergoes the laminar to turbulent transition and grows thicker in the streamwise direction. The computational setup is schematically drawn in figure 5.1(right). Non-dimensionalization, in this case, is based on the free-stream (for flat-plate simulation) or channel center quantities (for channel flow simulation). Free-stream density, ρ_∞ , speed of sound, c_∞ , and viscosity, μ_∞ , are respectively taken as the reference parameters for density, velocity, and dynamic viscosity. Parameter $(\gamma - 1)T_\infty$ is the scaling factor for the static temperature and $1/(\gamma\rho_\infty c_\infty^2)$ represents the reference static pressure. As such, the dimensionless form of the Equation of State reads $p = (\gamma - 1)\rho T/\gamma$.

To overcome the excessive computational cost associated with resolving all turbulent flow scales at high-Reynolds numbers, such as the one studied here, Large-Eddy Simulation technique with the dynamic Smagorinsky sub-grid scale modeling, introduced in section 2.2.4, has been employed here. Equations (2.12) to (2.15), along with the complementary equations discussed in [27], are advanced in time via the implicit Beam and Warming formulation (2.9)-(2.11).

The present section is focused on the acoustic excitation of the spatially-developing boundary layer and characterizing its impact on the momentum and heat transfer near the boundaries. A procedure similar to chapter 3, has been adopted here. After validating our computational tool for the present flow configuration, base flow calculations are performed without any extra acoustic forcing. Time-averaged flow quantities are used as the *equilibrium case* for the Global Stability Analysis. One of the least stable modes that resemble the optimal mode identified for the fully-developed

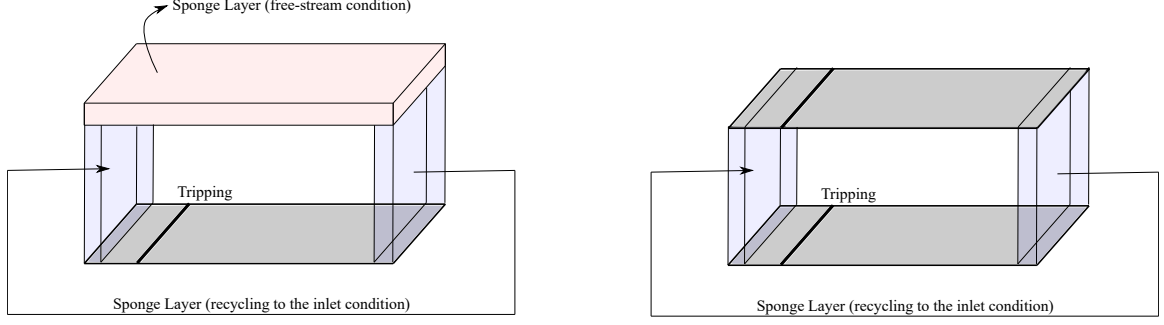


Figure 5.1. The schematic view of the computational setup for the validation study (left) and the present test case for acoustic excitation of spatially-developing boundary layer (right). The blue shaded area represents the region where the sponge layer is active in the streamwise direction, recycling the outlet to the inlet condition and the red shaded area shows the wall-normal sponge-layer enforcing the free-stream condition. The gray planes illustrate the walls and thick black lines

flow is selected for the acoustic excitation. Fully-nonlinear numerical simulations are conducted to study the interaction of acoustic wave and turbulent flow in detail.

5.1 Validation Study

Large-Eddy Simulation of H-type transition to turbulence in a spatially developing boundary layer over an adiabatic flat plate is chosen to assess our computational tool. Figure 5.1 (left) illustrates the computational setup for this study, following Sayadi et al [62], where the free-stream mach number $M_\infty = u_\infty/c_\infty = 0.2$ and Reynolds number per unit length is $Re_l = \rho_\infty u_\infty / \mu_\infty = 10^5$. Along the computational domain, Re_x varies $\in [1 \times 10^5, 10.6 \times 10^6]$. The computational setup therefore corresponds to $L_x \times L_y \times L_z = 10.6 \times 1 \times 0.6$ discretized using $N_x \times N_y \times N_z = 960 \times 160 \times 64$. Transition to turbulence is triggered via a blowing and suction on the wall following:

$$v(x, z, t) = A_1 f(x) \sin(\omega t) + A_{1/2} f(x) g(z) \cos(\omega t/2) \quad (5.1)$$

where $A_1 = 3 \times 10^{-4}$ and $A_{1/2} = 1 \times 10^{-6}$ are respectively the amplitudes of fundamental and sub-harmonic perturbations. Frequency of the suction and blowing is set to $\omega = \mathcal{F}U_\infty^2/\nu$ where $\mathcal{F} = 1.24 \times 10^{-4}$. Function $f(x)$ is defined as

$$|f(x)| = 15.1875\xi^5 - 35.4375\xi^4 + 20.25\xi^3 \quad (5.2)$$

where

$$\xi = \begin{cases} \frac{x-x_1}{x_m-x_1}, & \text{if } x_1 \leq x \leq x_m. \\ \frac{x_2-x}{x_2-x_m}, & \text{if } x_m \leq x \leq x_2, \end{cases}$$

and $x_m = (x_1 + x_2)/2$. In the present study, the start and end point of the tripping region are chosen such that $Re_{x_1} = 1.655^5$ and $Re_{x_2} = 1.81^5$ and function $g(z)$ is explicitly written as $g(z) = \cos(2\pi z/0.15)$.

To avoid the reflections from the boundaries, a numerical sponge layer is implemented wherein the following source term is added to the equations for conservation of mass, momentum, and energy (2.12):

$$S_q = -\sigma(q - q_{\text{ref}}), \quad \text{where} \quad \sigma = A_{\text{sponge}} \left(\frac{x - x_{\text{sponge},0}}{L_{\text{sponge}} - x_{\text{sponge},0}} \right)^n \quad (5.3)$$

where q_{ref} is the vector of reference variables, A_{sponge} and n are two constant parameters, and $x_{\text{sponge},0}$ and L_{sponge} are respectively, the location of the first point and total length of the sponge layer. Hence, the effect of this source term gradually increases inside the sponge zone; from zero at the beginning ($x_{\text{sponge},0}$) to A_{sponge} at the end.

The red shaded region of figure 5.1 (left) shows the sponge zone wherein the Equation (5.3) is applied to enforce the free-stream condition at $y_{\text{sponge},0} = 0.7$ and with the length $L_{\text{sponge},0} = 0.3$. The blue shaded area represents the sponge zone active in the streamwise direction, recycling the outlet to the inlet condition. This technique allows for applying a periodic boundary condition to simulate a flow that is spatially developing in nature. Spalart and Watmuff [63] verified a similar ap-

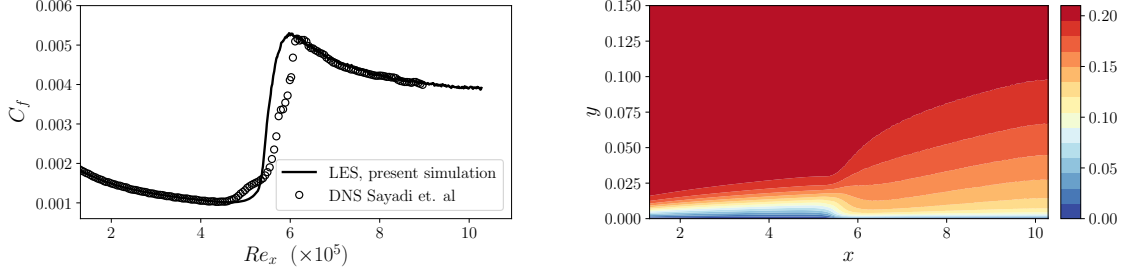


Figure 5.2. Comparison of skin friction coefficient, C_f , calculated in the present study against the DNS results of Sayadi et al [62] (left). Our Large Eddy Simulation is performed on a grid of size $N_x \times N_y \times N_z = 960 \times 160 \times 64$, while the DNS of Sayadi et al [62] has $N_x \times N_y \times N_z = 4096 \times 550 \times 512$ grid points. Time averaged streamwise flow velocity scaled with the free stream speed of sound calculated using LES (right)

proach, known as the fringe method, for simulating a turbulent boundary layer, by comparing against the experimental data, and Sayadi et al. [62] employed this methodology to study the laminar-turbulent transition. At the inlet, $x_{\text{sponge},0} = 1.5$ and $L_{\text{sponge},0} = 0.5$, while at the outlet, $x_{\text{sponge},0} = 9.1$ and $L_{\text{sponge},0} = 1.5$. In both cases, the parameters $A_{\text{sponge}} = 20$ and $n = 4$ have been adopted. Skin friction coefficient, $C_f = \tau_{\text{wall}}/0.5\rho_{\infty}U_{\infty}^2$, calculated in the present study is compared against the reference values taken from Sayadi et al [62] (with more than 1.15 billion grid points) in figure 5.2 (left). An excellent agreement is observed between the two studies in both laminar and turbulent regimes. The minor deviation in the transition section may be attributed to assuming slightly different values in the blowing and suction form in Equation (5.1) as well as possible modeling errors. Similar observations are also reported when employing different numerical techniques [64]. Figure 5.2 (right) shows the time-averaged streamwise velocity normalized with the speed of sound in free stream c_{∞} . The growth of boundary-layer thickness in the laminar and turbulent regime is clearly visible along with the sudden change appearing at the transition point.

5.2 Base Flow Calculation

Upon validating our computational tool for a test case that involves a *late transition to turbulence*, we define a new flow configuration to study the implications of acoustic excitation on the heat and momentum transport. In the present test case, schematically shown in figure 5.1 (right), the inlet condition is calculated according to

$$T_{0,\text{in}} = 400\text{K}, \quad p_{0,\text{in}} = 150\text{kPa}, \quad \text{and} \quad M_c = 0.2 \quad (5.4)$$

where $T_{0,\text{in}}$ and $p_{0,\text{in}}$ are, respectively, total temperature and pressure at the inlet, and M_{cl} represents the Mach number at the channel center-line. Top and bottom walls are no-slip and isothermal at $T_{\text{wall}} = 300\text{K}$. Following the non-dimensionalization described in previous sections, and the given the working condition (5.4), Reynolds number per unit length is $Re_l = \rho_{cl}U_{cl}/\mu_{cl} = 4,645,412$. The computational setup is $L_x \times L_y \times L_z = 0.3 \times 0.03 \times 0.03$ discretized using $N_x \times N_y \times N_z = 960 \times 160 \times 64$. Therefore, Re_x in the domain varies within $\approx [0.7 \times 10^5 - 14.6 \times 10^5]$.

Flow quantities at the inlet are calculated using the self-similar solution for the compressible laminar boundary layer [65]. It is assumed that at the inlet location, the boundary layer thickness is minimal and therefore, the center-line can be treated as the free-stream $()_\infty$ conditions.

$$\begin{aligned} \left(\frac{\rho\mu}{\rho_\infty\mu_\infty} \mathbf{f}'' \right)' + \mathbf{f} \mathbf{f}'' &= 0 \\ \left(\frac{\rho\mu}{Pr \rho_\infty\mu_\infty} \mathbf{g}' + \frac{\rho\mu}{\rho_\infty\mu_\infty} \frac{U_\infty^2}{\rho_\infty C_p T_\infty} \left(1 - \frac{1}{Pr} \right) \mathbf{f}' \mathbf{f}'' \right)' + \mathbf{f} \mathbf{g}' &= 0 \end{aligned} \quad (5.5)$$

where $\mathbf{f}' = U(x, y)/U_\infty$, $\mathbf{g} = \rho(x, y)T(x, y)/\rho_\infty T_\infty$. Spatial derivatives in wall normal direction is shown by $()' = d/d\eta$ where $d\eta = (\rho(x, y)U_\infty/\sqrt{2\zeta}) dy$ and $\zeta =$

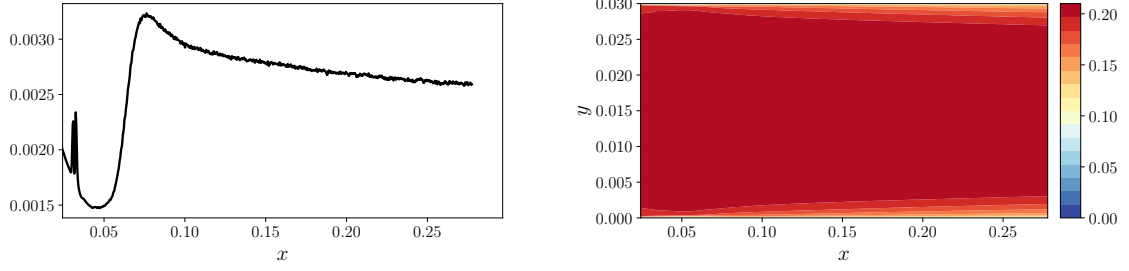


Figure 5.3. Skin friction coefficient, C_f , along the bottom wall where $Re_x \in \approx [0.7 \times 10^5 - 14.6 \times 10^5]$ using LES on a $N_x \times N_y \times N_z = 960 \times 160 \times 64$ grid (left). Time averaged streamwise flow velocity scaled with the free stream speed of sound in the spatially developing channel (right). Operating conditions are reported in (5.4).

$\rho_\infty \mu_\infty U_\infty x_{in}$. These coupled equations are solved using a fourth-order Runge-Kutta method subjected to the boundary conditions:

$$\begin{aligned} \mathbf{f}(0) &= \mathbf{f}'(0), \quad \text{and} \quad \mathbf{g}(0) = \mathbf{g}_{\text{wall}} \\ \mathbf{f}'(\infty) &= 1, \quad \text{and} \quad \mathbf{g}(\infty) = 1 \end{aligned} \tag{5.6}$$

From these quantities, all conservative variables are calculated at $x = [0.015 - 0.024]$ and set as q_{ref} in Equation (5.3) applied to the blue-shaded area of figure 5.1 (right). In this case, $x_{\text{sponge},0} = 0.024$ and $L_{\text{sponge}} = 0.009$ at the inlet and $x_{\text{sponge},0} = 0.265$ and $L_{\text{sponge}} = 0.05$ at the outlet. Sponge constants in Equation (5.3), for this configuration, are set to $A_{\text{sponge}} = 40$ and $n = 4$. To trigger the laminar-turbulent transition, the periodic suction and blowing of form (5.1) and (5.2) is employed considering $g(z) = \cos(2\pi z/0.0075)$, $Re_{x_1} = 1.36 \times 10^5$ and $Re_{x_1} = 1.56 \times 10^5$. This tripping is applied at frequency $\omega = 55$ where the amplitude of harmonic and sub-harmonic waves are $A_1 = 2.25 \times 10^{-3}$ and $A_{1/2} = 2.4 \times 10^{-5}$. Results of the skin friction coefficient, C_f , along the bottom wall as well as the spanwise-averaged mean streamwise velocity are plotted in figure 5.3.

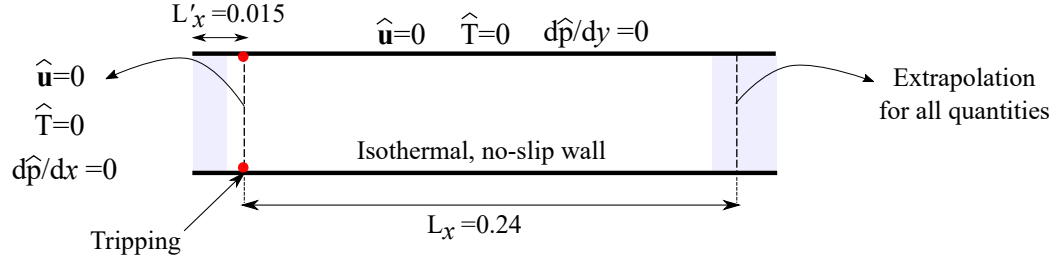


Figure 5.4. Schematic view of the computational setup for the Linear Stability Analysis as well as the imposed boundary conditions. The shaded blue region represents the sponge zone *implemented in the base flow calculations*. Vertical dashed lines (---) indicate the location where the LSA's boundary conditions are applied and the red dot is the starting point of the suction and blowing *in the base flow calculations*.

5.3 Linear Stability Analysis

Time-averaged flow quantities calculated in section 5.2 are taken as the base flow for the two-dimensional global stability analysis 2.5. Spectral method is used on the grid of size $N_x \times N_y = 128 \times 72$ subjected to the boundary conditions shown in figure 5.4. The inlet boundary condition is applied at the location of tripping *used in base flow calculations*. Velocity and temperature perturbations are assumed zero and $d\hat{p}/dx = 0$. The outlet boundary condition is imposed slightly into the sponge layer *implemented in the base flow computational setup* where all quantities are extrapolated from the interior points. All perturbation quantities vanish at the solid boundary, except the pressure where $d\hat{p}/dy = 0$. The eigenvalue spectrum, inside the domain bounded by $\mathcal{R}(\omega) \in [0, 9]$ and $\mathcal{I}(\omega) \in [-1.25, 0.5]$, is plotted in figure 5.5. In this configuration, different unstable modes are observed. Eigenvalues appearing around the line $\mathcal{R}(\omega) = 0$, like M0, represent a stationary mode which may appear due to the irregular changes in the base flow field, especially near the tripping region, reflections from the boundaries, or insufficient convergence of time statistics. Mode M1, and other more unstable modes on its right side, resemble the Tollmien–Schlichting waves that are unstable for a high-Reynolds turbulent boundary

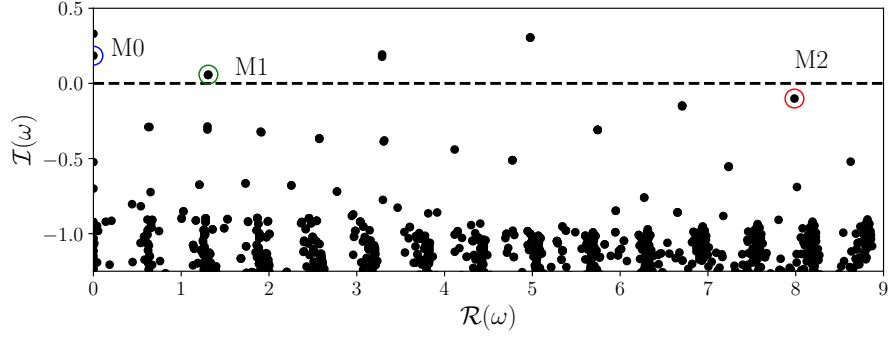


Figure 5.5. Eigenspectrum associated with the base flow described in section 5.2 subjected to the boundary conditions shown in figure 5.4. Due to the symmetric nature of eigenspectrum around $\mathcal{R}(\omega)$, only the right side is shown. Three modes are highlighted here; M0 representing a stationary mode, M1 belonging to a family of unstable modes, and M2 as the least stable mode.

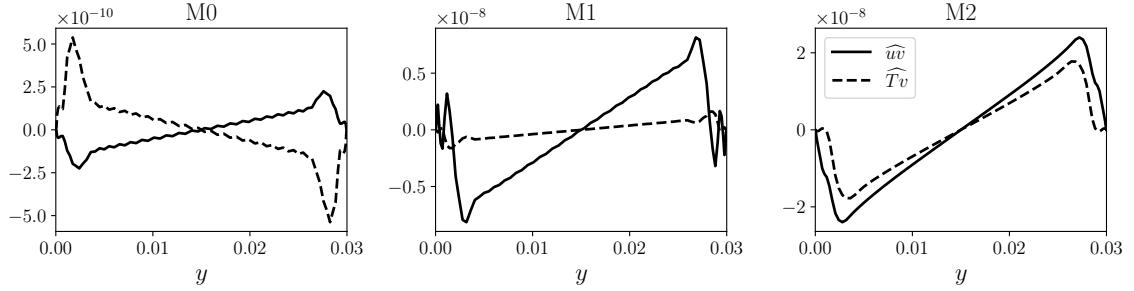


Figure 5.6. Mode shear stress, \widehat{uv} , (—) and heat flux, \widehat{Tv} , (- - -) for M0, M1, and M2 identified in figure 5.5. Profiles are plotted along the channel height at the mid-plate $x = 0.151$.

layer. On the other hand, M2 indicates the least stable mode. Two quantities of mode shear stress and heat flux, respectively, \widehat{uv} and \widehat{Tv} , are calculated according to (3.7) and are plotted for these three modes in figure 5.6. M0 looks somewhat jagged, which also suggests that this mode may appear due to numerical errors, M1 experiences substantial variations near the boundary, however, the associated

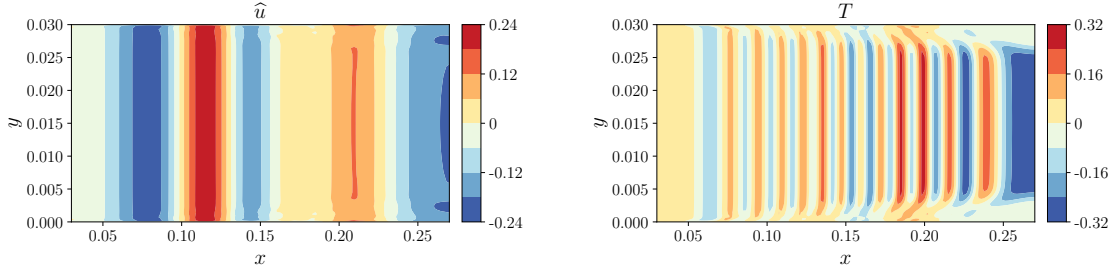


Figure 5.7. Streamwise velocity and temperature eigenfunctions, respectively \hat{u} and \hat{T} associated with mode M2 in figure 5.5.

shear stress is significantly higher than the heat flux. Among all, Mode M2 is the most similar to the mode R1 studied in chapter 3. Therefore, we pick this mode for the acoustic excitation in the remainder of this work. The streamwise velocity and temperature eigenfunctions corresponding to M2 are illustrated in figure 5.7. Eigenfunction associated with the streamwise velocity \hat{u} is minimally affected by the growth of the boundary layer suggesting that it can be classified as the acoustic mode. Due to the significant temperature difference between the wall and the boundary layer edge, which corresponds to a significant viscosity and thermal conductivity variations, the effect of boundary layer growth is clearly visible on the temperature eigenfunctions \hat{T} .

To limit the impact of inaccuracies in prescribing the exact boundary conditions, one can use multiple forcing regions operating with the exact phase shift calculated from the eigenfunctions of the selected mode. However, this technique has not been included in the present study.

5.4 Fully Non-linear Calculations

Mode M2 has been selected for the acoustic excitation of the spatially-developing boundary layer in a channel. An external periodic forcing term, \vec{f}_f , is added to the

right-hand side of the x-momentum Equation (2.12) and the work performed on the flow by this forcing is considered in the energy equation by $\vec{f}_f \cdot \vec{u}$.

$$\vec{f}_f = A_f \exp\left(-\frac{(x - x_m)^2}{L_f^2}\right) \sin(\omega_f t) \vec{e}_x \quad (5.7)$$

where A_f is the amplitude of forcing, assumed to be $A_f = 1$ in the present case, L_f represents the length scale of the forcing $L_f = 0.01$, x_m is the center of the forcing region $x_m = 0.105$, and ω_f indicates the forcing frequency which is taken from the previous section corresponding to the mode M2, $\omega_f = 7.985$. Time-averaged skin friction coefficient (C_f) in the excited and unexcited conditions are plotted in figure 5.8 (left). The excited C_f has an overall smoother transition to turbulence. In the laminar part and early stages of transition, the skin friction increases due to the excitation, but this trend is reversed from $x \approx 0.07$ to $x = 0.15$, and after that slightly overshoots C_f of fully turbulent region corresponding to the unexcited case. Figure 5.8 (right) illustrates the Shear and Thermal Enhancement Factors for the excited case following the definition in (3.4).

$$\text{SEF} = \frac{C_{f,\text{exc}}}{C_{f,\text{unexc}}} \quad \text{and} \quad \text{TEF} = \frac{Nu_{\text{exc}}}{Nu_{\text{unexc}}} \quad ((3.4))$$

where,

$$C_f(x) = \frac{\mu_w \frac{\partial U(x,y)}{\partial y} \big|_w}{0.5 \rho_{cl} U_{cl}^2} \quad \text{and} \quad Nu(x) = \frac{\frac{\partial}{\partial y} (T(x,y) - T_w) \big|_w x}{T_b(x) - T_w}$$

We observe that SEF and TEF are closely coupled. Both quantities start from the unity and increase in the early stages of transition where TEF takes larger values than SEF. This is followed by a steep decrease in both quantities, down to less than 0.8, right before the forcing region begins. Thereafter, both quantities approach towards unity and overshoot this line by ≈ 1.2 to 1.5% averaged in the magnified region. Figure 5.9 shows the temporal evolution of the temperature perturbations (δT) scaled by the static temperature at the channel center T_{cl} . A spatial averaging is taken over

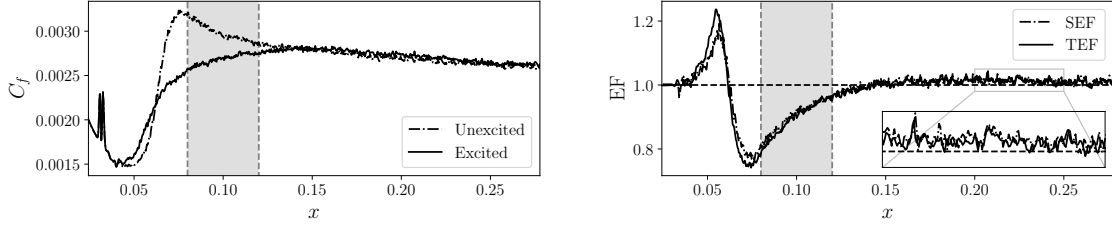


Figure 5.8. Skin friction coefficient C_f in the excited ($— \cdot \cdot —$) and unexcited ($-$) cases along the channel (left). Shear Enhancement Factor, SEF, ($— \cdot \cdot —$) as well as Thermal Enhancement Factor, TEF, ($-$) for the acoustically excited spatially developing boundary layer. The gray shaded areas show the region where the forcing amplitude $> 0.01A_f$

the first half of the forcing region $x \in [0.084 - 0.105]$. Results indicate a limit cycle is achieved in very few cycles and has a sinusoidal form without involving any clear and substantial non-linearity at the channel core. History of both enhancement factors, time-averaged over the entire bottom wall bounded by the sponge zones, $x \in [0.024, 0.265]$, are reported in figure 5.9. Both quantities oscillate around a value smaller than unity, where the SEF possesses a larger oscillation amplitude. Although the time-averaging of these two values are very similar, as also shown in figure 5.8, in the first half of a pulsation period, TEF (highlighted by red) is larger than the SEF (highlighted by blue), which can be used in scenarios where a significant heat load is expected to enter the domain only in some specific frequencies, e.g., by passing a rotor vane.

Streaming temperature ($T_{st} = \bar{T}_{exc} - \bar{T}_{unexc}$) and streaming velocity in streamwise direction (U_{st}) are shown in figure 5.10. To get a clearer picture, we have focused on the near-wall region. Both quantities are scaled with the corresponding channel centerline value. The streaming flow field is dominated by the interaction of external forcing and the unstable wave groups coming from upstream, generated due to the blowing and suction, manifested in the form of a steady vortex. Analyzing the unsteady flow properties ω_f is necessary to understand the flow physics in the excited

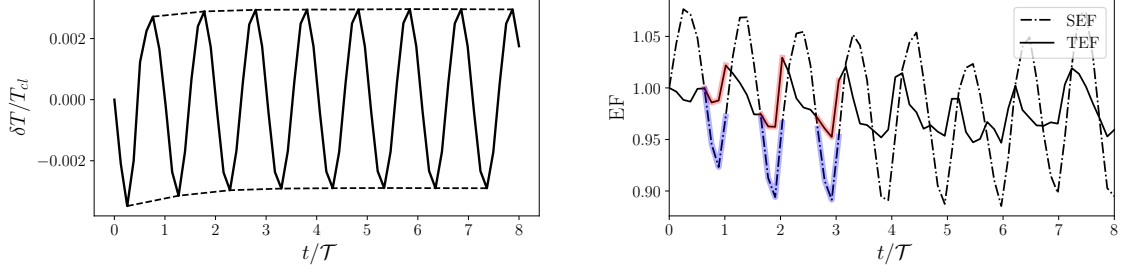


Figure 5.9. Temporal evolution of temperature perturbation at the channel center scaled by the local static temperature, T_{cl} (left). The dashed line (---) tracks the maximal and minimal values of each cycle. History of SEF (— · · —) and TEF(—) averaged over the entire bottom wall, excluding the sponge zones, for eight pulsation periods (right). Segments highlighted with red represent the phases in one period where TEF is larger than SEF, highlighted in blue

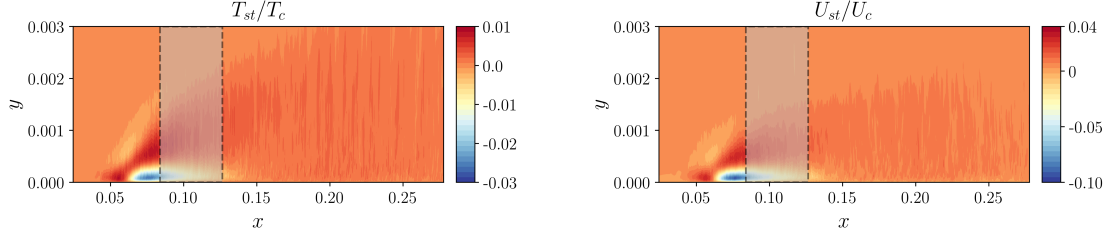


Figure 5.10. Streaming temperature, T_{st} , (left) and streaming velocity in streamwise direction, U_{st} (right) normalized by the center-line values. The gray shaded region shows the area where forcing amplitude $> 0.01 A_f$.

conditions. Following the equations discussed in section 3.2.3, Phase-locked averaged component of streamwise velocity, \hat{U} , and temperature, \hat{T} , are calculated at the excitation frequency ω_f . Figure 5.11 displays C_f and Nu along the bottom wall at four different instances of one period ($\mathcal{T} = 2\pi/\omega_f$). At the beginning of the pulsation cycle, the acoustic source acts as an expansion wave travelling upstream, which triggers the transition to turbulence earlier compared to the unexcited case. However, since it accelerates the flow in the streamwise direction, and the acceleration is known to

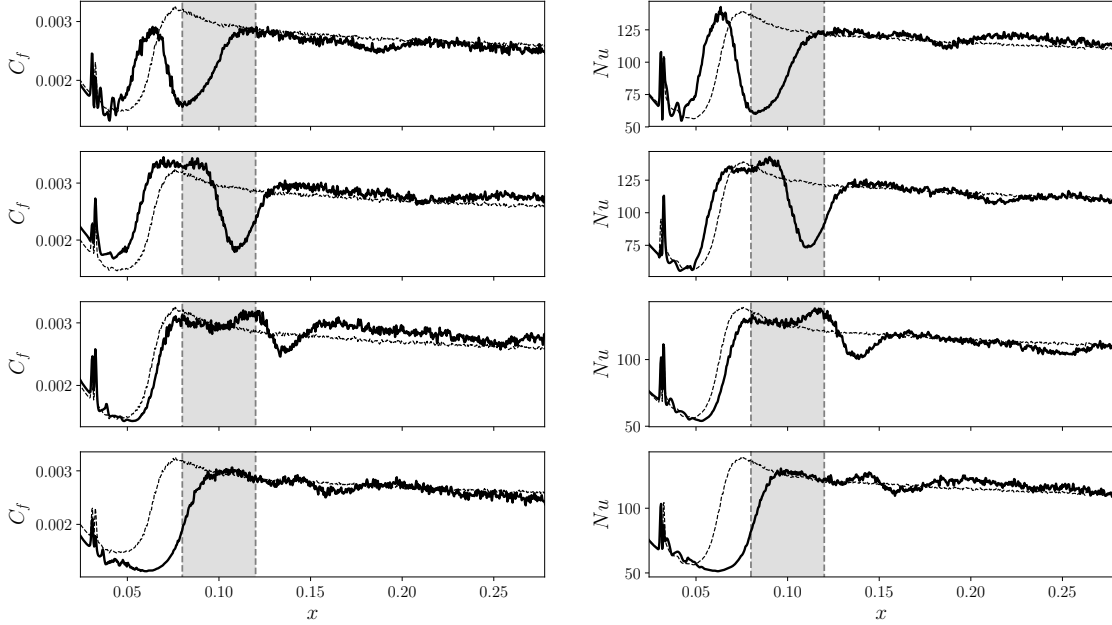


Figure 5.11. Phase-locked averaged skin friction coefficient, C_f , (left) and Nu (right) at four different instances of one excitation period (\mathcal{T}). The reference values corresponding to the time-averaged $\overline{C_f}$ and \overline{Nu} of the unexcited case are plotted with dashed-lines (- - -). The gray-shaded area indicates the region where the forcing amplitude $> 0.01A_f$. Each row corresponds to one instance; top row: $t/\mathcal{T} = 0/4$, second row: $t/\mathcal{T} = 1/4$, third row: $t/\mathcal{T} = 2/4$, and the bottom row: $t/\mathcal{T} = 3/4$.

have a stabilizing effect, a re-laminarization is spotted considering the sudden drop of C_f and Nu after the initial rise due to early transition. The positive pressure gradient decreases in the streamwise direction, and eventually, the inertial forces lead to secondary transition and turbulence. In the next instance, $t/\mathcal{T} = 1/4$ (the second row in figure 5.11), the re-laminarization is traveled downstream. From this point onward, the first transition point appears even later than the unexcited point, and the re-laminarization is convected downstream.

To have a clear look at the near-wall vortical structures, the iso-value contours of the Q-criterion for the present case at four instances of a period (\mathcal{T}) are plotted in figure 5.12. The Tollmien–Schlichting waves originated from the suction and blowing

in the upstream are observed as the rollers in the far-left. Turbulent zone is marked by the forest of near-wall vortices (spotted from $x \approx 0.15$) and the area appearing in between is attributed to the transitional zone. Instance $t/\mathcal{T} = 0$ (figure 5.12 top), shows a substantial level of perturbations early in upstream followed by early stages of break-down to turbulence. The re-laminarization is then clearly observed as a "gap" in the density of vortical structures near the bottom wall. The impact of such phenomenon was detected on the C_f and Nu in figure 5.11 This gap is weakened and is convected downstream in the following instances. At the instance $t/\mathcal{T} = 3/4$, shown on the fourth row of figure 5.12, transition to the fully-turbulent zone is delayed, although the perturbations on the T-S waves are significant.

Future work will study the effect of sponge layer strength and length as well as the location of forcing region on the results. The next effort will also consider different forcing amplitudes and will include mode M1 and other unstable family of modes for the acoustic excitation. As mentioned earlier, utilizing multiple external source terms operated with the exact phase shift calculated from the selected mode's eigenfunctions can significantly alleviate the effect of uncertainties at the boundaries and help targeting that specific mode.

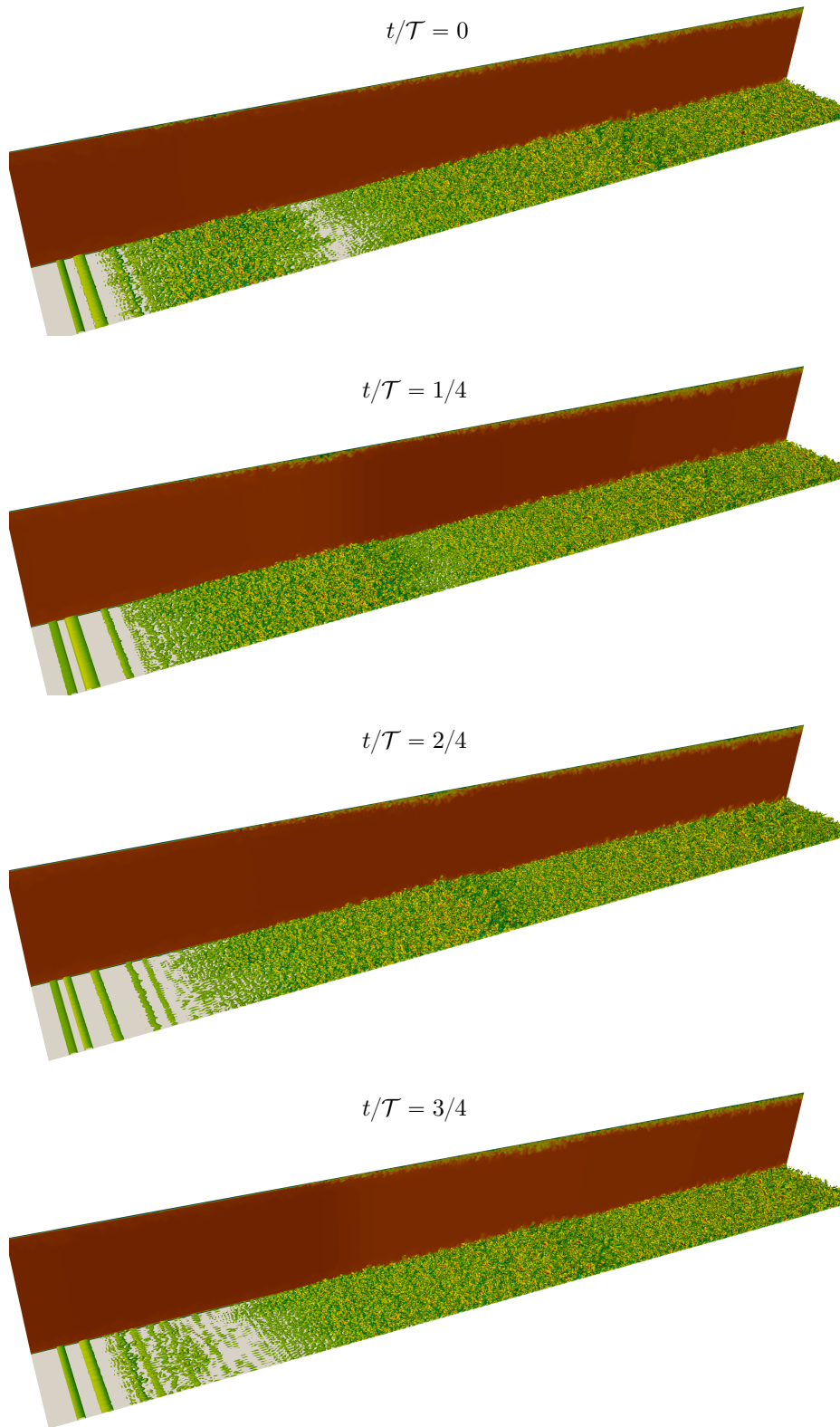


Figure 5.12. Instantaneous iso-value contours of Q-criterion in the excited condition at four instances of one period (\mathcal{T}). The structures are colored by their corresponding wall-normal velocity component from blue (negative) to red (positive values).

6. CONCLUSIONS

Passage of a sound wave over a solid boundary creates the Stokes Layer which interacts with the hydrodynamic and thermal boundary layers. Under favorable conditions, this process leads to the *acoustic streaming* which modifies the near-wall flow gradients and controls the heat and momentum transport through the boundary.

Detailed analysis of the streaming phenomenon required **developing adequate mathematical tools** to characterize acoustic-wave turbulence interaction. Linearized Navier-Stokes equations can accurately replicate the fluid flow response to small and low-frequency perturbations. In this research, Local and Global Linear Stability solvers were developed in order to identify the modes with positive heat transfer characteristics. In situations where the interaction of the turbulent boundary layer and the external acoustic wave involves the non-linear processes, accurate solution of fully non-linear Navier-Stokes equations is necessary. In the present research, we employed a solver that uses high-order compact finite difference method for Direct and Large-Eddy Simulation of turbulent flows.

The developed numerical tools were then used to study **heat transfer enhancement using acoustic streaming** created by superimposing acoustic waves in the streamwise direction. The external acoustic wave was designed to acoustically resonate within the selected configuration, according to the Linear Stability Analysis of the unexcited base flow. We observed an initially exponential growth in perturbation's amplitude which eventually leads to the limit cycle oscillations. The non-linear mechanism driving such oscillations creates a steady streaming within the background flow which enhances the heat transfer with minimal skin friction losses. Applying the external waves of similar strength at off-design frequencies did not make any measurable modifications to time-averaged flow quantities, emphasizing the role of resonance in giving rise to non-linear interactions. DNS conducted at the optimal frequency, but

with different excitation amplitudes illustrate that acoustic forcing with amplitudes higher than a minimum threshold can enhance the heat transfer up to 10.9% by only 5.3% increase in the skin friction. Violation of Reynolds Analogy in this configuration has been discussed in detail. Similar conclusions were also observed at higher Reynolds numbers or at lower resonance frequencies (due to using large domain sizes).

Direct Numerical Simulations were carried out to **demonstrate the heat transfer abatement via applying acoustic waves** in the spanwise directions. As a result of such pulsations, large near-wall structures are diverted towards the positive and negative directions. By adjusting the forcing amplitude (A_f) according to the pulsation period (\mathcal{T}) such that parameter $A_f\mathcal{T}$ remains constant, spanwise velocity perturbations are generated with similar amplitudes. Under this condition, an optimal excitation frequency was observed where 8% heat transfer reduction was achieved. In the majority of the cases involving spanwise external acoustic waves, Reynolds Analogy is valid and therefore, skin friction also decreases accordingly. The impact of turbulent flow on the velocity and temperature perturbations was also characterized at different excitation frequencies.

In the last analysis, we expanded the scope of numerical investigations to include the **evaluation of acoustic streaming in a spatially-developing boundary layer**. Global Stability Analysis was used to identify the optimal excitation frequency, that resembles the mode chosen for the fully-developed case. Due to high-Reynolds number in this configuration, Large-Eddy Simulation with a Dynamic Smagorinsky sub-grid scale modeling was employed to assess the effect of enforcing this mode in the domain via a detailed fully non-linear numerical simulations. The acoustic pulsations interact with the perturbations originated from the boundary layer tripping and modulate the transition to turbulence process. As a result, time-averaged local enhancement and reduction were observed in the heat and momentum transport near the boundaries.

The present study introduces a new technique, employing *acoustic streaming*, to improve the heat transfer efficiency of the existing thermal systems. Such processes

can be initiated by incorporating the external sources (like a loudspeaker or a horn), or by utilizing the pressure fluctuations readily available due to blade-row interaction in order to modulate the time-averaged heat transfer in both external turbine surfaces and internal cooling passages.

REFERENCES

REFERENCES

- [1] Martin Wiklund, Roy Green, and Mathias Ohlin. Acoustofluidics 14: Applications of acoustic streaming in microfluidic devices. *Lab on a Chip*, 12(14):2438–2451, 2012.
- [2] Pietro Scandura. Steady streaming in a turbulent oscillating boundary layer. *Journal of Fluid Mechanics*, 571:265–280, 2007.
- [3] Helene Bailliet, Vitalyi Gusev, Richard Raspet, and Robert A Hiller. Acoustic streaming in closed thermoacoustic devices. *The Journal of the Acoustical Society of America*, 110(4):1808–1821, 2001.
- [4] Norman Riley. Steady streaming. *Annual review of fluid mechanics*, 33(1):43–65, 2001.
- [5] Said Boluriaan and Philip J Morris. Acoustic streaming: from rayleigh to today. *International Journal of aeroacoustics*, 2(3):255–292, 2003.
- [6] Lord Rayleigh. On the circulation of air observed in kundt’s tubes, and on some allied acoustical problems. *Philosophical Transactions of the Royal Society of London*, 175:1–21, 1884.
- [7] Hermann Schlichting. Berechnung ebener periodischer grenzschichtstromungen (calculation of plane periodic boundary layer streaming). *Physikalische Zeitschrift*, 33:327–335, 1932.
- [8] Ludovic Menguy and Joel Gilbert. Non-linear acoustic streaming accompanying a plane stationary wave in a guide. *Acustica*, 86(2):249–259, 2000.
- [9] Takeru Yano. Turbulent acoustic streaming excited by resonant gas oscillation with periodic shock waves in a closed tube. *The Journal of the Acoustical Society of America*, 106(1):L7–L12, 1999.
- [10] P Vainshtein, M Fichman, and C Gutfinger. Acoustic enhancement of heat transfer between two parallel plates. *International Journal of Heat and Mass Transfer*, 38(10):1893–1899, 1995.
- [11] Murat K Aktas, Bakhtier Farouk, and Yiqiang Lin. Heat transfer enhancement by acoustic streaming in an enclosure. *Journal of heat transfer*, 127(12):1313–1321, 2005.
- [12] Murat K Aktas and Turkuler Ozgumus. The effects of acoustic streaming on thermal convection in an enclosure with differentially heated horizontal walls. *International Journal of Heat and Mass Transfer*, 53(23-24):5289–5297, 2010.
- [13] CR Lodahl, B Mutlu Sumer, and Jørgen Fredsøe. Turbulent combined oscillatory flow and current in a pipe. *Journal of Fluid Mechanics*, 373:313–348, 1998.

- [14] Alberto Scotti and Ugo Piomelli. Numerical simulation of pulsating turbulent channel flow. *Physics of Fluids*, 13(5):1367–1384, 2001.
- [15] Chenyang Weng, Susann Boij, and Ardeshtir Hanifi. Numerical and theoretical investigation of pulsatile turbulent channel flows. *Journal of Fluid Mechanics*, 792:98–133, 2016.
- [16] Sedat F Tardu, Gilbert Binder, and Ron F Blackwelder. Turbulent channel flow with large-amplitude velocity oscillations. *Journal of Fluid Mechanics*, 267:109–151, 1994.
- [17] Tokuro Mizushima, Toshiro Maruyama, and Yasumi Shiozaki. Pulsating turbulent flow in a tube. *Journal of Chemical Engineering of Japan*, 6(6):487–494, 1974.
- [18] HA Havemann and NN Narayan Rao. Heat transfer in pulsating flow. *Nature*, 174(4418):41, 1954.
- [19] MA Habib, SAM Said, AA Al-Farayedhi, SA Al-Dini, A Asghar, and SA Gbadebo. Heat transfer characteristics of pulsated turbulent pipe flow. *Heat and mass transfer*, 34(5):413–421, 1999.
- [20] SAM Said, A Al-Farayedhi, MA Habib, SA Gbadebo, A Asghar, and S Al-Dini. Experimental investigation of heat transfer in pulsating turbulent pipe flow. In *Proc Turbulent Heat Transfer Conference-2, Manchester, UK, Paper*, volume 2, pages 54–62, 1998.
- [21] Iman Rahbari and Carlo Scalo. Linear stability analysis of compressible channel flow over porous walls. In *Whither Turbulence and Big Data in the 21st Century?*, pages 451–467. Springer, 2017.
- [22] Iman Rahbari and Carlo Scalo. Quasi-spectral sparse bi-global stability analysis of compressible channel flow over complex impedance. In *55th AIAA Aerospace Sciences Meeting*, page 1879, 2017.
- [23] Gary N Coleman, John Kim, and RD Moser. A numerical study of turbulent supersonic isothermal-wall channel flow. *Journal of Fluid Mechanics*, 305:159–183, 1995.
- [24] Santhanam Nagarajan, SK Lele, and JH Ferziger. Leading-edge effects in bypass transition. *Journal of Fluid Mechanics*, 572:471–504, 2007.
- [25] Santhanam Nagarajan. *Leading edge effects in bypass transition*. PhD thesis, Stanford University, 2004.
- [26] Sanjiva K Lele. Compact finite difference schemes with spectral-like resolution. *Journal of computational physics*, 103(1):16–42, 1992.
- [27] Santhanam Nagarajan, Sanjiva K Lele, and Joel H Ferziger. A robust high-order compact method for large eddy simulation. *Journal of Computational Physics*, 191(2):392–419, 2003.
- [28] Richard M Beam and Robert F Warming. An implicit finite-difference algorithm for hyperbolic systems in conservation-law form. *Journal of computational physics*, 22(1):87–110, 1976.

- [29] Parviz Moin, Kyle Squires, W Cabot, and Sangsan Lee. A dynamic subgrid-scale model for compressible turbulence and scalar transport. *Physics of Fluids A: Fluid Dynamics*, 3(11):2746–2757, 1991.
- [30] Douglas K Lilly. A proposed modification of the germano subgrid-scale closure method. *Physics of Fluids A: Fluid Dynamics*, 4(3):633–635, 1992.
- [31] Mujeeb R Malik. Numerical methods for hypersonic boundary layer stability. *Journal of computational physics*, 86(2):376–413, 1990.
- [32] Sean Hu and Xiaolin Zhong. Linear instability of compressible plane couette flows. In *35th Aerospace Sciences Meeting and Exhibit*, page 432, 1997.
- [33] Sean Hu and Xiaolin Zhong. Linear stability of viscous supersonic plane couette flow. *Physics of Fluids*, 10(3):709–729, 1998.
- [34] Vassilios Theofilis. Global linear instability. *Annual Review of Fluid Mechanics*, 43:319–352, 2011.
- [35] V Theofilis and T Colonius. Three-dimensional instabilities of compressible flow over open cavities: direct solution of the biglobal eigenvalue problem. *AIAA Paper*, 2544:2004, 2004.
- [36] Yousef Saad. *Numerical methods for large eigenvalue problems: revised edition*, volume 66. SIAM, 2011.
- [37] Xavier Merle, Frédéric Alizard, and Jean-Christophe Robinet. Finite difference methods for viscous incompressible global stability analysis. *Computers & Fluids*, 39(6):911–925, 2010.
- [38] Pedro Paredes, Miguel Hermanns, Soledad Le Clainche, and Vassilis Theofilis. Order 10 4 speedup in global linear instability analysis using matrix formation. *Computer Methods in Applied Mechanics and Engineering*, 253:287–304, 2013.
- [39] Vicente Hernandez, Jose E. Roman, and Vicente Vidal. SLEPc: A scalable and flexible toolkit for the solution of eigenvalue problems. *ACM Trans. Math. Software*, 31(3):351–362, 2005.
- [40] Vicente Hernández, José E Román, Andrés Tomás, and Vicent Vidal. Slepcc users manual. Technical report, Technical Report DSIC-II/24/02-Revision 2.3. 2, D. Sistemas Informáticos y Computación, Universidad Politécnica de Valencia, 2006.
- [41] Xiaoye S. Li and James W. Demmel. Superlu dist: A scalable distributed-memory sparse direct solver for unsymmetric linear systems. *ACM Trans. Mathematical Software*, 29(2):110–140, June 2003.
- [42] X.S. Li, J.W. Demmel, J.R. Gilbert, iL. Grigori, M. Shao, and I. Yamazaki. SuperLU Users’ Guide. Technical Report LBNL-44289, Lawrence Berkeley National Laboratory, September 1999.
- [43] Ray-Sing Lin and Mujeeb R Malik. On the stability of attachment-line boundary layers. part 1. the incompressible swept hiemenz flow. *Journal of Fluid Mechanics*, 311:239–255, 1996.

- [44] V Theofilis, AV Fedorov, and SS Collis. Leading-edge boundary layer flow (prandtl's vision, current developments and future perspectives). In *IUTAM Symposium on One Hundred Years of Boundary Layer Research*, pages 73–82. Springer, 2006.
- [45] Peter J Schmid and Dan S Henningson. *Stability and transition in shear flows*, volume 142. Springer Science & Business Media, 2012.
- [46] Olivier Marquet, Denis Sipp, and Laurent Jacquin. Sensitivity analysis and passive control of cylinder flow. *Journal of Fluid Mechanics*, 615:221–252, 2008.
- [47] Mahesh Natarajan, Jonathan B Freund, and Daniel J Bodony. Actuator selection and placement for localized feedback flow control. *Journal of Fluid Mechanics*, 809:775–792, 2016.
- [48] Joseph W Nichols, Johan Larsson, Matteo Bernardini, and Sergio Pirozzoli. Stability and modal analysis of shock/boundary layer interactions. *Theoretical and Computational Fluid Dynamics*, 31(1):33–50, 2017.
- [49] Moon Joo Lee, John Kim, and Parviz Moin. Structure of turbulence at high shear rate. *Journal of Fluid Mechanics*, 216:561–583, 1990.
- [50] Javier Jiménez. How linear is wall-bounded turbulence? *Physics of Fluids*, 25(11):110814, 2013.
- [51] Emmanuel Lévêque, Federico Toschi, Liang Shao, and J-P Bertoglio. Shear-improved smagorinsky model for large-eddy simulation of wall-bounded turbulent flows. *Journal of Fluid Mechanics*, 570:491–502, 2007.
- [52] R Friedrich and FP Bertolotti. Compressibility effects due to turbulent fluctuations. *Applied Scientific Research*, 57(3-4):165–194, 1996.
- [53] WC Reynolds and AKMF Hussain. The mechanics of an organized wave in turbulent shear flow. part 3. theoretical models and comparisons with experiments. *Journal of Fluid Mechanics*, 54(2):263–288, 1972.
- [54] Javier Jimenez, Markus Uhlmann, Alfredo Pinelli, and Genta Kawahara. Turbulent shear flow over active and passive porous surfaces. *Journal of Fluid Mechanics*, 442:89–117, 2001.
- [55] Juan C Del Alamo and Javier Jimenez. Linear energy amplification in turbulent channels. *Journal of Fluid Mechanics*, 559:205–213, 2006.
- [56] Nils Tilton and Luca Cortelezzi. Linear stability analysis of pressure-driven flows in channels with porous walls. *Journal of Fluid Mechanics*, 604:411–445, 2008.
- [57] Oliver MF Browne, Gonzalo Rubio, Esteban Ferrer, and Eusebio Valero. Sensitivity analysis to unsteady perturbations of complex flows: a discrete approach. *International Journal for Numerical Methods in Fluids*, 76(12):1088–1110, 2014.
- [58] Frank M White and Isla Corfield. *Viscous fluid flow*, volume 3. McGraw-Hill New York, 2006.
- [59] Roberto Maffulli and Li He. Wall temperature effects on heat transfer coefficient for high-pressure turbines. *Journal of Propulsion and Power*, 30(4):1080–1090, 2014.

- [60] AKM Fazle Hussain. Coherent structures and turbulence. *Journal of Fluid Mechanics*, 173:303–356, 1986.
- [61] Wen-Je Jung, Norberto Mangiavacchi, and Rayhaneh Akhavan. Suppression of turbulence in wall-bounded flows by high-frequency spanwise oscillations. *Physics of Fluids A: Fluid Dynamics*, 4(8):1605–1607, 1992.
- [62] Taraneh Sayadi, Curtis W Hamman, and Parviz Moin. Direct numerical simulation of complete h-type and k-type transitions with implications for the dynamics of turbulent boundary layers. *Journal of Fluid Mechanics*, 724:480–509, 2013.
- [63] Philippe R Spalart and Jonathan H Watmuff. Experimental and numerical study of a turbulent boundary layer with pressure gradients. *Journal of Fluid Mechanics*, 249:337–371, 1993.
- [64] Minwoo Kim, Jiseop Lim, Seungtae Kim, Solkeun Jee, Jaeyoung Park, and Donghun Park. Large-eddy simulation with parabolized stability equations for turbulent transition using openfoam. *Computers & Fluids*, 189:108–117, 2019.
- [65] Tuncer Cebeci and Smith A. M. O. *Analysis of turbulent boundary layers*. Academic Press, New York, 1974.

APPENDIX

A. EQUATIONS FOR GLOBAL STABILITY ANALYSIS

In the global stability analysis, as discussed in chapter 2, the decomposition

$$q(x, y, z, t) = \bar{q}(x, y, z) + \hat{q}(x, y) e^{j\beta z} e^{-j\omega t}$$

is applied to the linearized Navier-Stokes equations which eventually leads to the generalized eigenvalue problem

$$\mathbf{A}\hat{\mathbf{q}} = \omega\mathbf{B}\hat{\mathbf{q}} \quad (2.21)$$

where,

$$\begin{pmatrix} A_u^X & A_v^X & A_w^X & A_p^X & A_T^X \\ A_u^Y & A_v^Y & A_w^Y & A_p^Y & A_T^Y \\ A_u^Z & A_v^Z & A_w^Z & A_p^Z & A_T^Z \\ A_u^C & A_v^C & A_w^C & A_p^C & A_T^C \\ A_u^E & A_v^E & A_w^E & A_p^E & A_T^E \end{pmatrix} \begin{pmatrix} \hat{\mathbf{u}} \\ \hat{\mathbf{v}} \\ \hat{\mathbf{w}} \\ \hat{\mathbf{p}} \\ \hat{\mathbf{T}} \end{pmatrix} = \omega \begin{pmatrix} B_u^X & B_v^X & B_w^X & B_p^X & B_T^X \\ B_u^Y & B_v^Y & B_w^Y & B_p^Y & B_T^Y \\ B_u^Z & B_v^Z & B_w^Z & B_p^Z & B_T^Z \\ B_u^C & B_v^C & B_w^C & B_p^C & B_T^C \\ B_u^E & B_v^E & B_w^E & B_p^E & B_T^E \end{pmatrix} \begin{pmatrix} \hat{\mathbf{u}} \\ \hat{\mathbf{v}} \\ \hat{\mathbf{w}} \\ \hat{\mathbf{p}} \\ \hat{\mathbf{T}} \end{pmatrix} \quad (2.22)$$

Matrices \mathbf{A} and \mathbf{B} are block-structured and the detailed mathematical description of each block is adopted from Theofilis and Colonius [35] as follows,

$$\begin{aligned}
A_u^X = & -\frac{4}{3} \frac{\bar{\mu}}{Re} D_{xx} + \left[-\frac{4}{3} \frac{1}{Re} \left(\frac{d\bar{\mu}}{d\bar{T}} \right) \frac{\partial \bar{T}}{\partial x} + \bar{\rho} \bar{u} \right] D_x \\
& -\frac{\bar{\mu}}{Re} D_{yy} + \left[-\frac{1}{Re} \left(\frac{d\bar{\mu}}{d\bar{T}} \right) \frac{\partial \bar{T}}{\partial y} + \bar{\rho} \bar{v} \right] D_y \\
& + \frac{\beta^2 \bar{\mu}}{Re} + 2\bar{\rho} \frac{\partial \bar{u}}{\partial x} + \bar{\rho} \frac{\partial \bar{v}}{\partial y} + j\beta \bar{\rho} \bar{w} + \bar{u} \frac{\partial \bar{\rho}}{\partial x} + \bar{v} \frac{\partial \bar{\rho}}{\partial y}
\end{aligned}$$

$$\begin{aligned}
A_v^X = & -\frac{1}{3} \frac{\bar{\mu}}{Re} D_{xy} - \frac{1}{Re} \left(\frac{d\bar{\mu}}{d\bar{T}} \right) \frac{\partial \bar{T}}{\partial y} D_x \\
& + \frac{2}{3} \frac{1}{Re} \left(\frac{d\bar{\mu}}{d\bar{T}} \right) \frac{\partial \bar{T}}{\partial x} D_y + \bar{\rho} \frac{\partial \bar{u}}{\partial y}
\end{aligned}$$

$$A_w^X = -\frac{j\beta}{3Re} \bar{\mu} D_x + \frac{2j\beta}{3Re} \left(\frac{d\bar{\mu}}{d\bar{T}} \right) \frac{\partial \bar{T}}{\partial x}$$

$$A_p^X = +\frac{1}{\gamma M^2} D_x + \frac{1}{\bar{T}} \left(\bar{u} \frac{\partial \bar{u}}{\partial x} + \bar{v} \frac{\partial \bar{u}}{\partial y} \right)$$

$$\begin{aligned}
A_T^X = & -\frac{1}{Re} \left(\frac{d\bar{\mu}}{d\bar{T}} \right) \left(\frac{4}{3} \frac{\partial \bar{u}}{\partial x} - \frac{2}{3} \frac{\partial \bar{v}}{\partial y} \right) D_x \\
& -\frac{1}{Re} \left(\frac{d\bar{\mu}}{d\bar{T}} \right) \left(\frac{\partial \bar{u}}{\partial y} + \frac{\partial \bar{v}}{\partial x} \right) D_y \\
& -\frac{1}{Re} \left(\frac{d\bar{\mu}}{d\bar{T}} \right) \left(j\beta \frac{\partial \bar{w}}{\partial x} + \frac{4}{3} \frac{\partial^2 \bar{u}}{\partial x^2} + \frac{\partial^2 \bar{u}}{\partial y^2} + \frac{1}{3} \frac{\partial^2 \bar{v}}{\partial xy} \right) \\
& -\frac{1}{Re} \left(\frac{d^2 \bar{\mu}}{d\bar{T}^2} \right) \left(\frac{4}{3} \frac{\partial \bar{T}}{\partial x} \frac{\partial \bar{u}}{\partial x} + \frac{\partial \bar{T}}{\partial y} \frac{\partial \bar{u}}{\partial y} + \frac{\partial \bar{T}}{\partial y} \frac{\partial \bar{v}}{\partial x} - \frac{2}{3} \frac{\partial \bar{T}}{\partial x} \frac{\partial \bar{v}}{\partial y} \right) \\
& -\frac{\bar{\rho}}{\bar{T}} \left(\bar{u} \frac{\partial \bar{u}}{\partial x} + \bar{v} \frac{\partial \bar{u}}{\partial y} \right)
\end{aligned}$$

$$B_u^X = j\bar{\rho}$$

$$A_u^Y = -\frac{1}{3} \frac{\bar{\mu}}{Re} D_{xy} + \frac{2}{3Re} \left(\frac{d\bar{\mu}}{dT} \right) \frac{\partial \bar{T}}{\partial y} D_x - \frac{1}{Re} \left(\frac{d\bar{\mu}}{dT} \right) \frac{\partial \bar{T}}{\partial x} D_y + \bar{\rho} \frac{\partial \bar{v}}{\partial x}$$

$$A_v^Y = -\frac{\bar{\mu}}{Re} D_{xx} + \left[-\frac{1}{Re} \left(\frac{d\bar{\mu}}{dT} \right) \frac{\partial \bar{T}}{\partial x} + \bar{\rho} \bar{u} \right] D_x - \frac{4}{3} \frac{\bar{\mu}}{Re} D_{yy} + \left[-\frac{4}{3Re} \left(\frac{d\bar{\mu}}{dT} \right) \frac{\partial \bar{T}}{\partial y} + \bar{\rho} \bar{v} \right] D_y + \frac{\beta^2 \bar{\mu}}{Re} + \bar{\rho} \frac{\partial \bar{u}}{\partial x} + 2\bar{\rho} \frac{\partial \bar{v}}{\partial y} + j\beta \bar{\rho} \bar{w} + \bar{u} \frac{\partial \bar{\rho}}{\partial x} + \bar{v} \frac{\partial \bar{\rho}}{\partial y}$$

$$A_w^Y = -\frac{j}{3} \frac{\beta \bar{\mu}}{Re} D_y + \frac{2j\beta}{3} \frac{1}{Re} \left(\frac{d\bar{\mu}}{dT} \right) \frac{\partial \bar{T}}{\partial y}$$

$$A_p^Y = \frac{1}{\gamma M^2} D_y + \frac{1}{\bar{T}} \left(\bar{u} \frac{\partial \bar{v}}{\partial x} + \bar{v} \frac{\partial \bar{v}}{\partial y} \right)$$

$$A_T^Y = -\frac{1}{Re} \left(\frac{d\bar{\mu}}{dT} \right) \left(\frac{\partial \bar{u}}{\partial y} + \frac{\partial \bar{v}}{\partial x} \right) D_x - \frac{1}{Re} \left(\frac{d\bar{\mu}}{dT} \right) \left(\frac{4}{3} \frac{\partial \bar{v}}{\partial y} - \frac{2}{3} \frac{\partial \bar{u}}{\partial x} \right) D_y - \frac{1}{Re} \left(\frac{d\bar{\mu}}{dT} \right) \left(j\beta \frac{\partial \bar{w}}{\partial y} + \frac{4}{3} \frac{\partial^2 \bar{v}}{\partial y^2} + \frac{1}{3} \frac{\partial^2 \bar{u}}{\partial x \partial y} + \frac{\partial^2 \bar{v}}{\partial x^2} \right) - \frac{1}{Re} \left(\frac{d^2 \bar{\mu}}{dT^2} \right) \left(\frac{\partial \bar{T}}{\partial x} \frac{\partial \bar{u}}{\partial y} + \frac{4}{3} \frac{\partial \bar{T}}{\partial y} \frac{\partial \bar{v}}{\partial y} - \frac{2}{3} \frac{\partial \bar{T}}{\partial y} \frac{\partial \bar{u}}{\partial x} + \frac{\partial \bar{T}}{\partial x} \frac{\partial \bar{v}}{\partial x} \right) - \frac{\bar{\rho}}{\bar{T}} \left(\bar{u} \frac{\partial \bar{v}}{\partial x} + \bar{v} \frac{\partial \bar{v}}{\partial y} \right)$$

$$B_v^Y = j\bar{\rho}$$

$$A_u^Z = -\frac{j\beta}{3Re}\bar{\mu}D_x - \frac{j\beta}{Re}\left(\frac{d\bar{\mu}}{d\bar{T}}\right)\frac{\partial\bar{T}}{\partial x} + \bar{\rho}\frac{\partial\bar{w}}{\partial x}$$

$$A_v^Z = -\frac{j\beta}{3Re}\bar{\mu}D_y - \frac{j\beta}{Re}\left(\frac{d\bar{\mu}}{d\bar{T}}\right)\frac{\partial\bar{T}}{\partial y} + \bar{\rho}\frac{\partial\bar{w}}{\partial y}$$

$$\begin{aligned} A_w^Z = & -\frac{1}{Re}\bar{\mu}D_{xx} - \frac{1}{Re}\bar{\mu}D_{yy} \\ & + \left[-\frac{1}{Re}\left(\frac{d\bar{\mu}}{d\bar{T}}\right)\frac{\partial\bar{T}}{\partial x} + \bar{\rho}u\right]D_x \\ & + \left[-\frac{1}{Re}\left(\frac{d\bar{\mu}}{d\bar{T}}\right)\frac{\partial\bar{T}}{\partial y} + \bar{\rho}v\right]D_y \\ & + \frac{4}{3Re}\bar{\mu}\beta^2 + \bar{\rho}\frac{\partial\bar{u}}{\partial x} + \bar{\rho}\frac{\partial\bar{v}}{\partial y} + j\beta\bar{\rho}w + \bar{u}\frac{\partial\bar{\rho}}{\partial x} + \bar{v}\frac{\partial\bar{\rho}}{\partial y} \end{aligned}$$

$$A_p^Z = \frac{j\beta}{\gamma M^2} + \frac{1}{\bar{T}}\left(\bar{u}\frac{\partial\bar{w}}{\partial x} + \bar{v}\frac{\partial\bar{w}}{\partial y}\right)$$

$$\begin{aligned} A_T^Z = & -\frac{1}{Re}\left(\frac{d\bar{\mu}}{d\bar{T}}\right)\frac{\partial\bar{w}}{\partial x}D_x - \frac{1}{Re}\left(\frac{d\bar{\mu}}{d\bar{T}}\right)\frac{\partial\bar{w}}{\partial y}D_y \\ & -\frac{1}{Re}\left(\frac{d\bar{\mu}}{d\bar{T}}\right)\left[\frac{\partial^2\bar{w}}{\partial x^2} + \frac{\partial^2\bar{w}}{\partial y^2} - \frac{2}{3}j\beta\left(\frac{\partial\bar{u}}{\partial x} + \frac{\partial\bar{v}}{\partial y}\right)\right] \\ & -\frac{1}{Re}\left(\frac{d^2\bar{\mu}}{d\bar{T}^2}\right)\left[\frac{\partial\bar{T}}{\partial x}\frac{\partial\bar{w}}{\partial x} + \frac{\partial\bar{T}}{\partial y}\frac{\partial\bar{w}}{\partial y}\right] - \frac{\bar{\rho}}{\bar{T}}\left(\bar{u}\frac{\partial\bar{w}}{\partial x} + \bar{v}\frac{\partial\bar{w}}{\partial y}\right) \end{aligned}$$

$$B_p^Z = j\bar{\rho}$$

$$A_u^E = \left[-2 \frac{\gamma(\gamma-1)M^2}{Re} \bar{\mu} \left(\frac{4}{3} \frac{\partial \bar{u}}{\partial x} - \frac{2}{3} \frac{\partial \bar{v}}{\partial y} \right) + \gamma \bar{\rho} \bar{T} \right] D_x$$

$$- 2 \frac{\gamma(\gamma-1)M^2}{Re} \bar{\mu} \left(\frac{\partial \bar{u}}{\partial y} + \frac{\partial \bar{v}}{\partial x} \right) D_y$$

$$- 2 \frac{j\beta\gamma(\gamma-1)M^2}{Re} \bar{\mu} \frac{\partial \bar{w}}{\partial x} + \bar{T} \frac{\partial \bar{\rho}}{\partial x} + \bar{\rho} \frac{\partial \bar{T}}{\partial x}$$

$$A_v^E = -2 \frac{\gamma(\gamma-1)M^2}{Re} \bar{\mu} \left(\frac{\partial \bar{u}}{\partial y} + \frac{\partial \bar{v}}{\partial x} \right) D_x$$

$$+ \left[-2 \frac{\gamma(\gamma-1)M^2}{Re} \bar{\mu} \left(-\frac{2}{3} \frac{\partial \bar{u}}{\partial x} + \frac{4}{3} \frac{\partial \bar{v}}{\partial y} \right) + \gamma \bar{\rho} \bar{T} \right] D_y$$

$$- 2 \frac{j\beta\gamma(\gamma-1)M^2}{Re} \bar{\mu} \frac{\partial \bar{w}}{\partial y} + \bar{T} \frac{\partial \bar{\rho}}{\partial y} + \bar{\rho} \frac{\partial \bar{T}}{\partial y}$$

$$A_w^E = -2 \frac{\gamma(\gamma-1)M^2}{Re} \bar{\mu} \frac{\partial \bar{w}}{\partial x} D_x$$

$$- 2 \frac{\gamma(\gamma-1)M^2}{Re} \bar{\mu} \frac{\partial \bar{w}}{\partial y} D_y$$

$$+ \frac{4}{3} \frac{j\beta\gamma(\gamma-1)M^2}{Re} \bar{\mu} \left(\frac{\partial \bar{u}}{\partial x} + \frac{\partial \bar{v}}{\partial y} \right) + j\beta\gamma \bar{\rho} \bar{T}$$

$$A_p^E = \bar{u} D_x + \bar{v} D_y + j \beta \bar{w} + \gamma \left(\frac{\partial \bar{u}}{\partial x} + \frac{\partial \bar{v}}{\partial y} \right)$$

$$A_T^E = -\frac{\gamma \bar{\kappa}}{RePr} D_{xx} - 2 \frac{\gamma}{RePr} \left(\frac{d\bar{\kappa}}{d\bar{T}} \right) \frac{\partial \bar{T}}{\partial x} D_x$$

$$- \frac{\gamma \bar{\kappa}}{RePr} D_{yy} - 2 \frac{\gamma}{RePr} \left(\frac{d\bar{\kappa}}{d\bar{T}} \right) \frac{\partial \bar{T}}{\partial y} D_y$$

$$+ \frac{\beta^2 \gamma \bar{\kappa}}{RePr} - \frac{\gamma}{RePr} \left(\frac{d\bar{\kappa}}{d\bar{T}} \right) (\bar{T}_{xx} + \bar{T}_{yy})$$

$$- \frac{\gamma}{RePr} \left(\frac{d^2 \bar{\kappa}}{d\bar{T}^2} \right) \left(\frac{\partial \bar{T}^2}{\partial x} + \frac{\partial \bar{T}^2}{\partial y} \right)$$

$$- \frac{\gamma(\gamma-1)M^2}{Re} \left(\frac{d\bar{\mu}}{d\bar{T}} \right) \left(\frac{4}{3} \frac{\partial \bar{u}^2}{\partial x} + \frac{\partial \bar{v}^2}{\partial x} + \frac{\partial \bar{w}^2}{\partial x} + \frac{\partial \bar{u}^2}{\partial y} \right.$$

$$\left. + \frac{4}{3} \frac{\partial \bar{v}^2}{\partial y} + \frac{\partial \bar{w}^2}{\partial y} - \frac{4}{3} \frac{\partial \bar{u}}{\partial x} \frac{\partial \bar{v}}{\partial y} + 2 \frac{\partial \bar{u}}{\partial y} \frac{\partial \bar{v}}{\partial x} \right)$$

$$B_p^E = j$$

$$A_u^C = \bar{\rho}\bar{T}D_x + \bar{T}\frac{\partial\bar{\rho}}{\partial x}$$

$$A_v^C = \bar{\rho}\bar{T}D_y + \bar{T}\frac{\partial\bar{\rho}}{\partial y}$$

$$A_w^C = j\beta\bar{\rho}\bar{T}\bar{w}$$

$$\begin{aligned} A_T^C = & -\bar{\rho}\bar{u}D_x - \bar{\rho}\bar{v}D_y - \bar{\rho}\frac{\partial\bar{u}}{\partial x} - \bar{\rho}\frac{\partial\bar{v}}{\partial y} \\ & -j\beta\bar{\rho}\bar{w} - \bar{u}\frac{\partial\bar{\rho}}{\partial x} - \bar{v}\frac{\partial\bar{\rho}}{\partial y} + \frac{\bar{\rho}}{\bar{T}}\left(\bar{u}\frac{\partial\bar{T}}{\partial x} + \bar{v}\frac{\partial\bar{T}}{\partial y}\right) \end{aligned}$$

$$L_p^C = \bar{u}D_x + \bar{v}D_y + j\beta\bar{w} + \frac{\partial\bar{u}}{\partial x} + \frac{\partial\bar{v}}{\partial y} - \frac{1}{\bar{T}}\left(\bar{u}\frac{\partial\bar{T}}{\partial x} + \bar{v}\frac{\partial\bar{T}}{\partial y}\right)$$

$$B_T^C = -j\bar{\rho}$$

$$B_p^C = j$$

where D_x and D_{xx} are first and second derivative operators in x direction and D_y and D_{yy} are their counterparts in y direction, respectively. Mixed derivatives are represented by D_{xy} . These operators are calculated via numerical techniques discussed in section 2.5.

VITA

VITA

Iman Rahbari**EDUCATION**

Ph.D. in Mechanical Engineering
Purdue University, West Lafayette, USA (06/2015 - 12/2019)

Master of Science in Mechanical Engineering
University of Tehran, Tehran, Iran (09/2011 - 09/2014)

Bachelor of Science in Mechanical Engineering
Semnan University, Semnan, Iran (09/2007 - 09/2011)

EMPLOYMENTS

Research and Teaching Assistant, School of Mechanical Engineering
Purdue University, West Lafayette, USA (06/2015 - 12/2019)

Associate Research Engineer-Intern
ArcelorMittal, East Chicago, USA (07/2017 - 08/2017)

Research and Teaching Assistant, School of Mechanical Engineering
University of Tehran, Tehran, Iran (06/2012 - 02/2015)

AWARDS

Cloud Credits for Research, Amazon Web Service (\$15,000 in Credits), 2019

Magoon Award for Excellence in Teaching, Purdue University, 2019

Summer Research Fellowship, Purdue University, 2019

First Ranked Graduate in Heat Transfer and Fluid Flow, Semnan University, 2011